

Bangor University

DOCTOR OF PHILOSOPHY

Properties of Nanocrystalline Thin Films of Metal and Metal Alloys Obtained at the Oil – Water Interface

Baxter, Sean. N.

Award date:
2023

Awarding institution:
Bangor University

[Link to publication](#)

General rights

Copyright and moral rights for the publications made accessible in the public portal are retained by the authors and/or other copyright owners and it is a condition of accessing publications that users recognise and abide by the legal requirements associated with these rights.

- Users may download and print one copy of any publication from the public portal for the purpose of private study or research.
- You may not further distribute the material or use it for any profit-making activity or commercial gain
- You may freely distribute the URL identifying the publication in the public portal ?

Take down policy

If you believe that this document breaches copyright please contact us providing details, and we will remove access to the work immediately and investigate your claim.

Properties of Nanocrystalline Thin Films of Metal and Metal Alloys Obtained at the Oil – Water Interface

Sean N. Baxter



PRIFYSGOL
BANGOR
UNIVERSITY

School of Chemistry
College of Physical and Applied Sciences

Submitted in accordance of the requirements for the
Degree of Doctor of Philosophy in Chemistry.

Supervisor Dr. P. John Thomas

April 2023

Statement of Originality

Yr wyf drwy hyn yn datgan mai canlyniad fy ymchwil fy hun yw'r thesis hwn, ac eithrio lle nodir yn wahanol. Caiff ffynonellau eraill eu cydnabod gan droednodiadau yn rhoi cyfeiriadau eglur. Nid yw sylwedd y gwaith hwn wedi cael ei dderbyn o'r blaen ar gyfer unrhyw radd, ac nid yw'n cael ei gyflwyno ar yr un pryd mewn ymgeisiaeth am unrhyw radd oni bai ei fod, fel y cytunwyd gan y Brifysgol, am gymwysterau deuol cymeradwy. Rwy'n cadarnhau fy mod yn cyflwyno'r gwaith hwn gyda chytundeb fy Ngoruchwyliwr.

I hereby declare that this thesis is the results of my own investigations, except where otherwise stated. All other sources are acknowledged by bibliographic references. This work has not previously been accepted in substance for any degree and is not being concurrently submitted in candidature for any degree unless, as agreed by the University, for approved dual awards.

I confirm that I am submitting this work with the agreement of my Supervisor.

Myfyrwyr/Student:

Sean N. Baxter

Roy Hatfield 1932 – 2023

Abstract

Thin films of metal and metal alloy nanocrystals have been prepared at the toluene–water interface. These self assembled thin films have been transferred to glass, polystyrene and PTFE substrates. The films have then been subjected to charge transport, catalysis and antibacterial studies. Studies showed manipulation of the gold:silver ratio of alloy films resulted in tuneable charge transport and catalytic characteristics. Antibacterial studies have also been used to demonstrate the activity of silver nanocrystal films on gram–negative bacteria.

Mae ffilmiau tenau o nanocrystalau metel a metel aloi wedi'u paratoi ar y rhyngwyneb tolwen–dŵr. Mae'r ffilmiau tenau hunan-ymgynnull hyn wedi'u trosglwyddo i swbstradau gwydr, polystyren a PTFE. Mae'r ffilmiau wedyn wedi bod yn destun trafndiaeth wefru, catalysis ac astudiaethau gwrthfacterol. Dangosodd astudiaethau fod trin y gymhareb aur:arian o ffilmiau aloi wedi arwain at gludiant gwefr tiwnadwy a nodweddion catalytig. Mae astudiaethau gwrthfacterol hefyd wedi'u defnyddio i ddangos gweithgaredd ffilmiau nanocrystal arian ar facteria gram–negyddol.

Acknowledgements

I would like to thank the following people, without whom I would not have been able to complete this thesis. My supervisor Dr John P Thomas, whose insight and knowledge into the subject matter and methods used helped to guide me through this research.

The 3rd and 4th year project students I had the pleasure of getting to know and help over the 4 years of research. The three Erasmus students; Karen, Manon, and Soraya who each had their own unique and individual style when it came to carrying out their work.

My colleagues in the School of Chemistry who made working as a Senior Demonstrator whilst carrying out the PhD such a pleasure. The technical staff: Denis Williams, Nick Welsby, Gwynfor Davies, David Hughes, and Glynne Evans, who were both colleagues and teachers. The office buddies Anna Zelma and Charlotte Booth, and the many conversations and adventures we had (the map was still on the wall when the building was handed over). Also, Dr Lorrie Murphy who has been most helpful in the final stages of writing and submission, since the University took the decision to close the School of Chemistry.

And my biggest thanks to my Family, both near and far. My wife, Charlotte for all the support you have shown me through this research, the culmination of many years of work and your encouragement to finally finish writing and submit and my children, Celyn and Harri who have no idea what this all means.

Contents

List of Figures	vii
List of Tables	xv
1 Introduction	1
1.1 History of Nanocrystals	2
1.2 Properties of Nanocrystals	3
1.3 Preparation Methods for Metallic Nanocrystals	9
1.4 Charge Transport Properties in Nanocrystals	16
1.5 Techniques for Characterisation of Nanocrystals	32
2 Experimental and Context	41
2.1 Thin Films of Metal and Metal Alloy Nanocrystals	41
2.2 Characterization Methods	44
2.3 Annealing Metallic Nanocrystals Deposited on Glass Substrates	45
2.4 Catalytic Studies of Nanocrystals	45
2.5 Preparation of a Single Phase Silver Nanocrystal Hydrosol	46
2.6 Inorganic Chalcogenide Ligand Synthesis	47
3 Thin Nanocrystalline Films of Metal and Metal Alloys	48
3.1 Introduction	48
3.2 Characterisation of Nanocrystalline Films of Metal and Metal Alloys	49
3.3 Influence of Annealing on the Morphology of Nanocrystalline Films	61
3.4 Investigation of Janus Nanocrystals Generated at an Interface	63
3.5 Conclusion	65
4 Charge Transport in Metal and Metal Alloy Nanocrystal Films	67
4.1 Introduction	67
4.2 Results and Discussion	68
4.3 Conclusion	74
5 Nanocrystal Metals and Metal Alloys as Nanocatalysts	77
5.1 Introduction	77

5.2	Nanocatalysed Reduction Reactions	78
5.3	Nanocatalysed Hydrogenation of Cyclohexene	86
5.4	Conclusions	87
6	Using Silver Nanocrystal Films as Antibacterial Coatings	90
6.1	Introduction	90
6.2	Results and Discussion	92
6.3	Conclusion	92
7	Summary and Future Work	95
	Bibliography	97

List of Figures

1.1	Typical sizes of small particles. The area shown, by the arrow, corresponds to the dimensions of nanoparticles.	1
1.2	The Lycurgus Cup showing the colour perceived in reflected light (left), and from internal illumination (right).	2
1.3	The plot shows the relationship between the particle size of gold and the corresponding melting point. The melting point decreases as the particle size decreases.	4
1.4	Diagram of the electronic band structure in metals, semi-conductors and insulators.	5
1.5	Diagram showing the effect of decreasing particle size (particle nuclearity) on the electronic structure of a metal.	6
1.6	The diagram shows the plasmon oscillations for a spherical particle, showing the displacement of the electron cloud.	7
1.7	The optical absorption spectra of gold nanoparticles of varying diameters. Notice the red shift with increasing particle size.	8
1.8	Schematic showing the two phase method for the generation of silver nanocrystals at the interface of toluene and water.	10
1.9	Schematic showing the concentration of the precursor at the interface. The vertical dotted lines show an area of water rich or toluene rich emulsion.	11
1.10	Diagram showing the variations in position of the particle at the interface with different contact angles.	12
1.11	Proposed reaction scheme for the synthesis of metal nanocrystals using THPC and metal salts.	13
1.12	Typical STEM (a) and HRTEM (b) examples of Au nanoparticles synthesised in the THPC method as a hydrosol (a) and water-toluene interface (b). The films of nanoparticles formed at the interface were deposited onto substrates and used directly.	14
1.13	A diagram showing an electrical equivalent circuit for an array of nanocrystals, shown in grey, and their capacitance linkers.	17
1.14	An equivalent circuit for the double barrier tunnelling junction. Showing the the junction each side of the nanoparticle island. Each junction can be modelled as a resistor and capacitor in parallel.	18

1.15	Set-point current dependence of the whole shape of Coulomb staircases. These curves are simulated by the orthodox theory using $R_1/R_2 = 1, 2, 5, 10, 20, 50, 100$ and 1000 , respectively (indicated by the dashed arrow in order). The circuit parameters are $R_1 = 0.1\text{--}100\text{ G}\Omega$, $R_2 = 0.1\text{ G}\Omega$, $C_1 = 0.16\text{ aF}$, $C_2 = 0.20\text{ aF}$, $Q_0 = 0e$ and $T = 4.2\text{ K}$. The vertical axis is normalized by multiplying R_1 to compare the whole shape of the Coulomb staircase. A higher R_1/R_2 value gives a sharper Coulomb staircase; in contrast, the shapes of the curves are not dependent on R_1/R_2 values under $R_1/R_2 > 50$	20
1.16	Plot of $\ln\sigma$ vs $1/T$. The straight lines show four different linear regimes for Activation energy with temperature change. Reprinted with permission from J. Am. Chem. Soc., 2012, 134 (29), 11888–11891. Copyright (2012) American Chemical Society.	22
1.17	Conductivity in nanocrystalline silicon films of a range of thickness's ($E_{31} = 1200\text{ nm}$ – $B_{22} = 170\text{ nm}$). Conductivity appears to be becoming independent of temperature at low temperatures.Reprinted from Journal of Non-Crystalline Solids, 299–302, Ram, Sanjay K. <i>et al.</i> , Investigations of the electron transport behavior in microcrystalline Si films, 411–415, Copyright (2002), with permission from Elsevier.	23
1.18	Ligand binding according to the covalent bond classification. ME represents a NC of binary <i>II – VI</i> , <i>IV – VI</i> , and <i>III – V</i> semiconductors (such as CdS). Reprinted with permission from J. Am. Chem. Soc., 2013, 135 (49), 18536–18548. Copyright (2013) American Chemical Society.	25
1.19	(a) Total structure of the $[\text{Au}_{25}(\text{SNaP})_{18}]^- [\text{TOA}]^+$ nanocluster ($\text{Au}_{25}\text{S}_{18}$ is shown in ball-and-stick mode, thiolate ligands and TOA^+ in wire-and-stick mode). (b) Icosahedral Au_{13} kernel. (c) Six dimeric $\text{Au}_2(\text{SR})_3$ staple motifs. Gold, green or orange; sulfur, yellow; carbon, gray; hydrogen, white; TOA, magenta. Reprinted with permission from ACS Nano, 2016, 10 (8), 7998–8005. Copyright (2016) American Chemical Society.	27
1.20	Scheme showing the ligand exchange process used for preparation of all-inorganic nanocrystals.Reprinted with permission from J. Am. Chem. Soc., 2010, 132 (29), 10085–10092. Copyright (2010) American Chemical Society.	28
1.21	TEM images of 9.1 nm CdSe, A, and 5 nm Au, B, NCs capped with $\text{Sn}_2\text{S}_6^{4-}$ ligands.Adapted with permission from J. Am. Chem. Soc., 2010, 132 (29), 10085–10092. Copyright (2010) American Chemical Society.	29
1.22	Simplified schematic diagram of the Scanning Electron Microscope.	33

1.23	SEM image showing Escherichia coli (E.coli) adhered to a silver nanocrystal film previously deposited on a microscope slide substrate.	34
1.24	Schematic of a Transmission Electron Microscope, showing the internal components. Schematic copied from http://www.hk-phy.org	35
1.25	TEM of Au _{0.5} Ag _{0.5} nanocrystals generated at the water toluene interface. Films were sonicated in chloroform to distribute the nanocrystals an a single drop of the mixture was pipetted on to a holey carbon copper TEM grid. The scale bar shows 10 nm.	35
1.26	Cartoon showing the generation of a photoelectron from an X-ray photon.The X-ray photon strikes the sample(Left), knocking out an electron(Right). . . .	36
1.27	Schematic of a typical AFM instruments internal workings. The deflection of the tip is measured using a reflected laser beam.	37
1.28	An example of 2D Miller Indices.	38
1.29	XRD pattern of Ag taken from JCPDS file no. 04-0783. The Miller indices have been labelled above the peaks.	40
2.1	Photographs showing the silver film at the water–toluene interface. Notice the reflective appearance of the film.	42
2.2	Photographs showing the silver film supported on polystyrene (left) and 1.5 x 1.5 cm glass supports (right). Note the reflection shown by the silver on glass.	43
2.3	Photographs showing the UHV rig (left) and a sample post measurement (right).	44
3.1	X–ray diffraction patterns of a silver (black) and gold (blue). Cubic Au and Ag reference data from using collection codes 604631 (Ag) an 64701 (Au) has been included. The data has been stacked for clarity. Films all generated at the interface of toluene and water for 3 hours at 50°C. Films were then deposited onto glass substrates.	49
3.2	X–ray diffraction pattern of pure palladium . Cubic palladium reference data from collection code 648676 has been included and data stacked for clarity. Cracked and broken films were prepared at the interface of toluene and water after 3 hours at 50°C. It was then possible for fragments to be deposited onto glass substrates for analysis.	50
3.3	X–ray diffraction patterns of a silver (black), gold (blue) and silver–gold alloy (red) film on glass. Films all generated at the interface of toluene and water for 3 hours at 50°C. Films were then deposited onto glass substrates.	51

3.4	X-ray diffraction patterns of AuPd nanocrystal films on glass and polystyrene (inset). Peaks shown refer to the miller indices (111) and (200). Films are all generated at the interface of toluene and water for 3 hours at 50°C. Films were then deposited onto glass substrates or polystyrene beads added to the toluene phase post film generation. Toluene was left to evaporate leaving a polystyrene backed nanocrystal film.	52
3.5	Ag _{0.50} Pd _{0.50} nanocrystal film on glass. Miller indices (111) and (200) for both silver and palladium are shown from reference data. Films all generated at the interface of toluene and water for 3 hours at 50°C. Films were then deposited onto glass substrates or polystyrene added to the toluene phase post film generation. Toluene was left to evaporate leaving a polystyrene backed nanocrystal film.	53
3.6	Scanning electron microscope (SEM) images of Ag films deposited on glass at (A) 3000x and (B) 10000x magnification.	53
3.7	Scanning microscope images of films deposited on glass. (A) High magnification image of Au nanocrystal film. The visible cracks are due to solvent evaporation post-deposition. (B) low magnification image of the same film, showing the continuous and uniform deposit over several square millimetres. (C & D) Low and high magnification images of Ag nanocrystal films deposited on glass. (E & F) Low and high magnification images of Au _{0.50} Ag _{0.50} nanocrystal films deposited on glass.	54
3.8	(A)TEM image showing several Ag nanocrystals. (B) Selected area diffraction pattern of a typical Ag nanocrystal showing evidence of polycrystallinity. . .	55
3.9	TEM images of (A) gold and (B) palladium nanocrystals, scale bar shows 20 nm. Inset particle size histograms.	56
3.10	TEM image of pure palladium nanocrystals prepared at the interface of toluene and water, 50°C 3hours. The scale bar shows 100 nm.	57
3.11	HRTEM-HAADF images showing Au _{0.50} Pd _{0.50} alloy (middle). The gold content (left, red) and palladium content (right, green) have been calculated using EDS and shown as a colour map.	57
3.12	HRTEM-HAADF images showing two areas of nanocrystals from a Ag _{0.50} Pd _{0.50} alloy synthesis (middle). The silver content (left, red) and palladium content (right, green) have been calculated using EDS and shown as a colour map. The top images indicate a silver rich alloy fragment and bottom images a palladium rich alloy fragment.	58

3.13	3D surface profile showing a silver nanocrystal film on glass substrate.	58
3.14	XPS spectra obtained from the silver nanocrystal film survey scan (A). High resolution scans over Ag 3d, O 1s, C 1s, and P 2p are also shown (B-E).	59
3.15	Photograph showing the extent of material loss after annealing (right), compared to a freshly prepared substrate (left). Notice how after annealing the film loses its reflective sheen as material is lost.	61
3.16	X-ray diffraction of silver films before and after annealing. Films were held at the temperatures shown for 3 hours before being left to cool in the furnace. The data has been stacked for clarity.	62
3.17	X-ray diffraction of gold films before and after annealing. Films were held at the shown temperatures for 3 hours before being left to cool in the furnace. Data has been stacked for clarity.	62
3.18	NOESY NMR spectra showing the silver nanocrystals generated at the toluene-water interface. Samples were deposited on glass substrates and later sonicated in d-chloroform to produce a suspension for NMR analysis. The peak at 4.2 ppm is believed to be from trace H ₂ O/D ₂ O contamination.	64
3.19	NOESY NMR spectra showing single phase methanol/water generated silver nanocrystals. Nanocrystal suspensions were evaporated to dry and later sonicated in D ₂ O to create a suspension for NMR analysis.	65
4.1	Examples of some inorganic ligands surrounding a nanocrystal. (Top - clockwise) chalcogenide, metal chalcogenide, metal halide, halide and pseudohalide ions	68
4.2	Plots showing temperature dependence of the nanocrystal films resistance for different alloy compositions (labelled). A break has been used from 70 Ω to 100k Ω . The plot in top left shows data for Ag films, where resistance decreases $\approx 10\%$ with decreasing temperatures. The top right shows Au, with resistance increasing from 2.1 M Ω to 2.35 M Ω	69
4.3	Plot showing the change in natural log of conductivity, $\ln(\sigma)$ against the inverse temperature for a pure Au nanocrystal film. Two distinct linear regimes have been identified in red. Inset shows results from Ag _{0.50} Au _{0.50} deposits.	70

4.4	Plots showing temperature dependence of resistance for pure Au deposits annealed at selected temperatures. A break in the Y axis has been used between 40M Ω and 60M Ω . The plots on top show change in natural log of conductivity, $\ln(\sigma)$ against the inverse temperature for a pure gold nanocrystal films annealed at 120°C (Left) and 180°C(Right).	72
4.5	Diagram showing the ligand exchanges used. Top centre shows the supporting ligands expected after the generation of the nanocrystal arrays. Yellow shapes represents the metal nanoparticle with the attached ligands.	73
4.6	Plot of resistance against temperature for various Ag films after ligand exchange. The resistance drops with temperature as is expected for a metal conductor. . .	74
4.7	Plot of resistance against temperature for as prepared Au films and Au films with exchanged ligands. A break has been used between 3M Ω and 50M Ω . .	75
5.1	Proposed mechanism for the reduction of 4-nitrophenol to 4-aminophenol on the surface of metallic nanocrystals.	79
5.2	4-Nitrophenol in aqueous, basic and acid conditions showing how the UV/Vis profile changes as the -OH group interacts in the conditions.	80
5.3	Simple schematic reaction equation for the catalysed reduction of nitrobenzene to aniline.	80
5.4	The Haber mechanism for nitrobenzene reduction to aniline, originally proposed in 1898.	81
5.5	(LEFT)UV/Vis absorption spectra for a solution of 4-nitrophenol with sodium borohydride in the presence of a Ag film deposited on Whatman™ PTFE membrane. Abs. are arbitrary units of absorption and time indicates minutes since addition of sodium borohydride. (Right) $A/A_{t=0}$ against time. Where A is absorption at time and $A_{t=0}$ is initial absorption, before addition of sodium borohydride.	82
5.6	UV/Vis absorption spectra for a solution of 4-nitrophenol with sodium borohydride in the presence of Ag _{0.5} Pd _{0.5} (Left), Au _{0.5} Ag _{0.5} (Middle) and Ag _{0.5} Pd _{0.5} (Right) alloy films deposited on Whatman™ PTFE membrane. Abs. are arbitrary units of absorption and time indicates minutes since addition of sodium borohydride.	82

5.7	Plots of $A/A_{t=0}$ against time for $\text{Ag}_{0.5}\text{Pd}_{0.5}$ (Left), $\text{Au}_{0.5}\text{Ag}_{0.5}$ (Middle) and $\text{Ag}_{0.5}\text{Pd}_{0.5}$ (Right) nanocatalysts performance for multiple reactions recycling the original supported catalyst. Data has been shown for the initial, second and fifth cycle. Where A is absorption at time and $A_{t=0}$ is initial absorption, before addition of sodium borohydride. Between each use the nanocatalyst was washed gently with water to remove any loosely adhered reactants.	83
5.8	UV/Vis absorption spectra for a solution of nitrobenzene with sodium borohydride in the presence of a Ag film deposited on Whatman™ PTFE membrane (Top). The catalyst was removed washed and recycled twice after the initial cycle. UV/Vis absorption spectra for recycling shows some retained reduction activity (Bottom). Abs. are arbitrary units of absorption and time indicates minutes since addition of sodium borohydride.	84
5.9	UV/Vis absorption spectra for a solution of nitrobenzene with sodium borohydride in the presence of a virgin $\text{Ag}_{0.5}\text{Pd}_{0.5}$ film deposited on Whatman™ PTFE membrane (Left). The catalyst was removed washed and recycled after the initial cycle (Right). Abs. are arbitrary units of absorption and time indicates minutes since addition of sodium borohydride.	85
5.10	Proton NMR of cyclohexene in CDCl_3 . Peaks have been assigned and identified on the inset molecule.	86
5.11	Proton NMR of crude reaction liqueur in CDCl_3 after heating for 5 hours under H_2 atmosphere in the presence of a $\text{Au}_{0.5}\text{Pd}_{0.5}$ nanocatalyst supported on Whatman™ PTFE membrane circle. A small new peak at 1.43 ppm can be seen, relating to cyclohexane.	88
6.1	Scanning electron microscopy of the AgNC films. (A) Control sample of Ag unexposed to bacteria. (B and C) E. coli adhered to a reference glass microscope slide, incubated for 24 hours. (D-G) E. coli adhered to AgNC films after 24 h of incubation, Denatured E. coli cells have been circled.	91
6.2	Fluorescence micrographs of (A) E. coli adhered to a reference glass microscope slide and (B) an AgNC film after 6, 12 and 24 h incubation. The scale bar shown in the top left of each image is 100 μm . The green fluorescent staining indicates live cells and the red dead cells. Some of the images (such as B-12 h) appear green, but on closer inspection the interior of the bacteria cell is red, indicating death, and the green is the outer cell membrane casing.	93

S1	Proton NMR of crude reaction liqueur in CDCl_3 after heating for 5 hours under H_2 atmosphere in the absence of a catalyst.	113
S2	Proton NMR of crude reaction liqueur in CDCl_3 after heating for 5 hours under H_2 atmosphere in the presence of a $\text{Ag}_{0.5}\text{Au}_{0.5}$ nanocatalyst supported on Whatman TM PTFE membrane circle.	114
S3	Proton NMR of crude reaction liqueur in CDCl_3 after heating for 5 hours under H_2 atmosphere in the presence of a $\text{Ag}_{0.5}\text{Pd}_{0.5}$ nanocatalyst supported on Whatman TM PTFE membrane circle. A new peak at 1.43 ppm can be seen, relating to cyclohexane.	115

List of Tables

- 3.1 XPS surface composition results from a silver nanocrystal film deposited on glass. 60

Chapter 1

Introduction

Nanomaterials are particles between the size of 1 and 100 nm. Figure 1.1 shows where nanoparticles fit when compared to some other small particles. Nanocrystals (NCs) form an interesting topic within the field of nanoscience. The joint role of size and composition in regulating material properties lies at the heart of nanoscience and technology. Nanocrystals bridge the gap between molecules that possess distinct individual properties and bulk systems that acquire characteristics from a lattice that extends to infinity.

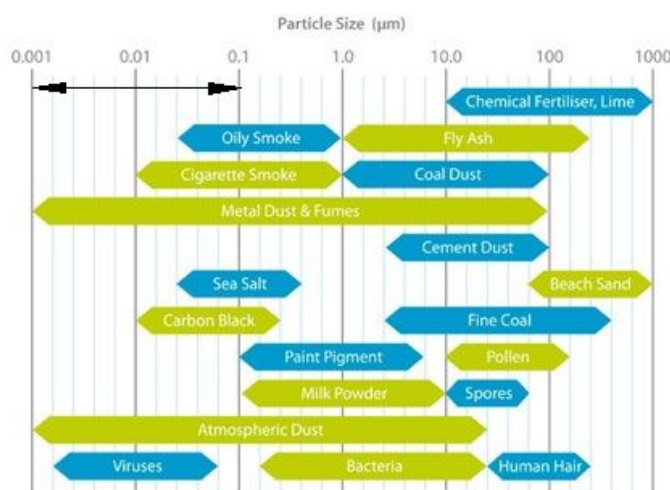


Figure 1.1 – Typical sizes of small particles. The area shown, by the arrow, corresponds to the dimensions of nanoparticles.

It is possible for nanocrystals to exist in a range of shapes, or morphologies. Superstructures of NCs have been identified as 3D arrays of spherical particles, 2D platelet structures and 1D rod structures.^{1,2} Strikingly, the properties of nanocrystals: chemical, physical, electronic and even thermodynamic are determined not just by the chemical identity but also by the dimension of the crystallites.^{1,3–6} Nanocrystallites of metal and semiconductors are vital ingredients in potential devices such as, electrical and electrochemical sensors, solar cell



Figure 1.2 – The Lycurgus Cup showing the colour perceived in reflected light (left), and from internal illumination (right).

devices,^{7,8} plasmonic devices,⁹ data storage elements,⁴ field effect transistors¹⁰ and light-emitting diodes.¹¹

Additionally, ligands that bind to the surface of nanocrystallites and prevent aggregation are important in determining the physics and chemistry of the particulate systems. For example, the dispersibility of particles in a particular solvent are nearly entirely determined by the ligand shell. Condensed nanocrystalline solids are made up of an appreciable quantity of surface species as the crystallites possess high specific surface area. Hence, ligands play a key role in assembly, structure and enabling smooth charge transport through nanocrystalline arrays.

Designing nanocrystalline materials for the future calls for an understanding of the effects of size, ligand shells and charge transport (CT) mechanism on properties. This chapter will initially focus on the CT theories and provide a brief overview of the mechanisms pertinent to the area. Later, more recent work on ligand shells of NC materials and their effects on the CT is highlighted.

1.1 History of Nanocrystals

Nanocrystals are not a new discovery. The term *nano* hails from the Greek word of nanos or dwarf. Their properties have been exploited since days of old, even if the reasons behind these properties were unknown. Colloids of nanoparticles can be traced as far back as the fourth century, where they were used in the dying of glasses and fabrics and also as a therapeutic aid

in arthritis treatment.^{12,13} It was common place to use gold and silver nanoparticles to colour glasses. an example of this is the Roman Lycurgus Cup (Figure 1.2) which forms part of the British Museum Collection. The Au–Ag colloids in the glass give rise to a brilliant red colour when illuminated internally and a deep green in normal reflected light.

Andrew Cassius reported the thermal stability of gold and tin oxide colloids, and they became fashionable for use in glasses as colourants.¹⁴ A popular dye, The Purple of Cassius, which was used in olden days was formed in the reaction of stannic acid and chloroauric acid. It is actually made from tin oxide and gold nanocrystals.¹⁴ Maya blue a 7th century blue dye used by Mayas has been found to consist of metal and oxide nanocrystals as well as indigo and silica.¹⁵ Michael Faraday gave a groundbreaking lecture in 1857 entitled "Experimental Relations of Gold (and other metals) to Light",¹⁶ in his talk he detailed the then current theories for the interaction of light with metal particles in solution. He correctly postulated that light interacted with the particles in the solutions, even though the technology at that time did not exist to be able to visualise the particles.

These early advances although promising did not lead to continued research of nanoparticles. The field has become much greater in more recent years with researchers working to identify and characterise new and interesting nanocrystals, as well as propose ever exciting and useful applications.

1.2 Properties of Nanocrystals

Nanocrystals possess interesting properties that differ from those expected when thinking about the bulk material. The properties such as, melting point, catalytic activity, hardness, colour and conductivity, all alter with dimension of the particles in question. These properties bridge the gap between bulk macroscopic chemistry, single atom or small molecules. For example the surface area to volume ratio for a gold cluster nanoparticulate containing 13 atoms, of which 12 are surface atoms (irrespective of the packing), is 92%. Incredibly larger than that of bulk matter, the nanoparticulate has a surface more populated than the bulk. As a comparison if we think about the reactivity of organic molecules we think about the effects caused by bulky groups, the physical dimensions normally don't matter, except where the cavity can accommodate a guest species.¹⁷ These surface to volume ratio properties have a dramatic effect on many of the other properties manifested in the nanomaterial. The

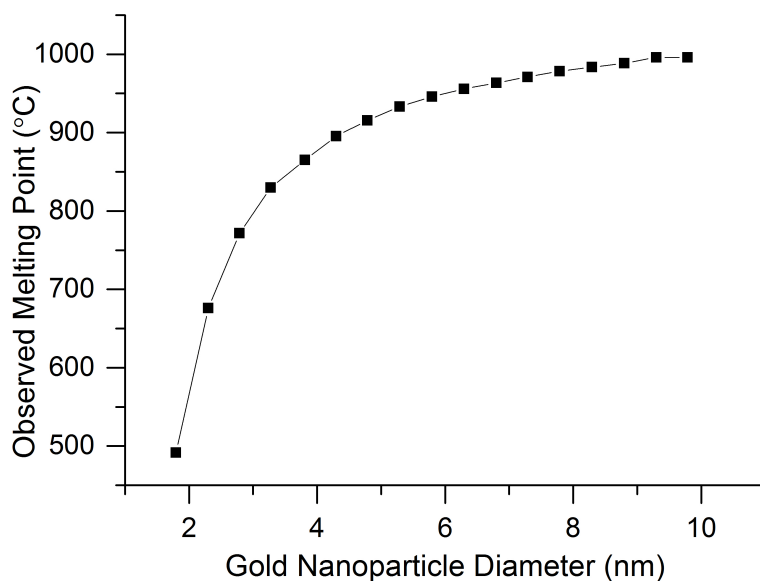


Figure 1.3 – The plot shows the relationship between the particle size of gold and the corresponding melting point. The melting point decreases as the particle size decreases.¹²

melting point has been shown to decrease with particle size. Investigations involving gold nanoparticles showed that as the particle size decreased the melting point of the particles also decreased (Figure 1.3).^{12,18} The property has also been studied and identified in other metal nanocrystals.^{19,20}

1.2.1 Electronic Properties of Nanocrystals

Electronic band theory states that electrons can only have quantised energies which fit into a range of energy bands. These bands are arranged between the ground state, where electrons are bound to the atomic nuclei of the particle, and the free electron energy state, which is a description of the energy required for an electron to escape from the particle entirely. Most of these lower states are filled with electrons, up to a particular band called the valence band. A simplified model, ignoring symmetry, to start to explain this.

In atoms the structure is well defined and has discrete energy levels. When two atoms join their atomic orbitals overlap and turn into molecular orbitals. As the number of atoms joining increases the number of molecular orbitals increases and as a consequence, the difference in energies between the bonding and antibonding becomes much smaller. In solids these levels form continuous bands of energy, rather than the discrete energy levels described above.²¹ However it is possible to have intervals of energy containing no orbitals, irrespective of the number of atomic orbitals combined, forming a band gap. The bands can have different gaps

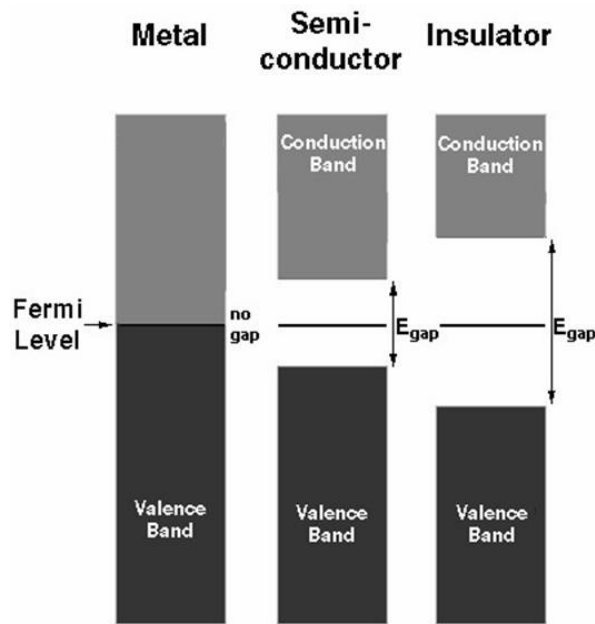


Figure 1.4 – Diagram of the electronic band structure in metals, semi-conductors and insulators.^{1,21}

between them, relating to the properties of the material. It is also possible for the bands to overlap and produce a single large band, as seen in metals. Under certain conditions these band gaps lead to the different classes of solids, metals (conductors), semiconductors (intrinsic and extrinsic) and insulators. The valence band in metals can be viewed as half full, at room temperature no additional energy is required for electrons to conduct. The band gap in insulators is sufficiently large enough that it is difficult to promote electrons from the valence band into the conduction band. Leading to very low electrical conductivity.(Figure 1.4) Semiconductors still contain a band gap between the valence band and conduction band, but a smaller one than found in insulators. The energy taken to promote an electron from the valence band to the conduction band depends on the size of the band gap, serving as the dividing line between insulators and semiconductors. For a semiconductor to conduct an electron needs to be promoted to the conduction band. Generally the energy is provided through thermal excitation (k_bT). Therefore conduction in semiconductors is strongly dependent on temperature. Electrons promoted will leave behind a positive hole, the excited electron-hole pairing is called an exciton. The hole is able to be filled by neighbouring electrons, giving the appearance of hole movement. The combined movement of holes and electrons forms the electrical conduction in semiconductors.

A metallic state forms when a continuum of energy levels above the Fermi level exists. The electrons are readily and easily promoted to the conduction band. It is here that quantum

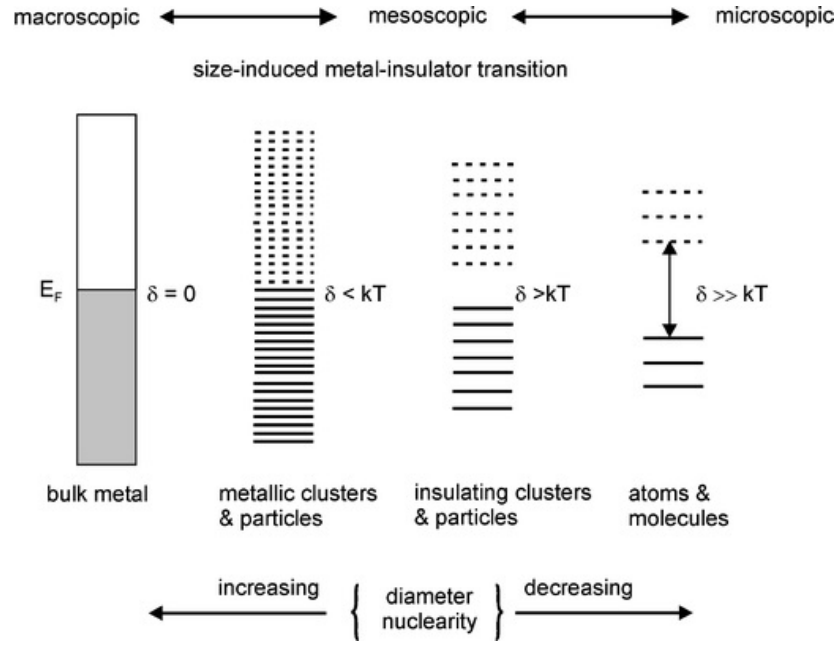


Figure 1.5 – Diagram showing the effect of decreasing particle size (particle nuclearity) on the electronic structure of a metal.²²

size effects begin to dominate in the electrical properties. On size decrease the continuum of electronic states breaks down leading to the metals becoming more insulating.

For sufficiently small sizes of metallic nanocrystals, discrete energy levels become resolved as the full width of the bands in bulk have not developed. Bands which would overlap in the bulk have not yet developed at the smaller particle sizes, due to symmetry prohibiting greater overlap. A gap begins to form leading to a lifting of the degeneracy of energy levels. Having the consequence that nanoscopic amounts of a metal may behave as a semiconductor or as an insulator, depending on the number of atoms and on the shape of the particle, i.e a 'Size Induced Metal to Insulator transition' occurs (Figure 1.5).²² The discreteness of the levels, Kubo Gap, can be measured in terms of the average spacing between successive quantum levels (δ). It is given by,

$$\delta = \frac{4E_f}{3n} \quad (1.1)$$

Where E_f is the Fermi energy level of the bulk metal and n is the number of valence electrons in the nanoparticle.^{1,23} In reality it is more nuanced in the case of semiconductors where the top of the conduction band and the bottom of the valence band are discretised by differing amounts.

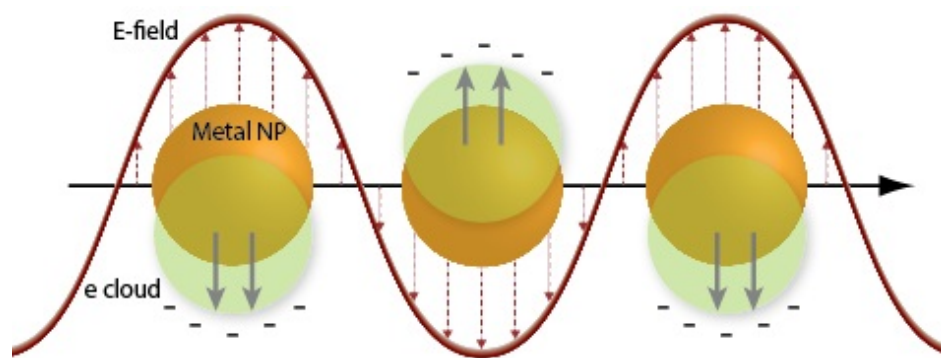


Figure 1.6 – The diagram shows the plasmon oscillations for a spherical particle, showing the displacement of the electron cloud.⁶

Thus, for a 3 nm diameter Ag nanoparticle that contains around 103 atoms, the value of δ would be 5–10 meV. Since at room temperature, $k_bT \approx 25$ meV, the 3 nm particle would be metallic, as $k_bT > \delta$. As temperatures decrease sufficiently the Kubo Gap becomes greater than the available energy k_bT , causing non-metallic properties. Discreteness of energy levels also brings about changes in the spectral features, especially those related to the valence band.

1.2.2 Catalytic Properties of Nanocrystals

One important use of nanocrystals is for catalysis. Catalytic properties of nanocrystals are largely due to higher specific surface area and coordinatively unsaturated surface, edge and corner atoms, compared to the bulk material.²⁰ The ability to generate different shapes of nanocrystals, with open faces and edges, can result in tunable catalysts. The exposed atoms exhibit catalytic activities due to the ability to interact with species in the surrounding area.²⁴ In homogeneous catalysis colloidal solutions of nanocrystals are dispersed into the reaction media.²⁰ The reactive unsaturated surface sites can also lead to agglomeration of nanocrystals within the homogeneous solutions increasing particle size, as particles combine, lowering their much favoured large surface atoms:bulk atoms ratio and reducing activity.²⁵ Agglomeration can be mitigated through supporting nanocrystals on surfaces or incorporating with larger particles for use as heterogeneous catalysts. Attaching nanocrystals on to supports, such as carbon nanotubes, polymers, magnetic compounds and titania, is believed to increase the stability and reuseability, through halting the agglomeration and easing the recollection and recycling of the catalyst.^{24,26–29} It has been shown over previous years that nanocrystals perform well as suitable nanocatalysts, both in solutions and when incorporated into supports. They have demonstrated their use as oxidation, hydrogenation and carbon–carbon coupling catalysts.^{20,26–29}

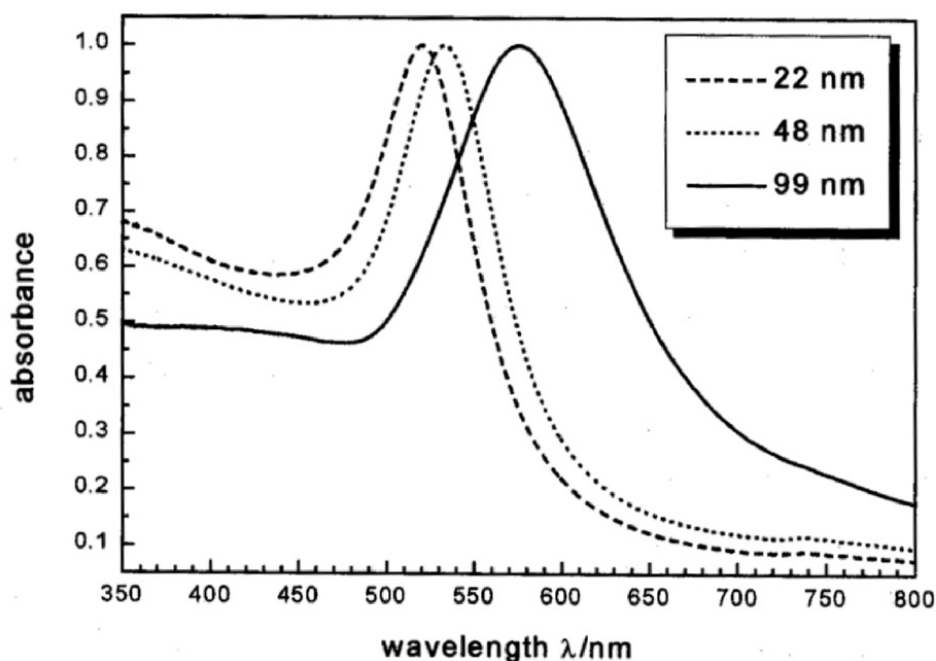


Figure 1.7 – The optical absorption spectra of gold nanoparticles of varying diameters. Notice the red shift with increasing particle size.³³

1.2.3 Optical Properties of Metal Nanocrystals

Optical properties in nanocrystals are dictated by the surface plasmon band. Coherently localised oscillations of the free conduction band electrons.^{30,31} The interaction of a plasmon and electric field is shown in (Figure 1.6). These electrons are polarisable and can lead to light being absorbed or scattered by the metal nanocrystals leading to a wide variety of optical phenomena.^{17,23,31} Surface plasmons are localised to the surface of the nanocrystal, localised surface plasmon resonance, and cannot spread as they would in a bulk material. Gustav Mie used Maxwell's equation to describe the interaction of light with metal nanocrystals. Where the spherical size of the nanocrystal was far less than the wavelength of light used, the oscillation will be dominated by polarisability.^{6,30,32} A large polarisation generates a strong local electric field enhancement on the surface as well as large light absorption and scattering at the surface plasmon frequency. The surface plasmon resonant frequency is strongly influenced by the size, shape, interparticle interactions and environment of the nanocrystal. For instance, it is known that gold nanocrystals in solution have a plasmon band of $\approx 520\text{ nm}$ increasing the particle size causes red shift and decreasing particle size causes blue shift (Figure 1.7), allowing for a degree of tunability.³³ Silver also shows the same trend.³⁴ The intensity of absorption lessens with particle size as there are fewer itinerant electrons to cause the effect.²³ Plasmon bands can be identified even in the presence of

stabilising ligands. It is possible to use them for probing growth and agglomeration as well as chemisorption on the nanocrystal surfaces. Ligands based on thiols have been shown to cause dampening of the plasmon band with increases in ligand concentration.³⁵

1.3 Preparation Methods for Metallic Nanocrystals

There are many methods for the synthesis and preparation of nanocrystals. Physical methods generally involve the evaporation of a solid metal, forming a saturated vapour from which homogeneous nucleation of nanoparticles can occur, growth is rapid and can be controlled using precise control over experimental conditions.¹ Chemical methods are useful for preparation of nanocrystals of both metals and semiconductor materials. Chemical methods are generally performed under mild conditions, are reasonably straight forward and have been reviewed many times.^{20,27,36} Most chemical methods produce solutions of nanocrystals supported with ligands to reduce coagulation and falling out of solution. When discussing reactions resulting in solutions there are three steps, seeding of the material, particle growth and finally termination by capping ligand.^{1,23} These solutions can be either, hydrosols - stabilised sterically and electrostatically, or organosols - stabilised sterically. Using polymers such as starch, cellulose, polyvinylpyrrolidone, and polyvinyl alcohol allowed the sols produced to be redispersed if the particles crashed out of the solution. There are multiple chemical methods for metal nanocrystals include reduction of metal salts, using borohydride, citrate alcohol, tetrakis(hydroxymethyl)phosphonium chloride (THPC), alkylaluminates and water gas (CO & H₂ mix). Solvothermal synthesis, where solvents are used at temperatures high above the their boiling point. Photochemical, where light is used to induce decomposition of the metal salt through generation of reducing agents. Electrochemical, where size of nanocrystals can be tuned varying the current density. Arrested precipitation, which makes use of the capped nanocrystals affinity to the pH of their supporting solution. Thermolysis, where reagents are injected into boiling solvents. Liquid–liquid interface, the method used in this thesis, shall be discussed in more detail below.

1.3.1 Preparation of Thin Films at the Liquid–Liquid Interface

It is possible to prepare smooth, continuous, films of metal nanocrystals of thickness ≈ 100 nm (Figure 1.8).³⁷ The first reported preparation of films at the liquid–liquid interface was in 1988.³⁸ Yogeve and Efrima proposed the use of a water–dichloromethane interface with silver nitrate being reduced to silver using hydrazine sulfate. These metal liquidlike films (MELLF) were unstable and over time the interface film would redissolve into the organic phase causing

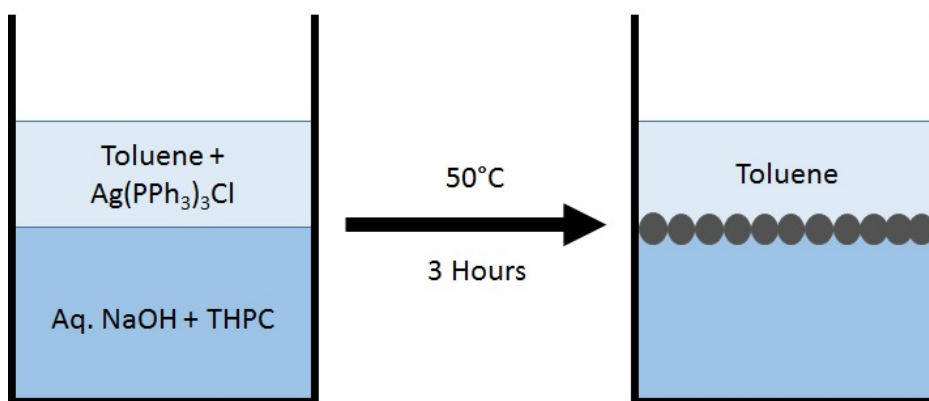


Figure 1.8 – Schematic showing the two phase method for the generation of silver nanocrystals at the interface of toluene and water.

a darkening of the dichloromethane, eventually depositing on the bottom of the vessel. The method was further improved by Rao *et al.* in 2003 by utilising the toluene–water interface employing the interaction of metal–triphenylphosphine complexes in the toluene layer and partially hydrolysed tetrakis(hydroxymethyl)phosphonium chloride in the aqueous layer.^{39,40} The method has since been used to prepare metals, such as gold, silver and palladium, metal oxides and hydroxides, such as copper hydroxide and zinc oxide, and metal chalcogenides, such as copper and cadmium sulfides.^{40–46} The reactions which are of most interest are those that derive precipitates through a simple and exceptionally benign method.

It is difficult to illustrate the true interface as it is a complex and dynamic environment, which changes with temperature and interfacial tension. Spectroscopic evidence suggests that the interface can be viewed as a sharp boundary roughened by ripples.³⁹ Realistic measurements suggest an interface width of 2 nm between water and most organic solvents. The model however may not match reality. If we think about a polar organic liquid it will have greater interactions with the water phase and the interface would be much wider. It is also believed that specific orientations of molecules at the interface will be favoured, The –OH of water will dangle across the interface and into an organic liquid.⁴⁷ For polar liquids there is evidence that an electrical double layer forms across the interface.⁴⁸

However the accepted model for the toluene–water interface allows the slow diffusion of solvents from one phase into the other, allowing for the reduction reactions to take place. The width of the pseudo interface mixture is, again, dynamic and dependent on temperature and interfacial tension. Figure 1.9 shows the density profile across the interface which is smooth

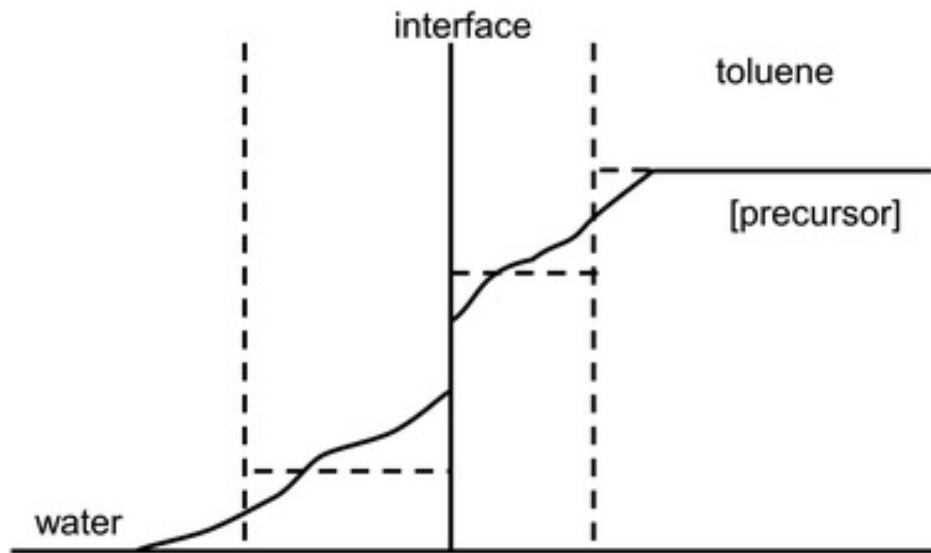


Figure 1.9 – Schematic showing the concentration of the precursor at the interface. The vertical dotted lines show an area of water rich or toluene rich emulsion.³⁹

rather than sharp. As ions diffuse across they disturb the interface and, it is believed, if an ion is strongly hydrated enough it may keep some of its original hydration shell as it passes into the other phase.⁴⁹

Adsorption of particles on the interface is driven by the systems need to reduce the interfacial tension between the toluene and water phases, as a film forms the tension lessens. To generate stable films the sum of surface tensions between the toluene–solid interface, $\gamma_{s/o}$, and water–solid interface, $\gamma_{s/w}$, must be less than the surface tension of the toluene–water interface, $\gamma_{w/o}$. There is a strong dependency on the contact angle of the particles at the interface (Figure 1.10). If a particle is hydrophilic it will position itself more in the aqueous phase, where as a hydrophobic particle will sit more in the organic phase. The Young-Dupré equation relates the surface tensions with the contact angle:²

$$\cos \theta_{w/o} = \frac{(\gamma_{s/w} - \gamma_{s/o})}{\gamma_{w/o}} \quad (1.2)$$

When $\theta = 90$ the maximum stability of the interface is seen, as would be expected when producing a film which perfectly separates the two phases, all other cases would involve one phase or the other being preferred.⁵⁰ The interfacial trapping is also strongly determined by the reduction in surface energy.

$$\Delta G = \pi r^2 \gamma_{wo} (1 - \cos \theta_{w/o})^2 \quad (1.3)$$

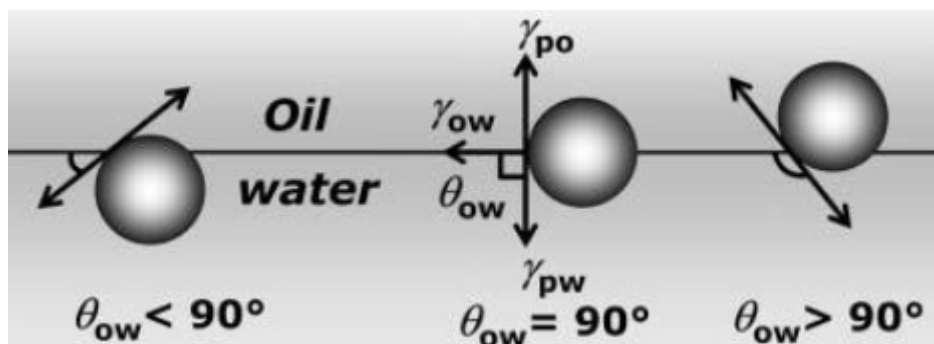


Figure 1.10 – Diagram showing the variations in position of the particle at the interface with different contact angles.⁵¹

Where ΔG is the reduction in surface energy, γ_{wo} is the interfacial tension of the solvents being used and $\theta_{w/o}$ measures the contact angle between the particle surface and the interface. For small particles the energy reduction is suitably large ($k_bT > 10^7$), and causes irreversible self assembly, producing very stable films.²

The reducing agent employed to generate the metal nanocrystals has two functions, principally it is there to reduce the metal ions in solution to metal nanocrystals, secondly and helpfully it also doubles up as a stabilising ligand.^{52,53}

1.3.2 Tetrakis-(hydroxymethyl)-phosphonium chloride

Tetrakis-(hydroxymethyl)-phosphonium chloride (THPC) was initially reported in 1921 by Hoffman.⁵⁴ Originally unsure, Hoffman later established the accepted structure and synthesised derivatives.⁵⁵ During these investigations it was identified that THPC decomposed in the presence of aqueous alkali hydroxides to form tris(hydroxymethyl)phosphine oxide (THPO) as well as formaldehyde and tris(hydroxymethyl)phosphine (THP) (Figure 1.11).^{56,57}

Duff *et al.* first proposed, in 1993, using THPC as a reducing agent for the reduction of metals, with the dual role of stabilizing in aqueous medium.⁵⁸ It was developed as a possible replacement for the traditional Faraday synthesis of gold colloids, which employed diethyl ether solutions of white phosphorus.¹⁶ Using THPC Duff *et al.* were able to produce gold colloids containing ultrafine phosphorus containing gold particles at high concentrations with a mean diameter between 1–4 nm, much smaller than the other methods of the time.^{58–61}

Two decades later more extensive studies on the action of THPC in the reduction of metal ions were undertaken.⁵³ During the study an overall reaction scheme was proposed, shedding light on the role played by THPC and formaldehyde (Figure 1.11). Using THPC it is

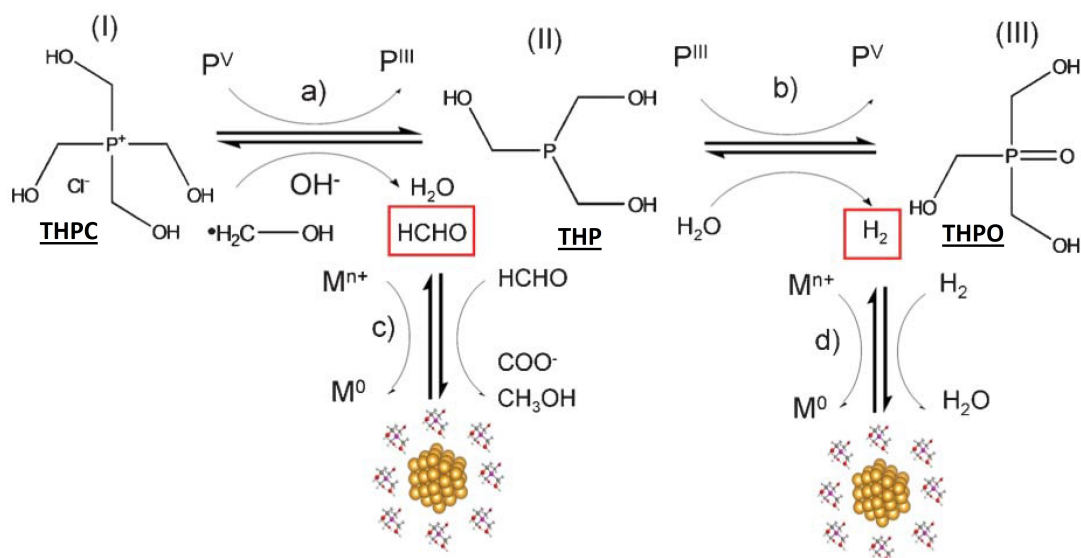


Figure 1.11 – Proposed reaction scheme for the synthesis of metal nanocrystals using THPC and metal salts.⁵³

possible to chemically reduce metal salt precursors, in both aqueous and organic solvents, to successfully obtain metallic nanostructures. It has been shown that nanostructures of; gold, silver, palladium, platinum and ruthenium as well as bi-metallic and tri-metallic nanostructures can be made.^{53,58,60–65} Reductions have been carried out in single and two phase systems, where the reducing agent and metal precursor are introduced in separate phases.^{39,40,66}

Role of THPC in reductions

THPC (structure I in Figure 1.11) converts to THPO (structure III in Figure 1.11) via THP (structure II in Figure 1.11) in the presence of hydroxide ions. Formaldehyde and hydrogen are produced during the process.⁵³ THPO adsorbs onto the surface of nanoparticles as a protecting ligand and quenches nanoparticle growth.⁶⁵ Experiments testing the stabilizing role of THPC as a ligand, the need for basic hydroxide conditions to activate the reducing power and the influence of formaldehyde have been undertaken by Hueso *et al.*. Using an aqueous solution of chloroplatinic acid and THPC it was shown that the reaction did not proceed in the absence of sodium hydroxide. On the addition of formaldehyde the reaction was able to proceed as normal producing well-crystallised Pt nanoparticles of 1.5 nm diameter. Proving that the THPC freely reacts with hydroxide ions generating the formaldehyde, *in situ*, which can then reduce the metal salts.⁵³ To test the stabilizing role that the THPC played, the reaction was performed in the absence of THPC with formaldehyde employed as the

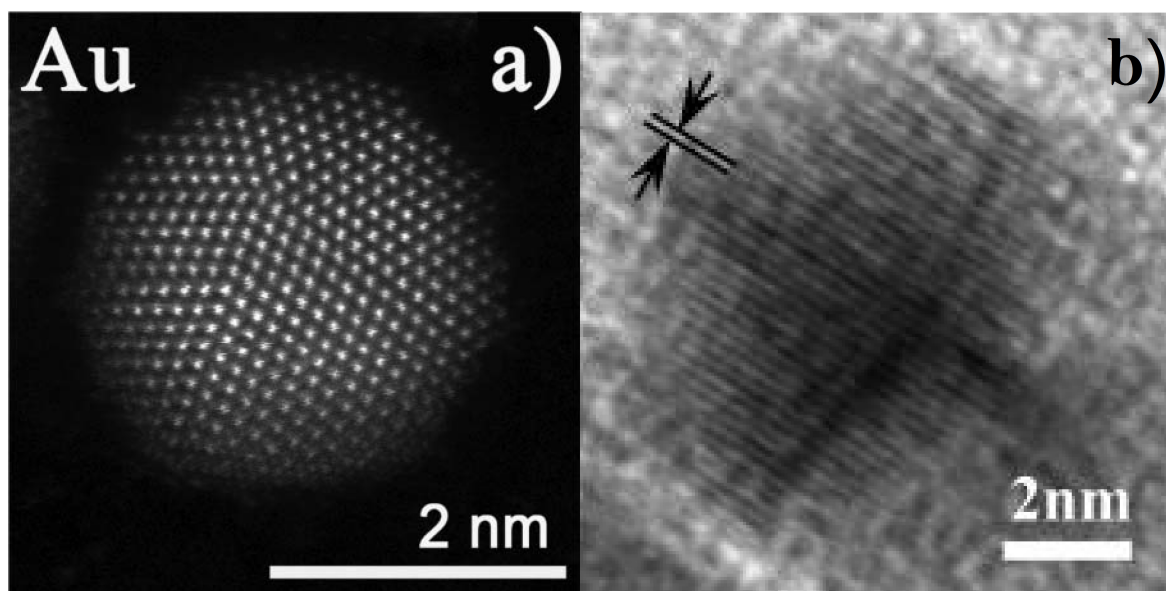


Figure 1.12 – Typical STEM (a) and HRTEM (b) examples of Au nanoparticles synthesised in the THPC method as a hydrosol (a) and water–toluene interface (b). The films of nanoparticles formed at the interface were deposited onto substrates and used directly. Images taken from ref^{53,68}

reducing agent. As expected the reaction occurred generating nanoparticles of Pt, however without the THPC present interparticle growth and aggregation could occur. Leading to large agglomerates forming as a black precipitate. It was therefore confirmed that THPC acted as both electrostatic stabilizer and generator of formaldehyde through the conversion of THPC to THPO.^{53,57,67} Hydrogen gas is also produced through the reduction of water by the reaction intermediate (Step b in Figure 1.11). The generated H₂ is then oxidised back to water in the reduction of metal ions.^{53,58}

Methods

THPC has been utilised in two main methods for the generation of nanoparticles.^{39,60} For a typical one phase reaction a metal salt in solution is added to a stirred aqueous mixture of sodium hydroxide and THPC. When using chloroauric acid the formation of an orange–brown hydrosol of gold nanoparticles of 1–2 nm diameter is generated.⁶⁷ It has been shown that using the same method and employing equimolar ratios of chloroplatinic acid and chloroauric acid yielded PtAu alloyed nanoparticles with an mean size of close to 2 nm.⁵³ Recently Li *et al.* have utilised THPC in the presence of (±)- α -Lipoic acid for the reduction of aqueous CuSO₄. THPC produced the more stable nanoparticles when compared to NaBH₄ and N₂H₄. In efforts to further increase the capping by the thiolated ligand, dihydrolipoic acid (DHLA), NaCl was later added. TEM analysis of the Cu nanoparticles showed an average diameter of around 1.6 nm.⁶³ Rao and co-workers have been utilising THPC reduction of metal ions

across the toluene–water interface.^{40,52,66,69,70} The formation of films of nanoparticles occur at the interface through a diffusion controlled process, when metal ions diffusing into the interface interact with reducing agents also in the interface.⁷⁰ In the series of reactions metal salts dissolved in toluene were carefully layered on top of aqueous NaOH, once the layers had stabilised, THPC was injected into the aqueous phase and reduction proceeded. The method has been used to synthesise; gold, silver, copper and palladium. Bi- and tri-metal nanoparticles could also be formed by varying the feed ratios of metal ions in the toluene phase of the reaction.⁵² The nanoparticles form as a thin film at the interface which can then be deposited onto a substrate,⁶⁶ or formed into sol through the addition of a suitable ligand exchange.⁴⁰ Typically when using Au(PPh₃)Cl the mean Au nanoparticle diameter after reacting for 24h at room temperature was ≈ 9 nm, with a close-packed arrangement of nanoparticles separated by an interparticle distance of 1.5 nm. Further studies with Au(PPh₃)Cl have shown that higher temperatures produce larger nanoparticles, 15 nm at 75 °C.⁶⁸ The films produced at elevated temperatures, and deposited onto glass substrates, possess relatively fewer cracks and pits than those at cooler temperatures and tend to show higher conductivities in electrical measurements. Higher concentrations of THPC produced less uniform films of nanoparticles with a broader range of diameters. Using highly concentrated precursor solutions did not effect the distribution of dimensions, merely the quantity of nanoparticles within the expected size range. Figure 1.12 shows the STEM and HRTEM of Au nanocrystals synthesised using THPC as a hydrosol and a two-phase method. Ag nanoparticle films produced using Ag₂(PPh₃)₄Cl₂ or Ag(PPh₃)Cl in place of the Au(PPh₃)Cl formed highly lustrous interface films with an average diameter of 10 nm.⁴⁰ The mono-metallic 75 °C Ag films showed diameters in the range of 60–100 nm through TEM imaging.⁵² When synthesised at room temperature the Ag films consisted of diameters in the range of 10–50 nm.⁴⁰ XPS analysis of pure Ag shows two different Ag species; one of the core Ag and one of the surface Ag bound to the ligands. Studies of silver nanoparticles formed using the method found them to be sensitive to the contact time, temperature and metal ion concentration.^{69,70} Nanoparticle films of Au–Ag, generated at 75 °C, showed an increase from ≈ 16 nm to ≈ 60 nm with increasing Ag content, when estimated from XRD peak widths. TEM of the 50:50 bi-metal AuAg and AuCu showed mean diameters of 23.5 nm for AuAg and a range 10–25 nm for AuCu.

1.4 Charge Transport Properties in Nanocrystals

The energy required for charge transport in a bulk material is equal to the work function. When looking at single particle systems, in the case of nanocrystals, there are separate energies for adding charge to a particle (EA, electron affinity) and removing charge (IP, ionisation potential). In the smaller systems there are less electrons, making the electronic behaviour very different to the bulk.¹ When compared to the bulk work function, the sum of IP and EA is almost equal, but not entirely. The difference is defined as the charging energy which is related to the capacitance (C) of the particle. Capacitance of nanocrystals is size dependent as shown in equation 1.4.

$$C(r) = 4\pi\epsilon_0\epsilon_r r \quad (1.4)$$

Where ϵ_0 is the permittivity of a vacuum and ϵ_r is the dielectric constant of the medium surrounding the particle. Using capacitance the charging energy (U) is defined by:

$$U = \frac{C(r)}{2e} \quad (1.5)$$

The charging energies defined by Equation 1.5 are not equivalent to the electronic energy levels found in nanocrystals, they are Coulombic states and manifestation of single electron tunneling.⁷¹

When describing a nanocrystal film, it can be thought of as an electrical circuit with metal particles capacitively coupled to the adjacent particles (Figure 1.13). There are two reported possible electron transport mechanisms, tunneling and hopping. Where both show voltage dependence on current, but only conduction by hopping shows any temperature dependence.⁷² Quantum tunneling is a quantum mechanical phenomenon which allows for electrons to tunnel through an insurmountable wall. The energy of an electron at room temperature is generally significantly lower than the barrier, meaning charge transfer is classically forbidden. Quantum tunneling through the barrier can take place; however, the ability to tunnel decays as the distance between particles increases.

Activated hopping, unlike tunneling, accounts for temperature and interactions by capping ligands. When nanocrystals in the film are coupled and interact the electrons may hop from

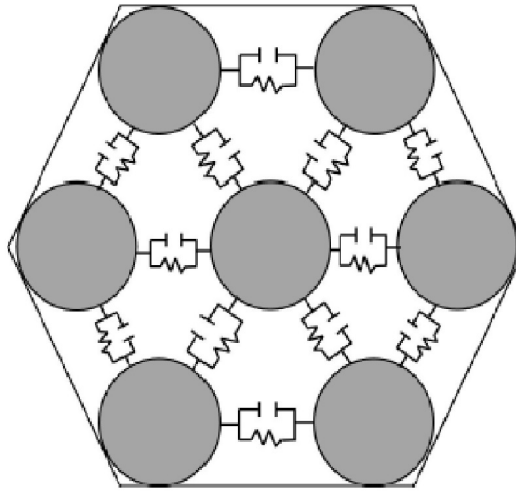


Figure 1.13 – A diagram showing an electrical equivalent circuit for an array of nanocrystals, shown in grey, and their capacitance linkers.⁷³

one particle to the next, influenced by temperature. A simple model for hopping between metal cores has been proposed.^{74,75} The conductivity (σ) in metallic nanocrystal films can be represented by Equation 1.6

$$\sigma \propto e^{-2\delta\beta} e^{-E_a/kT} \quad (1.6)$$

Where δ is the distance between nanocrystals, β is the tunneling constant between the nanocrystals in a dielectric medium and E_a the activation energy for an electron to hop between the nanocrystals. When the capping ligands are uniform, as is expected,³⁷ it may be assumed that δ and β are constant at various temperatures (T), giving:

$$\sigma = Ae^{-E_a/kT} \quad (1.7)$$

where:

$$E_a = \frac{1}{4\pi\epsilon_0\epsilon_r} \frac{e^2}{r} \quad (1.8)$$

1.4.1 Coulomb Blockade and Single Electron Tunnelling

Charge transport studies on a single conducting nanocrystal surrounded by an insulating ligand shell often exhibit distinct single-electron transport effects.⁷⁸ These effects are particularly prominent when the nanocrystal is small and the energy required for an electron to tunnel onto the particle is far greater than the thermal energy available (k_bT), described by the orthodox theory.^{77,79} The electron can tunnel onto the particle when the electrostatic conditions are favourable; the total energy after the addition of an electron onto the particle is required to

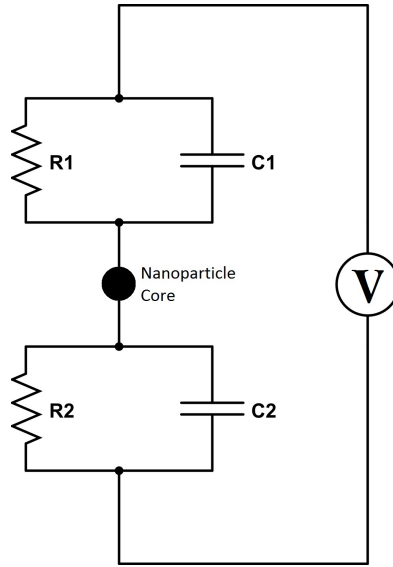


Figure 1.14 – An equivalent circuit for the double barrier tunnelling junction. Showing the the junction each side of the nanoparticle island. Each junction can be modelled as a resistor and capacitor in parallel.^{4,71,76,77}

be smaller than the energy of the initial state. The change in total energy of an electron for tunnelling can be modelled by the circuit in figure 1.14 and by the following equations.^{76,77} The electron transfer from particle to particle(or electrode) is governed by the Coulomb charging energy (E_C).

To tunnel through the first junction:

$$\Delta E_1^\pm(n) = \frac{e^2}{2C_\Sigma} \pm \frac{e}{C_\Sigma}(ne + Q_0 \mp C_2V) \quad (1.9)$$

To tunnel through the second junction:

$$\Delta E_2^\pm(n) = \frac{e^2}{2C_\Sigma} \pm \frac{e}{C_\Sigma}(ne + Q_0 \pm C_1V) \quad (1.10)$$

Where n is the number of electrons on the particle, V is applied voltage, $C_\Sigma = C_1 + C_2$ is the total capacitance of the tunnelling and Q_0 is the fractional residual charge surrounding the particle. At values larger than zero, the tunnelling is suppressed due to the higher final energy than the initial states, known as the Coulomb blockade.⁸⁰ Electrons can only tunnel one at a time when the value for the junction becomes negative.

Observation of the Coulomb blockade is temperature dependent as the charging energy needs to be higher than k_bT .

$$E_c > k_bT < \frac{\hbar}{RC_\Sigma} \quad (1.11)$$

Where R is the resistance of the tunnelling junction. Coulomb blockade can be discerned by non-linear current-voltage curves produced by transport measurements. A typical set of curves exhibiting single electron Coulomb blockade as well as staircase behaviour is shown in figure 1.15. The width of the current exclusion zone around nil voltage, called the blockade, depends on the charging energy, dimensionality of the array and the number of elements in the system.⁷³ The smaller periodic staircase on either side of zero voltage is referred to as the Coulomb staircase. It represents the sequential charging of the particle with a single charge carrier as the voltage is scanned across.⁸¹ It can be thought of as an electron trapped at some point in the system, before tunneling. The Coulomb blockade and staircase have both been observed in a number of experiments.^{71,77,81-87}

For a single island between source and drain electrodes the resistance and capacitance are related to the distances of the electrodes and ligand shell nature. Leading to a ratio R_1/R_2 , where R_2 is believed to be constant due to the ligand molecules and R_1 can be changed by the application of a bias voltage. The shape of any resulting Coulomb staircase is strongly dependent on the ratio as shown in Figure 1.15.^{77,86,87} E_c can be determined directly by scanning tunnelling spectroscopy(STS) measurements.^{3,76,86,87}

For ordered arrays, or films, of NCs there are multiple islands for charges to hop through making the phenomenon more complex to model.⁸² The value for E_c can be estimated when the NC is thought of as a sphere in a uniform dielectric medium.⁸⁸ Providing an estimate in the form of:

$$E_c = \frac{e^2}{4\pi\epsilon_0\epsilon_r D} = \frac{e^2}{2C} \quad (1.12)$$

where, C is the capacitance of the particle, D is the particle diameter and ϵ_r is the effective dielectric constant for the NC film, taking into account both the NC and its surrounding medium.^{81,85,89} Equation 1.12 shows that the E_c is dependent on the size, nature and surrounding ligands for NCs.⁹⁰ As an example, a particle with a typical D of 10 nm employing an organic insulating ligand shell, $\epsilon_r \approx 3.5$ has a charging energy, E_c , of ≈ 40 meV.⁸¹ As the

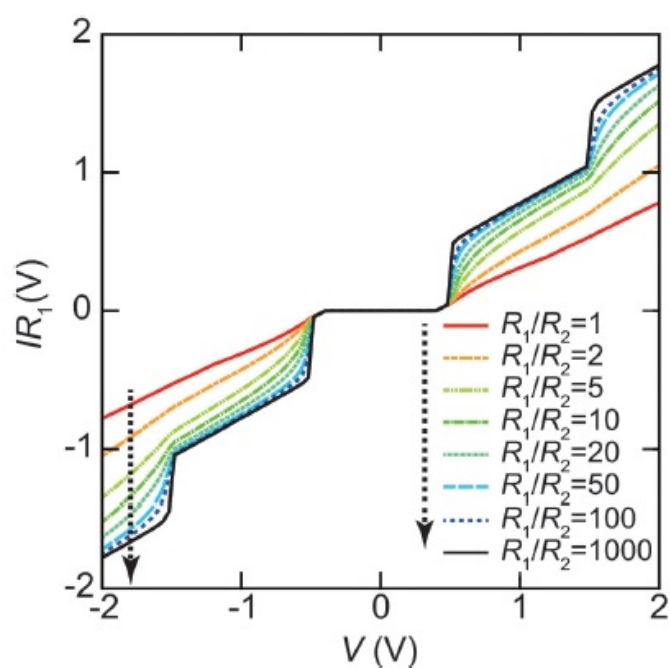


Figure 1.15 – Set-point current dependence of the whole shape of Coulomb staircases. These curves are simulated by the orthodox theory using $R_1/R_2 = 1, 2, 5, 10, 20, 50, 100$ and 1000 , respectively (indicated by the dashed arrow in order). The circuit parameters are $R_1 = 0.1\text{--}100\text{ G}\Omega$, $R_2 = 0.1\text{ G}\Omega$, $C_1 = 0.16\text{ aF}$, $C_2 = 0.20\text{ aF}$, $Q_0 = 0e$ and $T = 4.2\text{ K}$. The vertical axis is normalized by multiplying R_1 to compare the whole shape of the Coulomb staircase. A higher R_1/R_2 value gives a sharper Coulomb staircase; in contrast, the shapes of the curves are not dependent on R_1/R_2 values under $R_1/R_2 > 50$. Ref.⁷⁶ with permission from the Royal Society of Chemistry.

thermal energy at room temperature is approximately, ~ 25 meV, Coulomb charging energy will inhibit the conduction of charge, unless a suitable bias is applied to provide the energy required to overcome the barrier. There exists a voltage threshold V_{th} below which the charge transport is suppressed as Coulomb blockade dominates. E_c and V_{th} can be related by the following equation

$$V_{th} = \alpha N E_c \quad (1.13)$$

where $0 < \alpha < 0.5$ is a value determined by the NC packing and N is the number of islands along the conduction pathway.⁹¹ The dependency of V_{th} on the number of islands in the array means that there will be a decreasing V_{th} with an increase in array size.⁸³ The visualisation of a Coulomb staircase in NC arrays is progressively more difficult as the physical dimensions of the arrays increases.⁷³ Values calculated for V_{th} , in equation 1.13, can be somewhat unreliable as it has also been shown that V_{th} can change with the scale of the I–V measurement.⁹¹

1.4.2 Charge Transport properties in Arrays of Nanocrystals

There are several theories of the charge transport mechanisms within nanocrystal systems. Generally the medium consists of close packed metal or semiconductor grains held within an insulating matrix.⁴ We note that as the dimensions of a solid is reduced, the degeneracy of energy states that characterize the bulk band structure is lifted and the levels are separated by Kubo gap. Such discreteness is particularly pronounced at band edges and could lead to nanocrystals possessing electronic character distinct from the bulk.¹⁷ The electrical properties of granular materials, or in this case nanocrystals, have been extensively studied. The framework was built by Mott,⁹² Efros and Shklovskii⁹³ and Neugebauer and Webb⁷⁴ as well as others. The following section shall attempt to provide an overview of the different mechanisms and how they have been recognised in the course of experiments.

Conduction via Nearest Neighbour Hopping

In nearest-neighbour hopping (NNH), conduction occurs mainly through the tunnelling of charge carriers between neighbouring sites. NCs isolated from each other, show a decrease in conductance with temperature,^{37,94} fitting the model of activated hopping proposed by Neugebauer and Webb.⁷⁴

$$\sigma \propto e^{-2\delta\beta} e^{-E_a/k_b T} \quad (1.14)$$

Where δ is the separation between the NCs, β is the tunnelling constant between NCs in a dielectric constant, E_a is the activation energy for charge hopping. In a NC film with a well

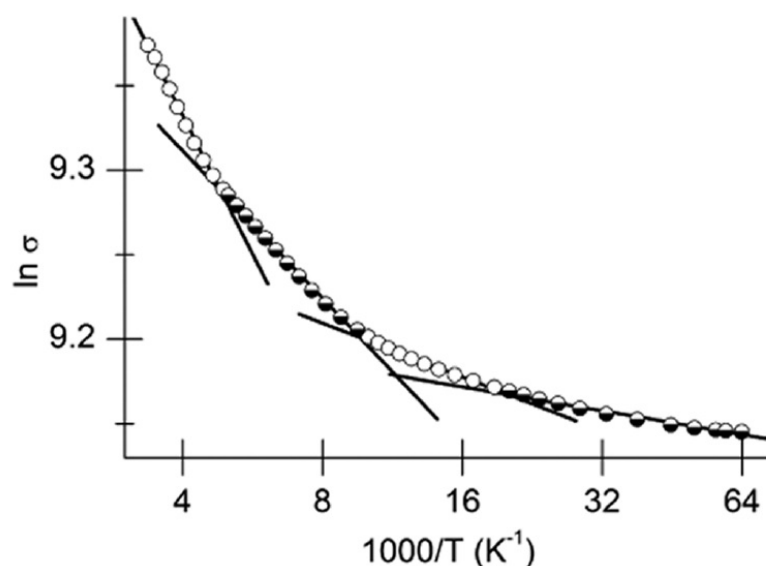


Figure 1.16 – Plot of $\ln \sigma$ vs $1/T$. The straight lines show four different linear regimes for Activation energy with temperature change. Reprinted with permission from J. Am. Chem. Soc., 2012, 134 (29), 11888–11891. Copyright (2012) American Chemical Society.

defined ligand, δ and β may be assumed to be constant, when thermal expansion/contraction is ignored.^{78,95} Thus,

$$\sigma = Ae^{-E_a/k_bT} \quad (1.15)$$

Information of the size of NCs and the effects of the surrounding ligands are contained in the pre-exponential A term. Additionally, size and ligand effects can also influence activation energy.⁹⁴ Linear plots of $\ln \sigma$ vs $1/T$ can be used to obtain the activation energy from experimental observations. The activation profile can undergo changes with temperature(see Figure 1.16).^{37,94}

When E_a is comparable to k_bT , conductivity is nearly independent of temperature, the CT mechanism changes to match the description of the variable range hopping model. Figure 1.17 shows such a collapse of E_a in the case of nanocrystalline Si.⁹⁶

Conduction via Variable Range Hopping

Nanocrystal assemblies within the non-metallic regime, can deviate from the Arrhenius behaviour.⁹⁶ The conductivity of these systems can be modelled as:

$$\sigma \approx \exp \left[-\frac{T_0^v}{T} \right] \quad (1.16)$$

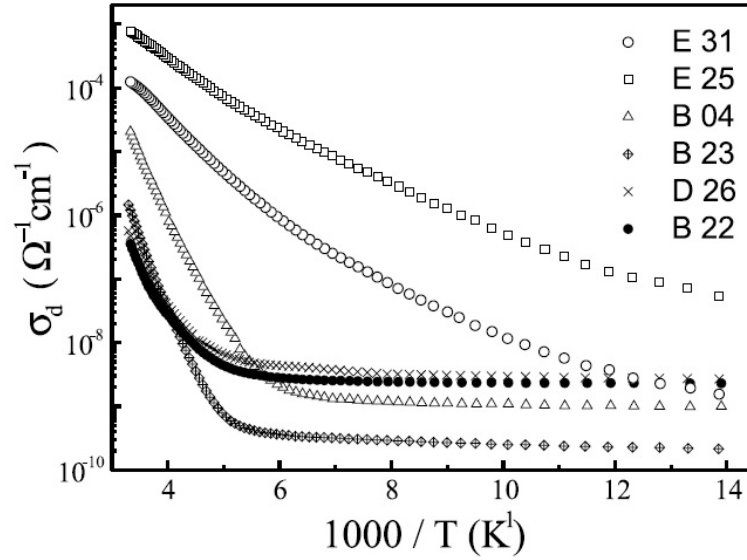


Figure 1.17 – Conductivity in nanocrystalline silicon films of a range of thickness's (E31 = 1200 nm – B22 = 170 nm). Conductivity appears to be becoming independent of temperature at low temperatures. Reprinted from Journal of Non-Crystalline Solids, 299–302, Ram, Sanjay K. *et al.*, Investigations of the electron transport behavior in microcrystalline Si films, 411–415, Copyright (2002), with permission from Elsevier.

where T_0 is a temperature constant and ν is a characteristic exponent which distinguishes between different mechanisms. If ν is ≈ 1 , then NNH Arrhenius behaviour is evident. Variable-range hopping models are used to explain the fractional value of ν . These models assume that charges can acquire the thermal energy required to hop to a new site. Hopping to the next neighbour site is not always energetically favoured since there is a larger probability of finding a more energetically favourable site at a greater hopping distance. The balancing of these two factors, energy difference and distance, are what lead to the fractional value.^{95,97} Transport with $\nu = 1/2$ ⁹³ and $\nu = 1/3$ ⁹⁸ signify Efros-Shklovskii variable range hopping (ES-VRH) and Mott variable range hopping (Mott-VRH) respectively.⁸⁵

Mott-VRH assumes a constant density of states around the Fermi level, where the hopping conduction occurs between localised states. Allowing for the characteristic temperature constant, T_0 , for Mott-VRH to be obtained.⁹⁹

$$T_0 \equiv T_M = \left(\frac{3}{k_b N(E_f) a^2} \right) \quad (1.17)$$

Where $N(E_f)$ is the density of states near the Fermi level and a is the localisation length. However, at low temperatures the density of states is not constant, it vanishes linearly with

energy.⁹⁹ Resulting in a Coulomb gap that must be overcome by hopping charges. The ES-VRH takes the Coulomb gap into account allowing for the energy increase associated with the hopping to overcome the Coulomb gap leading to.⁹⁹

$$T_0 \equiv T_E = \left(\frac{2.8e^2}{4\pi\epsilon\epsilon_0 k_b a} \right) \quad (1.18)$$

Where e is the charge of an electron, ϵ is the dielectric constant of the material and ϵ_0 is the permittivity of vacuum. Both forms of T_0 are dependent on the localisation length with the ES-VRH also showing a dependence on the dielectric constant of the material. When there is high disorder in the sample the Coulomb gap dominates conductance and ES-VRH has been shown to be the preferred hopping method. At samples with low disorder Mott-VRH seems to dominate.⁹³ It has also been seen that a transition between Mott and ES-VRH can occur when there is a intermediate disorder in the sample.¹⁰⁰

It is possible to distinguish between the two VRH mechanisms through curve fitting analysis, plotting $\ln(\sigma)$ vs $T^{1/3}$ for Mott-VRH or $T^{1/2}$ for ES-VRH. It has however been reported that data can seemingly fit both regimes.⁹⁹ To overcome the ambiguity, the determinant v can be determined from the following

$$W = -\frac{\delta \ln \rho(T)}{\delta \ln T} = p \times \left(\frac{T_0}{T} \right)^p \quad (1.19)$$

Where W is the reduced activation energy, hopping energy. Values for p can now be defined by the slope of $\ln W$ vs $\ln T$ since

$$\ln W = A - p \ln T \quad (1.20)$$

1.4.3 Nanocrystal Ligands and Their Effects on Charge Transport

As discussed previously, the charge transport properties can be modified through ligand exchange. Altering the ligands surrounding NCs impacts on interparticle distance (D), radius (r) and the effective dielectric constant (ϵ_r). Ligand exchange reactions allow for surfactants optimised for synthesis to be replaced by those more suited to the final application.¹⁰¹ The choice of surface ligands control the barriers to electrical transport in NC arrays.^{102,103} Many investigations have been undertaken using organic and inorganic ligands to tune the CT properties. Talapin compared the ligand exchange process to the substitution reaction in coordination

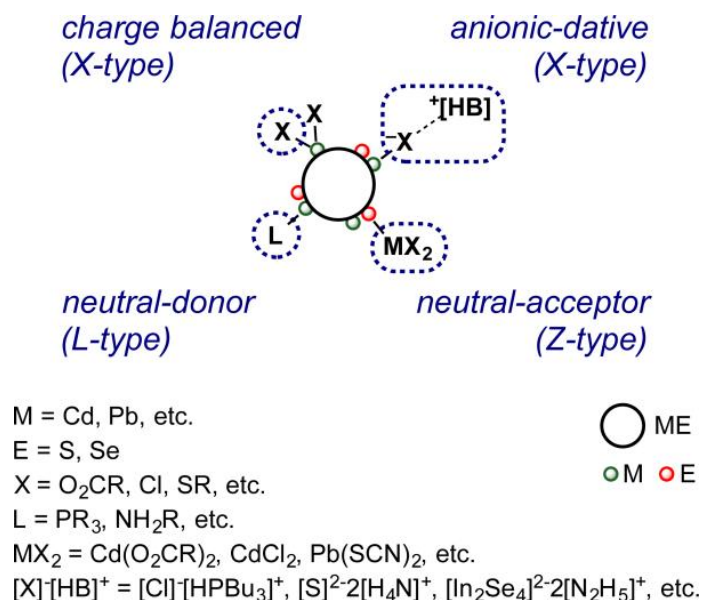


Figure 1.18 – Ligand binding according to the covalent bond classification. ME represents a NC of binary *II – VI*, *IV – VI*, and *III – V* semiconductors (such as CdS). Reprinted with permission from J. Am. Chem. Soc., 2013, 135 (49), 18536–18548. Copyright (2013) American Chemical Society.

chemistry.¹⁰¹ The types of ligands used have been categorised into 3 groups; donor, L, anion, X, and acceptor, Z (Figure 1.18). L type ligands are neutral donor species such as amines and phosphines. X type ligands attach to the NC surface in an anionic manner to terminate the lattice, species such as thiols, carboxylic acids, metal free ions¹⁰⁴ and halogens. Finally Z type ligands are neutral acceptor species such as CdCl₂ or AlCl₃.^{101,105–107} Total exchange of surface ligands would be dependent on concentrations of the incoming and outgoing ligands, as well as the difference in their affinities for the NC surface. For example, dodecanethiol will displace phosphine oxide ligands from Au NCs, however the reverse is unlikely due to the gold–sulfur affinity. The concept can be explained through the hard–soft acid–base principle, where strong electrostatic bonds are formed by hard Lewis acid–base pairs and strong covalent bonds are formed by soft Lewis acid–base pairs.^{108,109} Mixtures of hard Lewis acids and soft Lewis base pairs have a poor affinity and do not bind strongly.^{101,105} By using ligands which have multiple binding sites such as dithiols and carboxylates the affinity to the NC surface will increase. The steric effects caused by bulky tert–butyl ligands when compared to saturated straight chain alkanes will also effect the binding of ligands to the surface, it has been shown that bulky ligands have lower surface coverage when compared to easily packed ligands.¹⁰¹

There are two general methods for ligand exchange, in the first method ligands are exchanged in the liquid state. Performed in either a one phase system, or a two phase system where the incoming ligand promotes stability in a new medium.^{104,107} Liquid phase exchange facilitates creation of devices where the inter NC distances is related to the new ligand.

The second method involves the ligand exchange in solid-state. By soaking NC arrays in solutions containing the incoming ligand, the exchange can be allowed to happen.^{37,66,107,110} Allowing for a broad range of exchanges however, can also lead to cracking of the layer due to volume contraction caused by replacing large ligands with much smaller ones. Luther *et al.*, used repeated deposition and ligand exchange to attain a smooth uncracked layers of a desired thickness.¹¹¹

Organic Ligands in Nanocrystals

The use of organic ligands for NC arrays has been extensively studied.^{9,37,77,82,112,113} Typically, long chain hydrocarbons (C₄ – C₁₂) do not allow an efficient charge transfer and transfer of capping ligands with shorter molecules has been practised¹¹⁴ Investigations have shown that shorter ligands lead to increased conductivities in arrays of alkanethiol-capped Au NCs. Stansfield *et al.* used substituted arylthiol-capped Au NC arrays to demonstrate the substituent effects on the resulting conductivity. The arrays produced in this study showed the ability to be tuned between 100 and 75000 S m⁻¹ by simply varying the substituent in the para position.³⁷

The *N*-2,4,6-trimethylphenyl-*N*-methyldithiocarbamate molecule was incorporated onto PbS NCs. The molecule was selected as it is small and conjugated, requiring no further modification in the solid state. The carbodithiolate head is thought to bind strongly to the surface, through a pair of strong metal-sulfur bonds. These NC layers were used in solar cell devices providing, at the time, some of the highest efficiency devices. The ligand was also shown to lower the air sensitivity of the material.¹¹⁴

Strikingly, Nakanishi and co-workers were able to produce negative photocurrents, a decrease in current on illumination, in Au and Ag NCs through ligand modification.¹¹⁵ Au and Ag NCs of 5.6 ± 0.8 nm diameter were prepared and stabilised with a selection of alkane thiols. The resulting suspension was drop-cast onto glass and evaporated under vacuum. Film thickness of 120 – 300 nm were reported. The drop-cast films showed a red shift in the surface plasmon

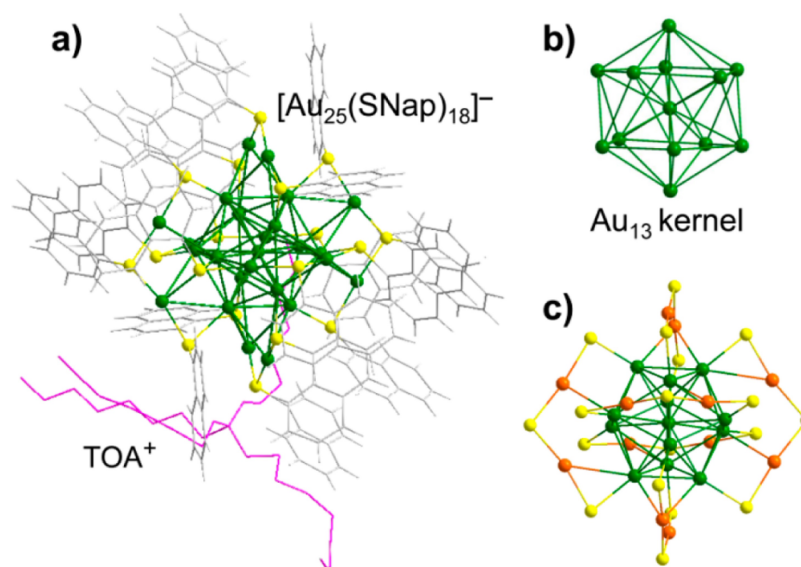


Figure 1.19 – (a) Total structure of the $[\text{Au}_{25}(\text{SNap})_{18}]^{-}[\text{TOA}]^{+}$ nanocluster ($\text{Au}_{25}\text{S}_{18}$ is shown in ball-and-stick mode, thiolate ligands and TOA^{+} in wire-and-stick mode). (b) Icosahedral Au_{13} kernel. (c) Six dimeric $\text{Au}_2(\text{SR})_3$ staple motifs. Gold, green or orange; sulfur, yellow; carbon, gray; hydrogen, white; TOA, magenta. Reprinted with permission from ACS Nano, 2016, 10 (8), 7998–8005. Copyright (2016) American Chemical Society.

resonance band when compared to the suspension, the shift was attributed to aggregation of the NCs.¹¹⁵ Contacts were sputter coated onto the films and then exposed to white LED light of intensity $I_{\text{white}} = 60 \mu \text{ W cm}^{-1}$. Films comprised of neutral thiols produced a positive current density on irradiation of light. When the films contained charged (either positive or negative) thiols a negative current density was obtained.¹¹⁶ The negative current density was believed to be due to the trapping of free charge carriers. It is suggested that traps were caused by two things; the NC cores and the organic ligands. The uncharged organic ligands contain no traps and charges tunnel through the insulating ligands. In charged ligands traps exist adding to those on the NC core. In the dark these traps lay above the Fermi energy and therefore only act as part of the tunnelling barrier. Under irradiation conditions the charge carriers are promoted to higher energies where the traps now have an effect, the density of traps in the system increases lowering the number of free carriers leading to a current decrease.¹¹⁵

Nanoclusters comprised of 25 gold atoms can be produced with atomic precision using wet chemical techniques.¹¹⁷ The properties of these nanoclusters can be easily influenced through the use of protecting ligands, in the same way as nanocrystals (Figure 1.19). It has been reported that electron-withdrawing ligands favour reduction over oxidation. $[\text{Au}_{25}(\text{SNap})_{18}]^{-}[\text{TOA}]^{+}$

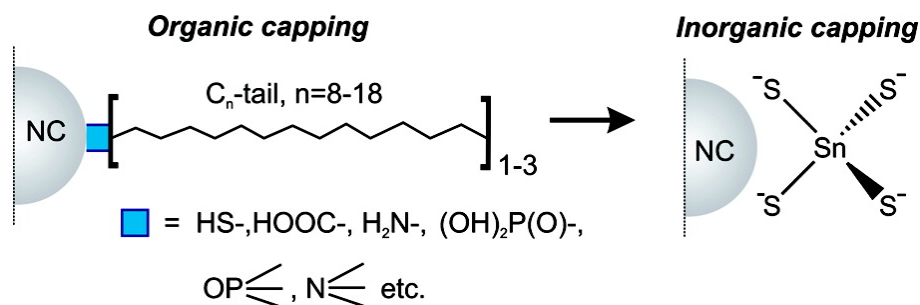


Figure 1.20 – Scheme showing the ligand exchange process used for preparation of all-inorganic nanocrystals. Reprinted with permission from J. Am. Chem. Soc., 2010, 132 (29), 10085–10092. Copyright (2010) American Chemical Society.

(from herein shown as Au₂₅(S₄Sn)) clusters have been prepared and their electronic properties investigated through UV/Vis spectroscopy and DFT calculations.¹¹⁷ For comparison clusters using Au₂₅(S₄Sn), Au₂₅(SPh) and Au₂₅(SCH₂CH₂Ph) were prepared as solutions in dichloromethane and optical absorption spectra collected. Clusters capped with Au₂₅(S₄Sn), Au₂₅(SPh) were red-shifted to increasing values compared to the Au₂₅(SCH₂CH₂Ph). To understand the red-shifts density functional theory calculations were performed using Au₂₅(SCH₃) and Au₂₅(SPh) as models. The exchange of (SCH₃) with (SPh) caused a slight decrease in the HOMO–LUMO gap, ≈ 0.03 eV, inducing the observed red-shift.¹¹⁷

Inorganic Ligands in Nanocrystals

More recent research has focused on a family of smaller inorganic ligands that promote charge transport and aid particle stability in polar solvents. Unlike organic ligands, these ionic species are widely believed to coordinate strongly to the surface of the NC and provide electrostatic stabilisation in polar solvents.^{102,103,118–120} Pronounced changes to charge transport have been reported following the functionalization of the nanocrystals surface with inorganics.

Here, we review detailed studies featuring the following complexes: chalcogenidometallates (also known as metal chalcogenide complexes, MCC) (SnS₄²⁻, Sn₂S₆⁴⁻, AsS₃³⁻, In₂Se₄²⁻),^{10,104,120–122} halometallates (PbCl₃⁻, PbI₃⁻, FeCl₃⁻, InCl₄⁻),^{123,124} chalcogenide (S²⁻)^{118,125} halides and pseudohalide (Br⁻, I⁻, SCN⁻, N₃⁻)^{8,124,126–131} ions.

Pioneering work building on Mitzi's initial reports, which brought MCCs to light,¹³² has shown that the MCCs dissolved in anhydrous hydrazine could displace ligands such as: alkyl phosphonic acids (TOPO etc), oleic acid and alkyl thiols¹²¹ commonly used to obtain monodisperse NCs (Figure 1.20). Following the ligand exchange, the NCs could move from the non-polar medium into polar solvents such as DMSO, hydrazine.^{104,118,120,121}

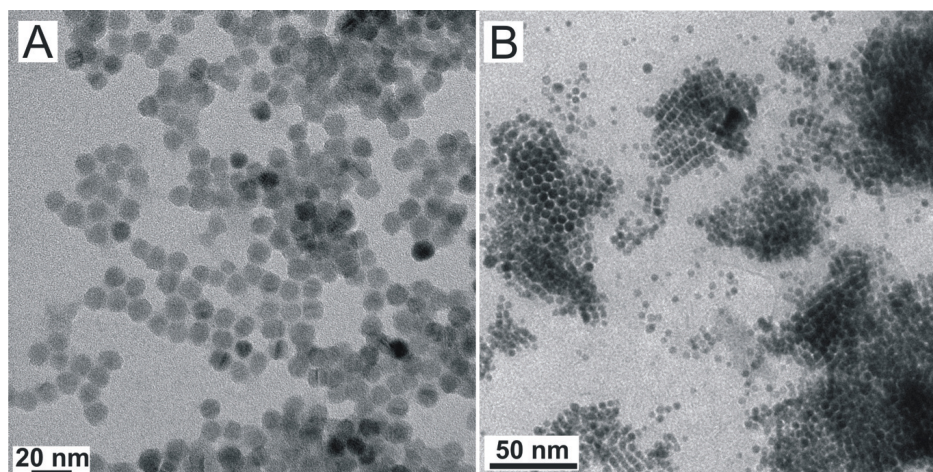
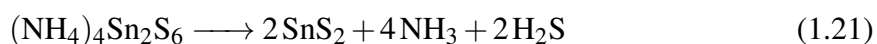


Figure 1.21 – TEM images of 9.1 nm CdSe, A, and 5 nm Au, B, NCs capped with $\text{Sn}_2\text{S}_6^{4-}$ ligands. Adapted with permission from J. Am. Chem. Soc., 2010, 132 (29), 10085–10092. Copyright (2010) American Chemical Society.

Such a ligand replacement was shown to largely preserve the original optical absorption characteristics of CdSe and Au NCs.^{120,121} A striking 10 orders of magnitude improvement in room temperature conductivity following the displacement of the dodecanethiol ligand by $\text{Sn}_2\text{S}_6^{4-}$ has been observed. The conductivity of, 5 nm, $\text{Sn}_2\text{S}_6^{4-}$ capped Au increased to *c.a.* 1000 S cm^{-1} from $\sim 10^{-9} \text{ S cm}^{-1}$.^{120,121} Reliable SnS_2 shells were obtained on CdSe nanocrystals through the use of the thermally decomposable $(\text{NH}_4)_4\text{Sn}_2\text{S}_6$ molecule (Figure 1.21). Whilst in solution the original organic-capped and $(\text{NH}_4)_4\text{Sn}_2\text{S}_6$ -capped NCs showed identical absorption spectra. When developed in to solid-state devices the close packed films of MCC-capped CdSe were red shifted, it was possible to increase the shift by thermal decomposition at 200°C to leave a very thin shell of SnS_2 .^{10,121}



Field-effect transistors (FET) manufactured with 4.5 nm CdSe/ SnS_2 NCs yielded electron mobilities of $1.4 \times 10^{-5} \text{ cm}^2 \text{ V}^{-1} \text{ s}^{-1}$.¹²¹ Similar studies on $\text{In}_2\text{Se}_4^{2-}$ -capped CdSe (3.9 nm) and CdSe/CdS (3.6 nm) resulted in values of $10\text{--}16 \text{ cm}^2 \text{ V}^{-1} \text{ s}^{-1}$ and $3.7 \text{ cm}^2 \text{ V}^{-1} \text{ s}^{-1}$.

Jang *et al.* performed temperature dependent Hall and Field-effect mobility studies on annealed arrays of 5.3 nm InAs NCs, capped with either $\text{In}_2\text{Se}_4^{2-}$ or Cu_7S_4^- ligands.¹⁰ They discovered that $\text{In}_2\text{Se}_4^{2-}$ capped InAs NCs showed a room temperature (RT) Hall mobility of $\sim 1.3 \text{ cm}^2 \text{ V}^{-1} \text{ s}^{-1}$. However the Cu_7S_4^- capped InAs NCs resulted in a much higher Hall mobility of $16.8 \text{ cm}^2 \text{ V}^{-1} \text{ s}^{-1}$. $\text{In}_2\text{Se}_4^{2-}$ capped InAs NCs showed a similar Field-effect

mobility, however the Cu_7S_4^- capped InAs NCs showed a lower Field-effect mobility ($7.5 \text{ cm}^2 \text{ V}^{-1} \text{ s}^{-1}$). The difference in mobilities between $\text{In}_2\text{Se}_4^{2-}$ and Cu_7S_4^- capped InAs was believed to be due to the more efficient tunnelling of electrons through the ligands. The comparison between the Hall and Field-effect results showed that in the low doping system (Cu_7S_4^-), the applied gate voltage played a more evident role in the charge transport, than in higher doped systems, by providing a charge accumulation.¹⁰ Building on these results, the Talapin group have proposed the use of MCCs to form composition-matched "solders" for the joining of NCs.¹¹⁹ They wished to provide alignment between the Fermi levels at the NC ligand boundary to allow efficient CT through the material. The ideal "solder" should be produced of a precursor that, when annealed, would form a semiconducting material which matched the bonded parts. In one example $[\text{Cd}_2\text{Se}_3]^{2-}$ ions were used to cap 4.7 nm CdSe NCs. Complete replacement of the original *n*-octadecylphosphonic acid ligands was confirmed by infrared (IR) spectroscopy. The $[\text{Cd}_2\text{Se}_3]^{2-}$ -capped CdSe NC suspension was spin-coated onto doped Si and used in FET mobility measurements. Post annealing at 250°C the electron mobility was measured at $210 \text{ cm}^2 \text{ V}^{-1} \text{ s}^{-1}$. At the time these values exceeded any other reported for solution-processed inorganic semiconductors.¹¹⁹ Further annealing at 300°C produced devices measuring FET mobilities of $> 300 \text{ cm}^2 \text{ V}^{-1} \text{ s}^{-1}$, a mobility which compares well to the best bulk solution-processed materials.¹⁰³ The data was believed to confirm the need for designing "solders" to join NCs which match the energy levels within the materials.

MCC complexes do however have their associated problems. The preparation of the compounds requires inert atmospheres, due to their unstable nature.^{10,120} It was also identified that the ionic composition differed, dependent on the solvent used. For reasons such as these researchers began looking into simpler, smaller and more stable molecules for ligands.^{109,118}

The thiocyanate (SCN^-) ion has been demonstrated as an air stable, environmentally benign, short ligand.^{129,130,133,134} SCN^- is suited as it can bind to the metal sites on the surface of the NC and electrostatically stabilise a variety of metal and semiconductor NC materials in polar solvents, such as: PbS, PbSe, CdS, CdSe and CdTe. The ligand was able to reduce the interparticle distance and increase the coupling between particles in films prepared post ligand exchange.¹³⁰ Devices produced with SCN^- -capped (5–8 nm) Au NCs were recorded to have conductivities of $2 \pm 0.7 \times 10^3 \text{ S cm}^{-1}$, an improvement by a factor of almost

10^{12} on the as prepared Au NCs.¹³⁰ NC spheres (6.3 nm) and cubes (11 nm) of PbS were produced and ligand exchanged with the (SCN^-) ion. FET devices employing each of the PbS morphologies and annealed at 120°C were generated. The cubes showed the higher current of the two, recording electron mobilities of $0.1 \pm 0.04 \text{ cm}^2 \text{ V}^{-1} \text{ s}^{-1}$, compared to the spheres electron mobility of $0.02 \pm 0.01 \text{ cm}^2 \text{ V}^{-1} \text{ s}^{-1}$. The cube morphology was also annealed at higher temperatures, 150°C , producing a device with a much higher electron mobility of $0.33 \pm 0.18 \text{ cm}^2 \text{ V}^{-1} \text{ s}^{-1}$.¹²⁹ Reports using SCN^- -capped CdSe NCs have provided a range of electron mobilities ($1.5 - 21.9 \text{ cm}^2 \text{ V}^{-1} \text{ s}^{-1}$) dependent on the conditions and materials used as the source/drain contacts in FET devices.^{130,133,134}

Arrays of SCN^- -capped PbSe have been investigated with the addition of PbCl_2 , in an atomic layer deposition process. The addition is believed to fill the vacant Pb sites producing a more stable NC.^{128,135} Conductivities of 20 S cm^{-1} and electron mobilities of up to $7 \text{ cm}^2 \text{ V}^{-1} \text{ s}^{-1}$ were measured in arrays of 5.9 nm NCs using Au contacts.¹²⁸ The treatment with PbCl_2 was shown to reduce the hole density whilst increasing the electron density in the NC arrays.¹²⁸ The technique was investigated at different temperatures and time scales. A 6 hour treatment at 65°C produced arrays with electron mobilities of $1.4 \times 10^{-1} \text{ cm}^2 \text{ V}^{-1} \text{ s}^{-1}$, and 12 hours yielded an electron mobility of $2.4 \text{ cm}^2 \text{ V}^{-1} \text{ s}^{-1}$. An alternative method using 95°C for just 10 minutes produced an array with an electron mobility of $\approx 4.7 \text{ cm}^2 \text{ V}^{-1} \text{ s}^{-1}$.¹³⁵

Non-chalcogenide, metal halide and halide ions have been employed as inorganic ligands for NC colloids.^{8,123,124,126} Halides are simple, short, readily available and offer a reduced toxicity when compared to other inorganic ligands being used. It has been shown that treatment with halide or halide salts leads to a reduction in surface trap sites and a reduced inter NC distance in array devices.¹²⁶ Br^- -capped PbS NCs in a room temperature (RT) process have achieved electron mobilities of $4 \times 10^{-2} \text{ cm}^2 \text{ V}^{-1} \text{ s}^{-1}$, a result comparable to some MCC type ligands after annealing at 200°C .⁸ Reports using I^- -capped CdSe NCs show an electron mobility of $12.8 \text{ cm}^2 \text{ V}^{-1} \text{ s}^{-1}$ after annealing at 200°C , which could be improved to $\approx 30.8 \text{ cm}^2 \text{ V}^{-1} \text{ s}^{-1}$ at an annealing temperature of 300°C .¹²⁴ The azide ligand, N_3^- , has also been demonstrated as a suitable ligand for capping InAs NC colloids.¹²⁴ FET devices produced using N_3^- -capped InAs annealed at 250°C had electron mobilities of $0.16 \text{ cm}^2 \text{ V}^{-1} \text{ s}^{-1}$, higher temperature annealing did show a slight improvement, but not to the same scale as the I^- -capped CdSe.¹²⁴

Ligand control is offering one of the more versatile routes in producing novel, tuned materials. Careful manipulation can yield changes of many orders of magnitude for electron mobilities and conductivities. Resulting in materials which can, one day, be built into specific devices and function as required. The newer, smaller inorganic ligands are producing arrays with much closer spacing and are thought to improve the mobility of electrons through the materials, as evidenced above. The functionalisation of NC is promising for applications in photovoltaics, FETs, molecular electronics, light-emitting diodes and many other wide ranging applications. We still require full investigations of the limits of sol and solid-state ligand exchanges. Do exchanges with smaller molecules in the solid state produce cracking and breaking up of arrays? Is a solid state exchange as efficient a method for production methods of the future?

1.5 Techniques for Characterisation of Nanocrystals

1.5.1 Electron Microscopy and Spectroscopy

Microscopy - the ability to form viewable images of objects far smaller than the eye can see - has long been used in research and has proven invaluable. There are however resolution limits to optical microscopy which render it unsuitable for modern research fields. Electron microscopy techniques; scanning electron microscopy (SEM) and transmission electron microscopy (TEM), greatly surpass these limits allowing a user to observe objects down to a few nanometres. Of the two techniques TEM works most like a traditional optical microscope. Whereby, electrons pass through the object to be imaged and form an image on a fluorescent plate or, more common in recent years, a charge-coupled device (CCD) allowing instant digital images to be produced. Scanning electron microscopy relies on those electrons scattered back up from the sample surface when forming an image. The technique can enable more three dimensional observation of the sample, as the enhanced depth of field allows for a thicker portion of the sample to be in focus. It is, however, dependent on the depth penetration of electrons and the subsequent detection of those scattered electrons. To prevent electron collisions with gas molecules and avoid arcing of the cathode in the accelerator experiments are performed at high vacuum.

Scanning Electron Microscopy, SEM

The scattered electrons collected for SEM imaging are released from the sample as a result of the ionising beam, these are known as secondary electrons. The data collected is then translated into pixel brightness to obtain the image. An example of this can be seen in figure

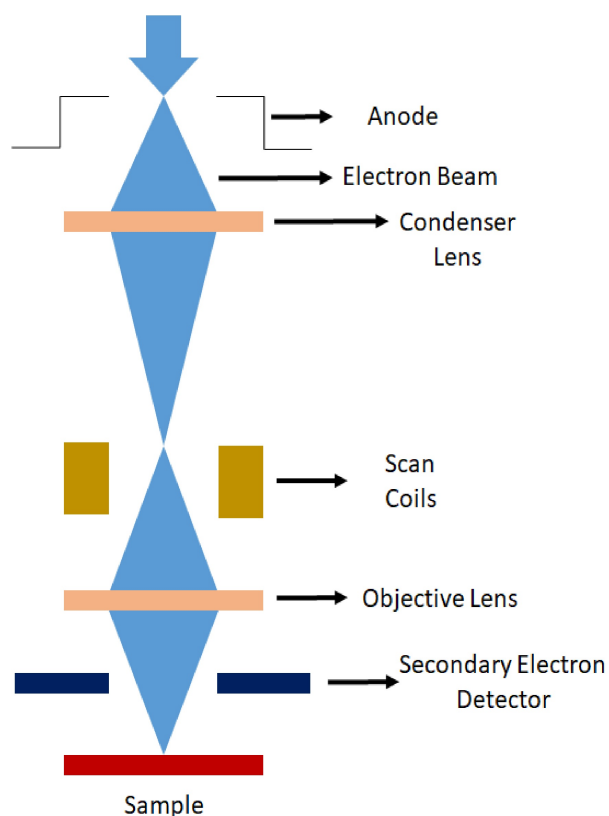


Figure 1.22 – Simplified schematic diagram of the Scanning Electron Microscope.

1.23. The electron beam is generated by thermionic emission from a tungsten filament, heated through the application of voltage. The emitted electron beam is accelerated through an anode plate, then focused by a lens through an aperture to remove stray electrons from the sides of the beams (figure 1.22). An objecting lens focuses the beam onto the sample where it can be scanned over the surface. The surface scanning is achieved by creating a magnetic field to deflect the beam back and forth across the surface in a controlled manner. When the primary electrons in the beam hit the sample surface secondary electrons are emitted. These secondary electrons are accelerated towards the detector by a potential applied between it and the sample. Once amplified the response can be computed and displayed. The user can then control magnification and sample positioning through the computer interface.

Transmission Electron Microscopy, TEM

In TEM, a beam of high energy electrons pass through a thin sample revealing information on particle size, morphology, crystallography and the elemental composition. To simplify, the TEM can be compared to an optical light microscope where the sample is observed using an electron beam. It is possible for TEM to generate atomic-resolution images and give chemical information at a resolution of 1 nm or better. A simplified TEM schematic is shown

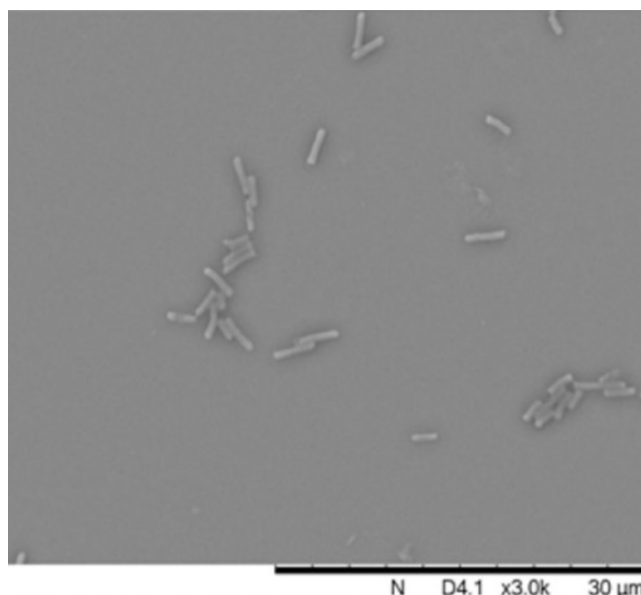


Figure 1.23 – SEM image showing *Escherichia coli* (*E.coli*) adhered to a silver nanocrystal film previously deposited on a microscope slide substrate.

in figure 1.24. The electron beam is generated from an electron gun heated through the application of a large current. Electrons leaving the gun are accelerated towards the specimen through the condenser lenses which focus the beam into a thin cylinder. During operation, electrons can be accelerated from 125 kV, depending on the particular microscope. The focused beam then strikes the specimen, where most of the electrons are transmitted through the thin specimen. The transmitted electrons are focused by the objective lens then projected through the projector lens on to the fluorescent plate or CCD. Some TEMs also collect backscattered electrons, secondary electrons and emitted photons for additional information.

The fact that it is possible to image and characterise an individual nanocrystal makes TEM an incredibly powerful technique for nano-materials analysis. A large range of materials can be characterised with TEM, including, metals, semiconductors, minerals, ceramics and polymers. The only requirement is that the specimen is suitably thin enough to transmit electrons through. An example TEM image can be seen in figure 1.25.

X-Ray Photoelectron Spectroscopy, XPS

X-Ray Photoelectron Spectroscopy (XPS) is a technique used for analysing surfaces. It can provide information about the presence of elements at the surface, their chemical and electronic states and how the properties vary over the first few atom layers. The process relies on the X-ray induced photoemission of electrons; spectra are produced by measuring the intensity and kinetic energy of emitted electrons. A typical XPS spectrum plots the number of

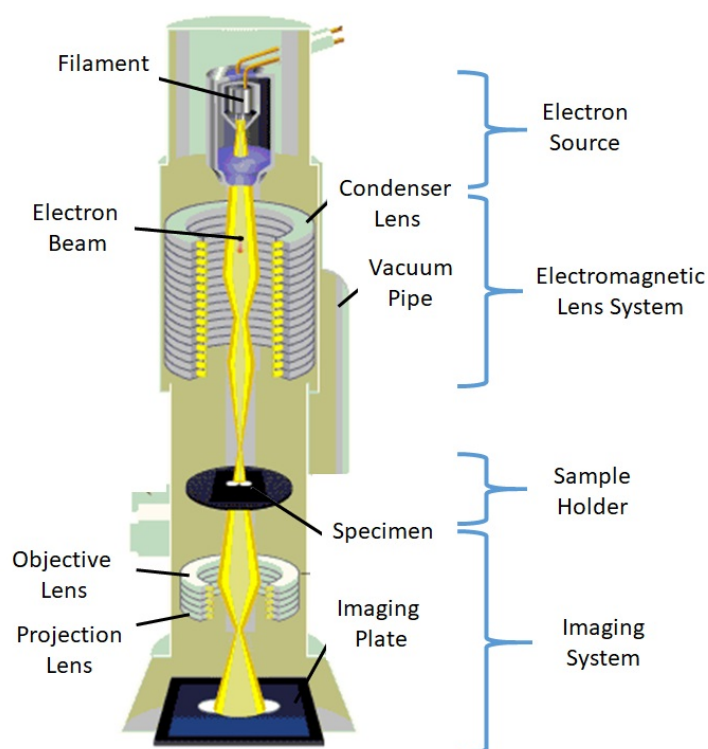


Figure 1.24 – Schematic of a Transmission Electron Microscope, showing the internal components. Schematic copied from <http://www.hk-phy.org>

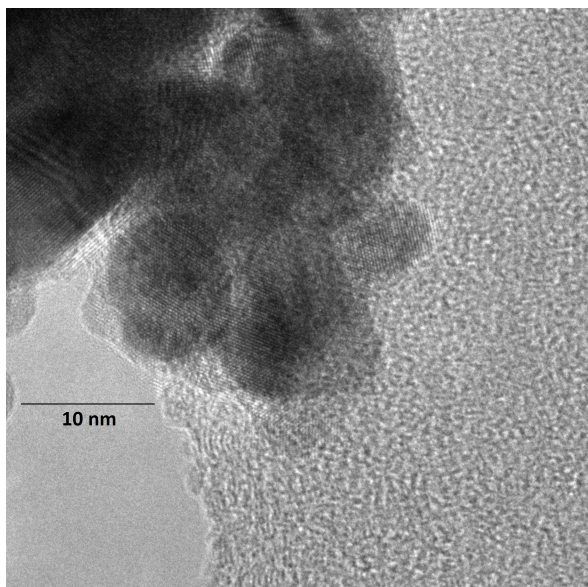


Figure 1.25 – TEM of $\text{Au}_{0.5}\text{Ag}_{0.5}$ nanocrystals generated at the water toluene interface. Films were sonicated in chloroform to distribute the nanocrystals and a single drop of the mixture was pipetted on to a holey carbon copper TEM grid. The scale bar shows 10 nm.

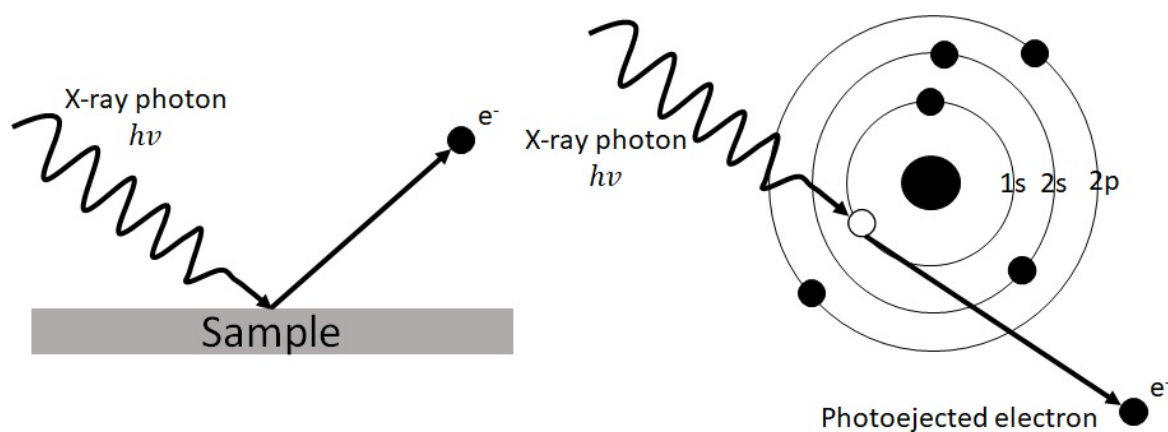


Figure 1.26 – Cartoon showing the generation of a photoelectron from an X-ray photon. The X-ray photon strikes the sample (Left), knocking out an electron (Right).

collected electrons against the binding energy. XPS peaks are characteristic to an element and its specific electronic state, allowing direct identification of the surface layers atoms of the analyte. The peaks correspond to the electron configuration of the electrons within each atom (1s, 2s, 2p, 3s, etc.).

The photoelectron occurs when a photon of sufficient energy hitting the surface manages to excite an electron, through the photoelectric effect. The excited electron is emitted from the material as a result of absorbing the electromagnetic energy of very short wavelength (figure 1.26). An XPS instrument will consist of an X-ray source, sometimes with a monochromator, and an electron detector capable of measuring the kinetic energy of the electrons striking it. These, along with the sample under investigation are held in a chamber at ultrahigh vacuum, to avoid electrons colliding with air molecules and losing energy.

1.5.2 Atomic Force Microscopy, AFM

Atomic force microscopy (AFM) provides a three-dimensional image of the surface being analysed. Surfaces being analysed need no special treatment or coatings that would irreversibly change the surface, such as when using carbon/gold sputter coatings for some SEM applications. AFM doesn't need the expensive high vacuum environments of the previously discussed techniques for operation. AFM modes can work well in ambient air or liquid environments, increasing the possible uses of AFM to include biological macromolecules and living organisms. An AFM comprises of a piezoelectric scanner sample bed, a cantilever with a sharp tip for "scanning" the surface and a laser, which is reflected off of the cantilever tip into a photodiode to collect the surface profile information. The cantilever tip is normally

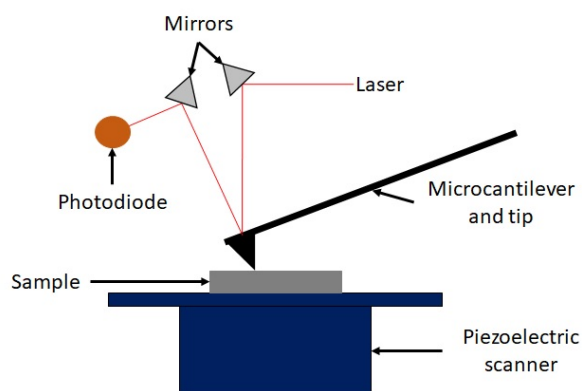


Figure 1.27 – Schematic of a typical AFM instruments internal workings. The deflection of the tip is measured using a reflected laser beam.

sharpened to a radius in the order of micro– or nanometres, depending on the image resolution required. When the tip is brought into contact with the sample surface the cantilever is deflected, due to the presence of forces between tip and sample. Deflection is measured using a laser spot reflecting between the cantilever and an array of photodiodes. Most AFM instruments employ a feedback mechanism to avoid contact between the tip and surface, which would cause irreparable damage. The feedback system works by keeping the tip to sample distance constant. To achieve this a piezoelectric crystal, which can move in the Z direction to maintain a constant force is employed, while scanning in x and y directions. A simplified schematic of this can be seen in figure 1.27.

1.5.3 UV/Visible Spectroscopy, UV/Vis

Ultraviolet–visible (UV/Vis) spectroscopy is a tool used in characterising materials. During a typical experiment, a sample is irradiated with electromagnetic radiation in the ultraviolet and visible ranges and the absorbed wavelengths are analysed through the resulting spectrum. The technique can be employed to identify substances, determine concentrations and identifying some functional groups. Photons in the visible range have wavelengths between 800–400 nm whereas the near UV range include wavelengths down to 200 nm.

Absorption of the visible and ultraviolet wavelengths by the material is associated with electron transitions between energy levels, generally from HOMO to LUMO. The wavelength absorbed is a measure of the energy gap between energy levels in the orbitals. Lambert’s law and Beer’s law have been formulated to describe absorption intensity. Lambert’s law states,

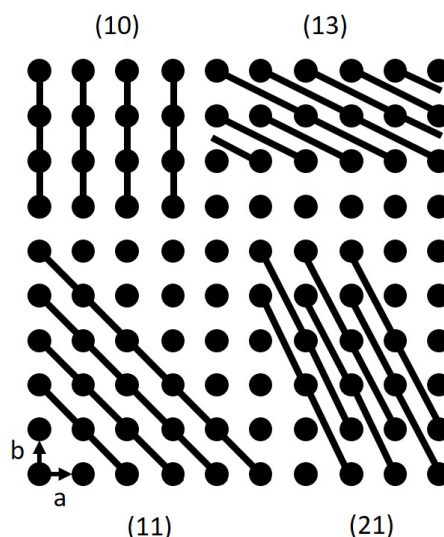


Figure 1.28 – An example of 2D Miller Indices.

the fraction of incident light absorbed is independent of source intensity. Beer's law states, absorption is proportional to the number of absorbing molecules. Combining these laws gives,

$$\log_{10} \frac{I_0}{I_{den}} = A = \epsilon \cdot l \cdot c \quad (1.22)$$

I_0 and I are the incident and transmitted light respectively, A is the absorbance, l is the path length in centimetres, c is the concentration in mol/dm^3 and ϵ is the molar extinction coefficient.

The electron excitation is accompanied with changes to the rotational and vibrational quantum numbers. Leading to a broadening of the fine absorption line containing the rotational and vibrational fine structure. Normally in the liquid state interactions between the solute and solvent blur leading to an smooth curve being observed.

It is also possible to observe size dependent properties in a UV/Vis spectrum, Including peak broadening and shifts in the absorption wavelength. Some electronic properties can also be determined through UV/Vis spectroscopy.

1.5.4 X-Ray Diffraction, XRD

X-ray diffraction (XRD) is a technique for the structural analysis of crystalline solids. The diffraction of X-rays by the core electrons within the solid provides information regarding the crystallographic structure, crystallinity, crystal size and preferred orientation of the sample. The method is based on the diffraction of X-rays ($\lambda \approx 10^{-9} - 10^{-11}$ m) by the core electrons

of the atoms making up the crystal lattice, which are of the same order of magnitude as the wavelength of the radiation. Solids analysed can be either single crystal, powder or even thin textured films.

A solid crystalline material can be thought of as a ordered array of atoms. The array forms as repeating blocks (unit cells). Within the sold it is possible to imagine families of planes passing through the unit cell at various angles. These planes can be thought of as mirrors to model the crystal, a stack of reflecting planes each with separation, d . Miller indices are used to define these planes, a set of 3 numbers (for three dimensions), labelled as h , k and l , which correspond to the vector normal to the planes they describe (Figure 1.28).

Formally diffraction can be regarded as a reflection of the X-rays from the lattice planes, whereby the angle of incidence corresponds to the angle of reflection. The absorption of X-ray radiation is so small that the different lattice planes are irradiated with the same intensity. As a result, reflected radiation from different layers of the crystal lattice interfere constructively causing amplification of the signal. Mathematically this law is described by the BRAGG equation (equation 1.23).

$$n\lambda = 2d \sin(\theta) \quad (1.23)$$

Where, λ = Wavelength of incident wave d = Spacing between layers of atoms θ = Angle between the incident rays and the surface of the crystal n = integer.

In an X-ray pattern the intensity of the diffracted rays is shown as a function of the angle 2θ (figure 1.29). For this purpose, the sample is irradiated with monochromatic X-rays, while a detector is guided on a circular path around the sample. Using the Miller indices (hkl), which can be assigned to each experimentally determined reflexes, and the interlayer spacing, the lattice constant of the unit cell can be determined. It is also possible to compare the diffraction pattern to a database of previously reported crystals.

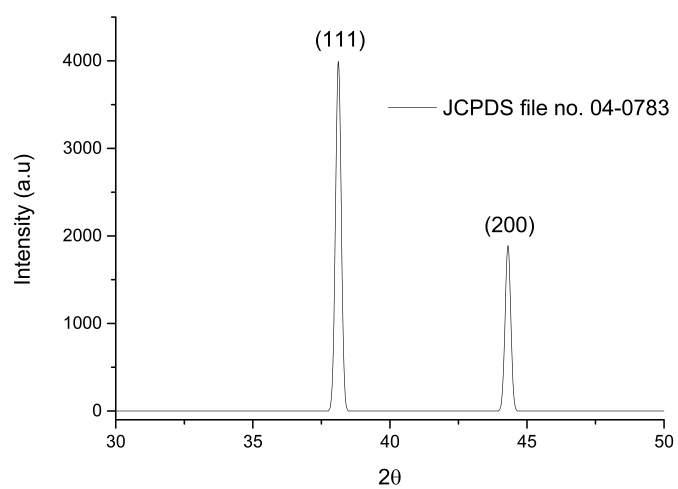


Figure 1.29 – XRD pattern of Ag taken from JCPDS file no. 04-0783. The Miller indices have been labelled above the peaks.

Chapter 2

Experimental and Context

2.1 Thin Films of Metal and Metal Alloy Nanocrystals

The thin films of metal and metal alloy nanocrystals used in this thesis were prepared using, chloro(triphenylphosphine)gold(I) ($\text{Au}(\text{PPh}_3)\text{Cl}$), chlorotris(triphenylphosphine)silver(I) ($\text{Ag}(\text{PPh}_3)_3\text{Cl}$), Copper cupferrate ($\text{Cu}(\text{Cup})_2$) and dichlorobis(triphenylphosphine)palladium(II) ($\text{Pd}(\text{PPh}_3)_2\text{Cl}_2$). Gold and palladium precursors were used as purchased, the silver and copper precursors were prepared using modified previously reported methods.^{66,136,137}

All chemicals were purchased from Aldrich, with the exception of chloro(triphenylphosphine)gold(I) (Acros Organics), they were all used as received with no further purification or analysis.

2.1.1 Synthesis of chlorotris(triphenylphosphine)silver(I)

The complex was prepared following a method previously reported.¹³⁶ Briefly, to a stirred dispersion of AgCl (1.43 g, 10 mmol) in dichloromethane (150 ml), a solution of triphenylphosphine (TPP) (10.97 g, 4 mmol), in dichloromethane (50 mL), was added drop wise and the stirring continued for an hour, during which time the solids almost completely dissolved. The clear liquid obtained was filtered and, to the filtrate, petroleum ether was added to precipitate a white crystalline solid. The solid was then washed with petroleum ether and air dried. The collected solid was used to produce thin films of Ag, at the interface of toluene and water, without any further purification. Elemental analysis (%) found: C, 69.45; H, 4.84; Cl, 4.23; P, 9.69; Ag, 11.02. Calcd: C, 69.71; H, 4.84; Cl, 3.82; P, 10.00; Ag, 11.62.

2.1.2 Synthesis of Copper Cupferrate

Copper cupferrate ($\text{Cu}(\text{Cup})_2$) was prepared as previously reported.¹³⁷ Briefly, to a stirred solution of CuCl_2 (0.607 g, 4.5 mmol) in 100 mL deionised water, a solution of cupferron (3.0 g, 19 mmol) in 700 mL deionised water was added dropwise. A grey/green precipitate

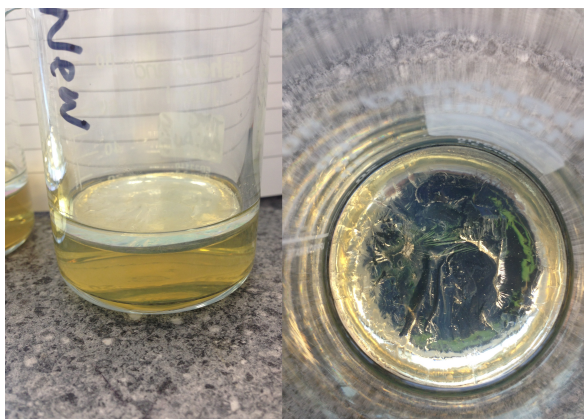


Figure 2.1 – Photographs showing the silver film at the water–toluene interface. Notice the reflective appearance of the film.

of $\text{Cu}(\text{Cup})_2$ forms, the solid was collected and washed with deionised water and dried in an oven at 100°C . The collected solid was used without any further purification or analysis.

2.1.3 Deposition of Nanocrystal Thin Films at the Water–Toluene Interface

In a typical preparation of Ag nanocrystal metal films, a toluene solution of chlorotris(triphenylphosphine)silver(I) ($\text{Ag}(\text{PPh}_3)_3\text{Cl}$), (10 mL, 1.5 mM), was layered on top of aqueous sodium hydroxide (16 mL, 6.25 mM) in a clean 100 mL beaker (diameter 4.8 cm). Identical beakers were used throughout to remove any effects caused by changing the diameter of the interface. The reactions were left to stand, to allow the phases to stabilise. To initiate the reaction, aqueous tetrakis(hydroxymethyl)phosphonium chloride (THPC, 80% wt% in water) (330 μL , 50 mM) was injected down the walls of the beaker. The beaker was immediately transferred to an oven set at 50°C . After around three hours, sometimes less depending on the metal being used, a film with metallic lustre was seen at the interface between toluene and water (Figure 2.1). The film was then transferred onto a substrate for further analysis. To obtain alloyed films, the reaction was carried out with equimolar solutions of $\text{Ag}(\text{PPh}_3)_3\text{Cl}$, $\text{Au}(\text{PPh}_3)\text{Cl}$ and $\text{Pd}(\text{PPh}_3)_2\text{Cl}_2$, mixed in different proportions. For example, to produce a $\text{Au}_{0.7}\text{Ag}_{0.3}$ alloy, a toluene layer with 7 mL 1.5 mM $\text{Au}(\text{PPh}_3)\text{Cl}$ solution and 3 mL 1.5 mM $\text{Ag}(\text{PPh}_3)_3\text{Cl}$ was employed. A schematic of the two phase method can be seen in figure 1.8.

2.1.4 Film Transfer from the Water–Toluene Interface

Films of metallic nanocrystals prepared at the interface were collected in one of three methods (Figure 2.2). A polystyrene support was created by the addition of polystyrene beads to the



Figure 2.2 – Photographs showing the silver film supported on polystyrene (left) and 1.5 x 1.5 cm glass supports (right). Note the reflection shown by the silver on glass.

toluene. Evaporation of the toluene resulted in a polystyrene supported film which could be easily removed and manipulated.

Films were also transferred onto a glass substrate by piercing the film with a small piece of glass and gently lifting the substrate diagonally through the film to deposit a thin layer of nanocrystals onto the glass. The glass supported films were left to dry in air or in an oven at 50 – 60 °C. They were later dipped in fresh toluene and dried to remove unreacted material from the surface, resulting in a more reflective sample.

Films produced for heterogeneous catalysis studies were collected on to Whatman™ PTFE membrane circles. The two phase reaction solution was collected and toluene removed by pipette. The resulting aqueous solution and solid film was filtered through the membrane allowing the nanocrystals to collect on the PTFE circle. The PTFE circles were left to dry in the air cut into 5 mm strips and stored for later use.

2.1.5 Ligand Exchange

To investigate the effects of supporting ligands on the metallic nanocrystals. Nanocrystal films, mounted upon glass substrates, were submersed into 20 mL of a 1–2 mM solution of the desired ligand. The films were then left to soak for 24–48 hours in the fridge during which time ligand exchange occurred. Films were removed from the ligand solution and washed gently with two portions of methanol or water, depending on the solvent used. Films were then left to dry completely in air.

2.1.6 Charge Transport Measurements

Charge transport measurements for metallic nanocrystals were carried out using a home-built system that comprised a cold finger, which was incorporated into a closed-cycle He cryostat. The metallic nanocrystal film to be analysed was mounted onto a cold finger with copper wires attached to the film using a highly conductive araldite or "glue". A feed through enabled

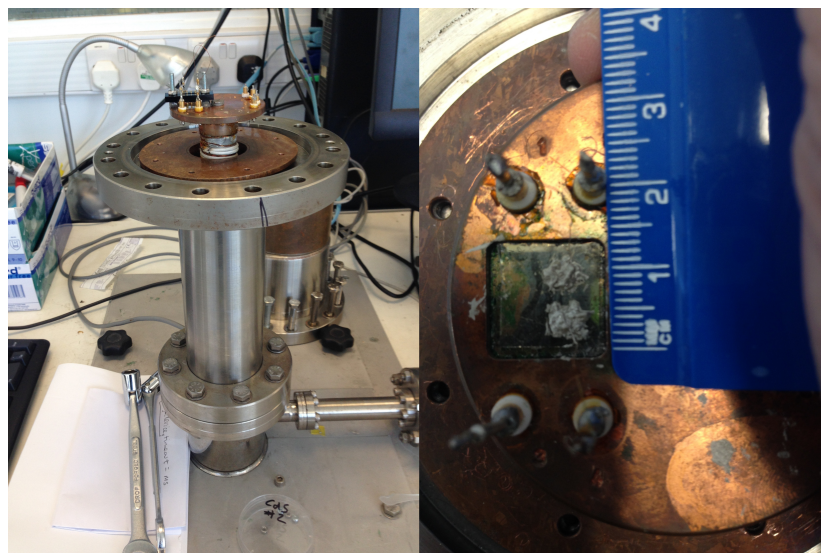


Figure 2.3 – Photographs showing the UHV rig (left) and a sample post measurement (right).

the copper wires to be attached to a Keithley 2400 Series Source–Measure unit, as the cold finger was closed and sealed off from the atmosphere, to allow the measurements to be carried out. Finally, a Lakeshore 325 Temperature Controller was included into the set–up in order that the temperature be accurately monitored and controlled throughout the charge transport measurements. A photograph for the home–built charge transport measurement apparatus is shown in Figure 2.3. The whole system was held at a vacuum of 10^{-6} mbar employing both a rotary pump and a diffusion pump.

Once at a suitable vacuum the sample was cooled to 10–15 K using the closed–cycle cryostat. During cooling, and subsequent reheating the resistance of the films was measured. A voltage was applied to the film across the attached copper wires and the resulting current was obtained. A home–made python programme has been written to control the data collection and real–time plotting of collected data. Data collected can then be imported into any graphical analysis package and further processed.

2.2 Characterization Methods

X–ray diffraction was carried out on films deposited on glass substrates using a Bruker AXS D8 diffractometer with a Cu $K\alpha$ source. Atomic force microscopy was carried out using a Nanoscope IIIa microscope operating in tapping mode on interfacial deposits transferred to mica substrates whose surface was freshly cleaved. Scanning and transmission electron microscopy was carried out on Delong Instruments LVEM5 microscope with a FEG gun operating at 5 keV. High resolution SEM and energy dispersive X–ray analysis was carried out

using a Phillips XL30 FEG SEM. Samples for TEM were prepared by dispersing the films in chloroform by sonication, followed by drop casting on holey carbon coated Cu grids. FT-IR was carried out using a Bruker Alpha II spectrometer fitted with an ATR attachment. Proton NMR was carried out using Bruker 400 MHz spectrometer using a dispersion of the sample in CDCl_3 . Surface topography of Ag nanocrystal films on glass were characterised using a STIL Micromesure 2 confocal chromatic imager, employing a scan area of $25 \times 25 \mu\text{m}$ using a step size of 75 nm. Film thickness of Ag was approximated using both the Micromesure and a Taylor Hobson Form Talysurf Series 2 stylus profilometer.

2.3 Annealing Metallic Nanocrystals Deposited on Glass Substrates

Nanocrystal films of Au, Ag and AuAg alloys on glass supports have been annealed at temperature between 120 and 180 °C. Samples were heated to the chosen temperature in a muffle furnace and held at temperature for 3 hours before cooling. The annealed nanocrystal films were stored in the air prior to further work. Nanocrystal films were analysed by XRD and the charge transport properties were measured.

2.4 Catalytic Studies of Nanocrystals

Nanocrystals of Ag, Au, $\text{Ag}_{50}\text{Pd}_{50}$ and $\text{Au}_{50}\text{Pd}_{50}$ on Whatman™ PTFE membranes were investigated as reusable homogeneous catalysts in the reduction of 4-nitrophenol (4-NP) and nitrobenzene. The nanocrystals were also tested for their use as catalysts in the hydrogenation reaction of cyclohexene.

2.4.1 Catalysed Reduction of 4-Nitrophenol and Nitrobenzene

The reduction of 4-nitrophenol (4-NP) was carried out in a cuvette. A typical procedure used aqueous 4-NP (2.5 mL, 0.12 mM). A 5 mm strip of Whatman™ PTFE membrane containing the nanocrystals being tested was placed down the side of the cuvette, so as not to obscure the UV beam path. Freshly prepared NaBH_4 (3 drops, 3 M) was added to the cuvette to initiate reduction. The reaction mixture gradually changed from yellow to colourless and H_2 bubbles were observed. The supported catalysts were recycled up to 5 times using the same procedure employing fresh 4-NP and NaBH_4 each time. The progress of all reactions was followed by UV/Vis spectrometry (250–500 nm, scanning every 30 seconds). Reduction reactions with nitrobenzene were carried out in the same procedure replacing the 4-NP with aqueous nitrobenzene (2.5 mL, 0.32 mM).

2.4.2 Catalysed Hydrogenation of Cyclohexene

Hydrogenation reactions were carried out homebuilt set-up, equipping a commercially available laboratory pressure reactor and bench top H₂ generator. The sealed vessel, a tinyclave from büchiglasuster, equipped with a glass reaction chamber, was attached to a Peak Scientific, Precision Hydrogen, bench top hydrogen generator and a nitrogen bottle.

A typical reaction employed a 10 ml, 1:1, mixture of the cyclohexene and chloroform. Chloroform was chosen as the solvent as it could be easily evaporated and would not interfere with crude NMR studies in deuterated chloroform (CDCl₃). A 5 mm strip of Whatman™ PTFE membrane containing the nanocatalyst (either, Au₅₀Ag₅₀, Au₅₀Pd₅₀, Ag₅₀Pd₅₀) under testing was added to the reaction along with a magnetic stirrer bar. The tinyclave was assembled and atmosphere purged. The atmosphere in the vessel was purged by charging with around 3 bar nitrogen and releasing 3 times before charging with around 3 bar hydrogen and releasing. The third hydrogen charge and sealed into the vessel. The hydrogenation reaction was then heated to 100 °C in an oil bath with stirring for 5 hours. Reactions were removed from the oil bath and left to cool overnight before releasing contained pressure and opening to the air. The reaction liqueur was left towards the back of a fumehood to allow the chloroform solvent to mostly evaporate. A crude proton NMR was performed on the remaining liqueur to identify the presence of any expected hydrogenated product.

2.5 Preparation of a Single Phase Silver Nanocrystal Hydrosol

The single phase reduction of chlorotris(triphenylphosphie)silver(I) by hydrolysed THPC was carried out in the following method.

THPC (640 µL, 50 mM in water) was added to a stirred methanol (25 mL) solution of (Ag(PPh₃)₃Cl) (15.72 mg, 0.0169 mmol). After 30 minutes all solids had fully dissolved. Aq. NaOH (0.280 mL, 1 M) was injected into the stirred solution and left stirring for 1 hour, after which a tan/brown suspension of nanocrystals had formed. Nanocrystals were collected by evaporation of the methanol, before sonication in D₂O for NMR studies.

2.6 Inorganic Chalcogenide Ligand Synthesis

Synthesis of $\text{Na}_4\text{SnS}_4 \cdot 18\text{H}_2\text{O}$

The inorganic ligand Na_4SnS_4 was prepared following the reported procedure.^{138,139} Briefly, a solution of SnCl_4 (10.53 g, 30 mmol) was added dropwise to a stirred solution of $\text{Na}_2\text{S} \cdot 9\text{H}_2\text{O}$. The reaction was kept iced until completion. It was observed that the solution was clear and pale green on completion. MgO (2.0 g) was added to the pale green solution and heated for 2 hours to remove impurities. After heating, the solution was filtered warm to remove the MgO and volume reduced to around half. The remaining solution was poured into acetone and stored in the fridge to precipitate out the desired product. The precipitate was collected and dried under vacuum. Elemental analysis (%) found: Na, 15.12; S, 18.68; H, 3.70. Calculated: Na, 13.87; S, 19.34; H, 5.48;

Chapter 3

Thin Nanocrystalline Films of Metal and Metal Alloys

3.1 Introduction

Two dimensional lattices of nanocrystals have been previously obtained from a variety of metal, semiconductor and oxide nanocrystals. These have been prepared in various methods including, deposition, spin coating and evaporation.^{3,40–46,94,110,140–143} Annealing of arrays of nanocrystals has been previously investigated showing increased conductivity for PbSe nanocrystal arrays.¹⁴⁴ Whilst mild annealing of arrays has also been utilised to remove surface ligands exposing surface atoms.¹⁴⁵

It has been suggested that the water–toluene interface will create Janus nanocrystals, consisting of two distinct surface ligand regimes. Luo and colleagues used a toluene in water emulsion to synthesise nanocrystals of Ag from Ag(PPh₃)Cl and THPC. Using NOSEY NMR spectroscopy they were able to identify separate regions of lipophilic and lipophobic surface ligands.¹⁴⁶ More recently Li has synthesised amphiphilic Janus Au nanocrystals containing both D-penicillamine and benzyl mercaptan surface ligands.¹⁴⁷

This thesis uses the water–toluene method for nanocrystal synthesis previously used by Rao and co workers.^{40,94} The method had been used to synthesise nanocrystalline films of metal (Au and Ag) and metal alloys (AgAu, AuPd and AgPd). The following chapter reports the characterisation of generated films using a selection of techniques. The chapter will also attempt to characterise differences when annealing Ag and Au nanocrystalline films on glass. In light of previous amphiphilic Janus nanocrystal studies^{146,147} an attempt to investigate if the films produced using the interface method match the Janus nanocrystal thinking.

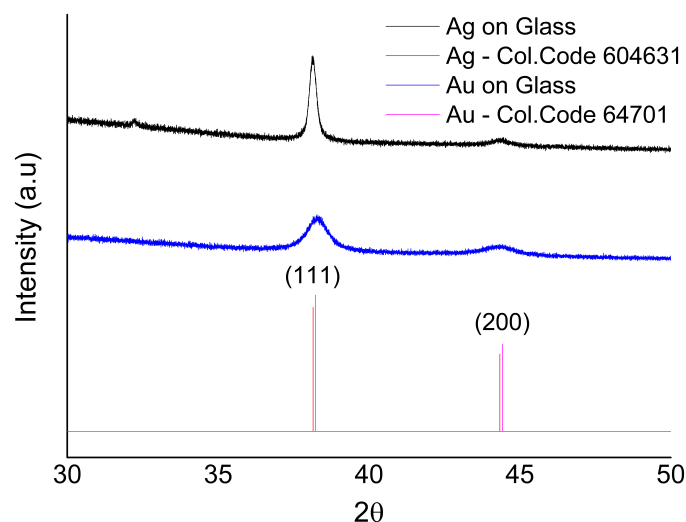


Figure 3.1 – X-ray diffraction patterns of a silver (black) and gold (blue). Cubic Au and Ag reference data from using collection codes 604631 (Ag) and 64701 (Au) has been included. The data has been stacked for clarity. Films all generated at the interface of toluene and water for 3 hours at 50 °C. Films were then deposited onto glass substrates.

3.2 Characterisation of Nanocrystalline Films of Metal and Metal Alloys

Films of metal and metal alloy nanocrystals generated at the water–toluene interface have been transferred on to glass and polystyrene substrates where they could be later characterised. XRD, AFM SEM and UV/Vis characterisation could all be completed without further processing of the films on their substrates. TEM required sonication of the films in chloroform to break up the films before a single drop of the resulting liquor was added onto a holey carbon copper mesh. XPS was performed both on glass and iridium metal substrates.

3.2.1 Results and Discussion

The structure of silver and gold films was initially analysed by XRD. Figure 3.1 reveals a pattern typical of bulk Au and Ag for the films on glass substrates. The slightly broader peaks are characteristic of nanocrystals. The peaks around 38.1 degrees are the (111) planes and the peaks around 44.3 are for the (200) planes. A higher degree of orientation for the (111) peaks is apparent from the higher intensity of the peaks. It is possible using the pattern to calculate the unit cell size for the gold and silver films. Using the formula linking d , the separation of planes, a the unit cell dimension and the miller indices (h,k,l) (equation 3.1) and combining

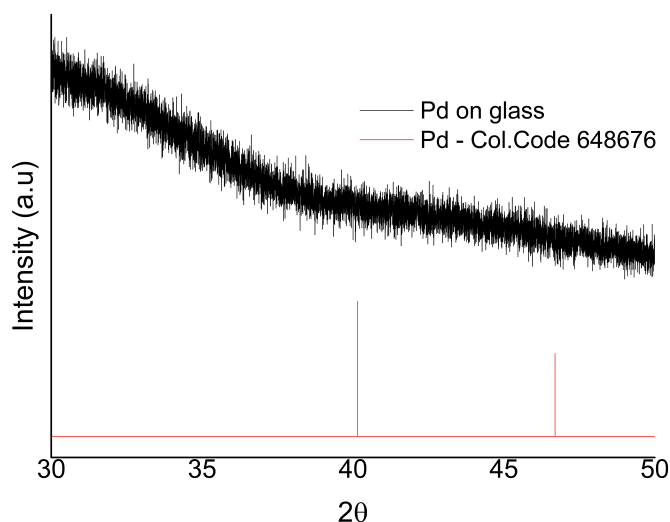


Figure 3.2 – X-ray diffraction pattern of pure palladium . Cubic palladium reference data from collection code 648676 has been included and data stacked for clarity. Cracked and broken films were prepared at the interface of toluene and water after 3 hours at 50 °C. It was then possible for fragments to be deposited onto glass substrates for analysis.

with the Bragg equation (equation 1.23) it is possible to calculate the unit cell parameters for the cubic gold and silver lattices.

$$d = \frac{a}{\sqrt{h^2 + l^2 + k^2}} \quad (3.1)$$

When combined with the Bragg equation the following formula is generated;

$$a = \frac{\lambda \sqrt{h^2 + l^2 + k^2}}{2 \sin(\theta)} \quad (3.2)$$

Using the θ values for the (111) miller indices measured from the XRD patterns of silver and gold the unit cell parameters are calculated as 4.085 Å and 4.069 Å respectively. Compared to reported values of 4.09 Å 4.08 Å for silver and gold.^{148,149}

It was also possible to synthesise pure palladium nanocrystals using the same method. However, these did not self assemble into the smooth unbroken films at the interface as gold and silver nanocrystals did. The films were broken and fragmented, with some settling down to the bottom of the beaker, no longer supported by the interface forces. Figure 3.2 shows the XRD pattern collected from the fragmented films deposited on glass. However, the deposited films were unsuitable for XRD analysis, they were extensively broken rough. It was not

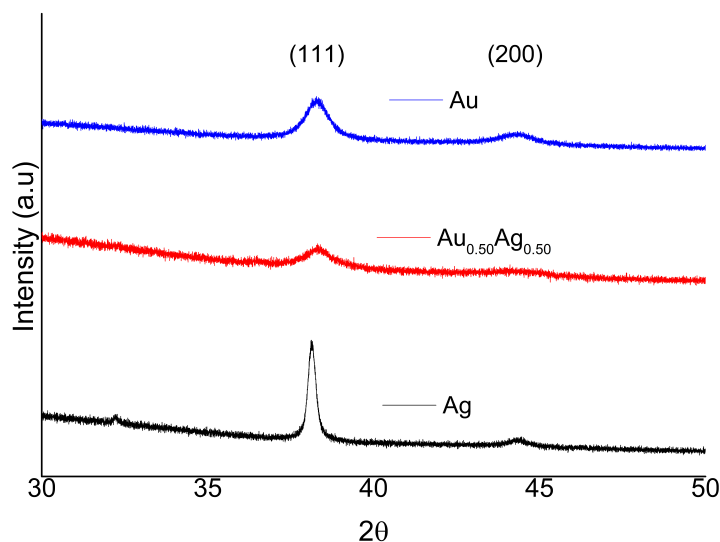


Figure 3.3 – X-ray diffraction patterns of a silver (black), gold (blue) and silver–gold alloy (red) film on glass. Films all generated at the interface of toluene and water for 3 hours at 50 °C. Films were then deposited onto glass substrates.

possible to collect a reflection pattern for any of the expected planes. Other characterisation techniques did, however, prove that the fragments synthesised were palladium.

Alloyed nanocrystals of $\text{Ag}_{0.25}\text{Au}_{0.75}$, $\text{Ag}_{0.50}\text{Au}_{0.50}$ and $\text{Ag}_{0.75}\text{Au}_{0.25}$ prepared on glass substrates were analysed and compared to the pure nanocrystal materials. Figure 3.3 shows the XRD pattern for the $\text{Ag}_{0.50}\text{Au}_{0.50}$ alloy. The (111) and (200) peak positions for the $\text{Ag}_{0.50}\text{Au}_{0.50}$ alloy lay between those for the pure materials, as is expected by Vegard's Law. Vegard's Law states that the lattice parameter of simple alloys are expected to follow the rule of mixtures, in which the lattice parameter is simply the weighted average of the two parts.¹⁵⁰ However the observation is somewhat masked by the broad peaks, characteristic of nanocrystals.

AuPd and AgPd nanocrystal films were deposited on glass and polystyrene supports. The XRD patterns for AuPd are shown in figure 3.4. The patterns for polystyrene backed nanocrystals show a high noise to signal ratio with very small intensities reported. It was decided that no further analysis was to be performed on the polystyrene backed films. The support method was however a cheap and effective way to collect and store the nanocrystals but could not be used for further analysis. AuPd films deposited on glass substrates produced more intense reflections than polystyrene, possibly due to a smoother more uniform support surface.

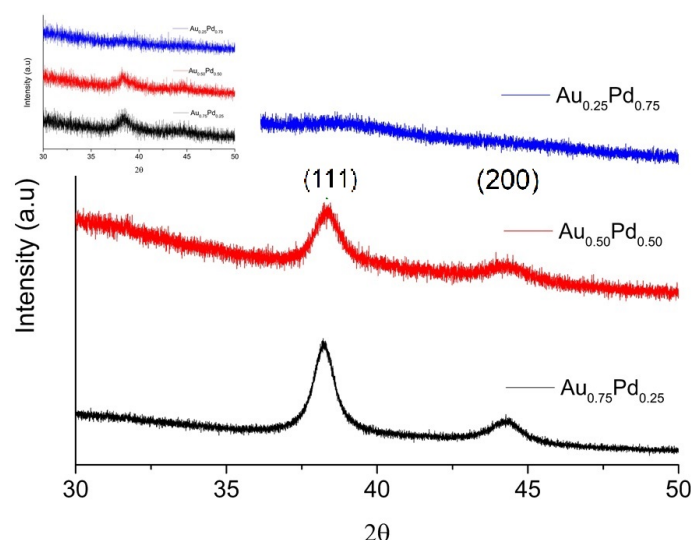


Figure 3.4 – X-ray diffraction patterns of AuPd nanocrystal films on glass and polystyrene (inset). Peaks shown refer to the miller indices (111) and (200). Films are all generated at the interface of toluene and water for 3 hours at 50 °C. Films were then deposited onto glass substrates or polystyrene beads added to the toluene phase post film generation. Toluene was left to evaporate leaving a polystyrene backed nanocrystal film.

The intensities and resolution of the patterns decreased as the concentration of palladium increased, from 0.00 to 0.75. The look and feel of the films became thinner and more fragile with increased palladium content, similar to the experience with pure palladium. Using the θ value for the (111) miller indices, measured from the XRD pattern of $\text{Au}_{0.75}\text{Pd}_{0.25}$ on glass, the unit cell parameter was calculated as 4.07 Å. The reported value falls between the previously published unit cell parameters for pure gold (4.08 Å) and palladium solids (3.89 Å).

Figure 3.5 shows the XRD pattern of $\text{Ag}_{0.50}\text{Pd}_{0.50}$ it appears that peaks corresponding to both silver and palladium, are present, although not clear. Leading us to believe alloying is either incomplete, or there is a phase separation between the two metals, meaning the feed ratio of starting materials does not correspond to the final alloyed material. It was expected that they would alloy in the same way as AuPd, however the evidence does not support that theory. It does appear that there is some alloying as the (111) peak at 38.2 degrees is shifted right and broader than the pure nanocrystal counterpart. There is however clearly two peaks around the (200) peaks, one for silver and a second for palladium, 44.8 degrees and 46.4 degrees respectively, these are believed to relate to a silver rich and palladium rich alloy in a phase separation.

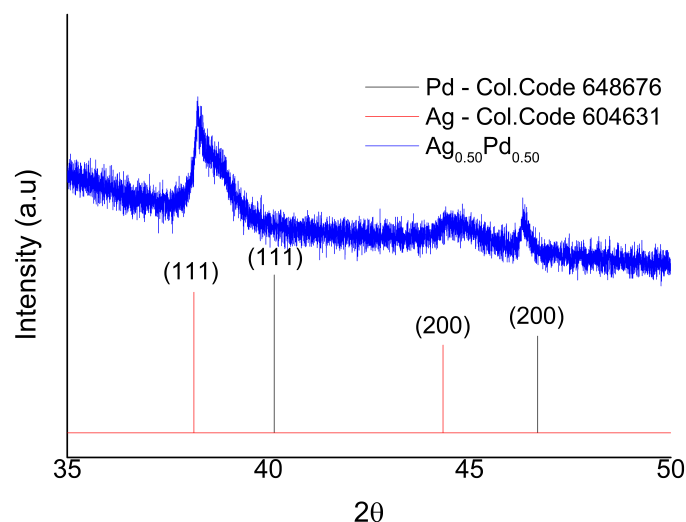


Figure 3.5 – $\text{Ag}_{0.50}\text{Pd}_{0.50}$ nanocrystal film on glass. Miller indices (111) and (200) for both silver and palladium are shown from reference data. Films all generated at the interface of toluene and water for 3 hours at 50°C . Films were then deposited onto glass substrates or polystyrene added to the toluene phase post film generation. Toluene was left to evaporate leaving a polystyrene backed nanocrystal film.

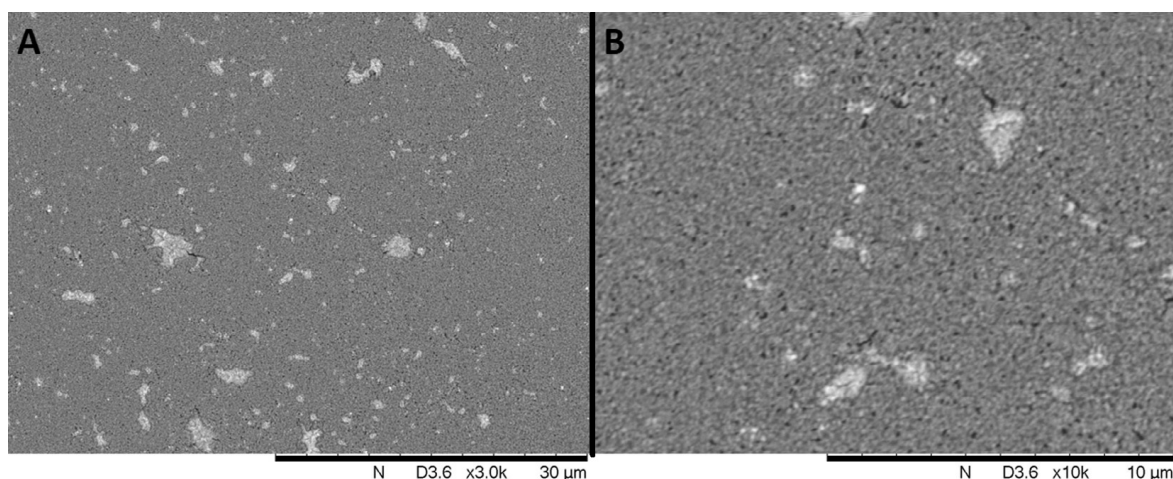


Figure 3.6 – Scanning electron microscope (SEM) images of Ag films deposited on glass at (A) 3000x and (B) 10000x magnification.

Scanning electron microscopy (SEM) has been used to visualise nanocrystal films of silver, gold and gold–silver alloys deposited on glass substrates. Scanning electron microscopy for deposited Ag nanocrystal films on glass are shown in figure 3.6. These films demonstrate a smooth film with a good level of coverage. There is also evidence of some aggregates having formed into visible clumps. It was later identified that by adding a washing step, a gentle submersion in toluene, surface aggregates could be greatly reduced.

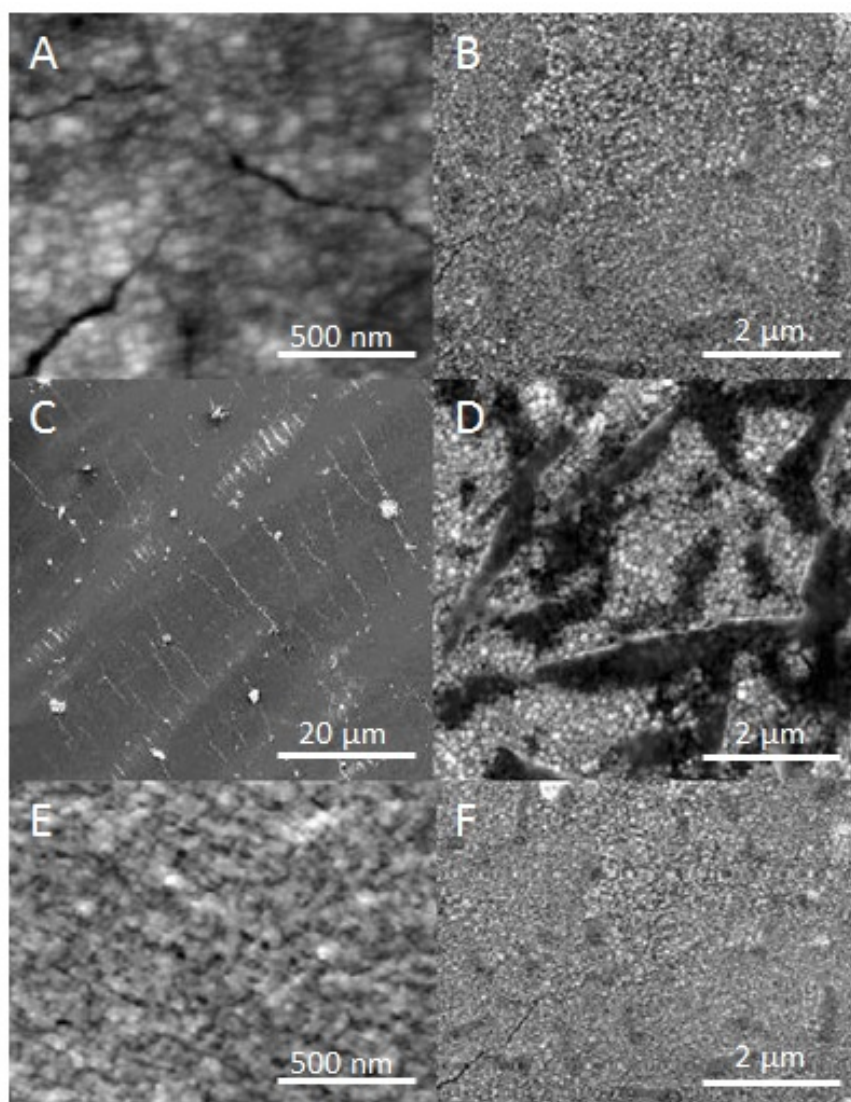


Figure 3.7 – Scanning microscope images of films deposited on glass. (A) High magnification image of Au nanocrystal film. The visible cracks are due to solvent evaporation post-deposition. (B) low magnification image of the same film, showing the continuous and uniform deposit over several square millimetres. (C & D) Low and high magnification images of Ag nanocrystal films deposited on glass. (E & F) Low and high magnification images of $\text{Au}_{0.50}\text{Ag}_{0.50}$ nanocrystal films deposited on glass.

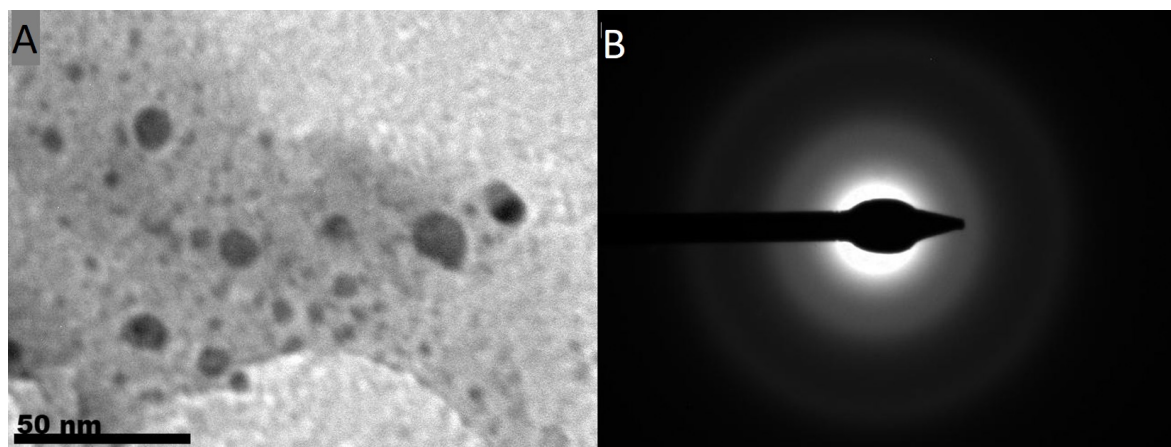


Figure 3.8 – (A)TEM image showing several Ag nanocrystals. (B) Selected area diffraction pattern of a typical Ag nanocrystal showing evidence of polycrystallinity.

Figure 3.7 shows highly uniform and continuous films over several tens of microns. Folds and cracks within the films are visible. At the higher resolutions irregular globular clusters with sizes in the range of tens of nanometres can be seen across all films. The edges of clusters are jagged due to the presence of smaller particulates. Interestingly, changes in the composition of nanocrystal alloys produced little change in the deposited $\text{Au}_x\text{Ag}_{1-x}$ materials.

Chloroform suspensions of Au, Ag, alloy nanocrystal films and Pd fragments were obtained by sonication of the collected material. A single drop of the resulting suspension was then dropped onto a holey carbon coated copper TEM disk for use in studies. The relative ease of material break up and removal from the substrate suggests that nanocrystal fragments may not be strongly bound to each other and the surface. Figure 3.8A shows a TEM image of sonicated Ag nanocrystals. Particle size analysis over multiple images provides an average particle size of $10.6 \text{ nm} \pm 6.83$. The relatively high standard deviation is an indication of a wide spread of particle sizes. There are a small number of large agglomerates (the largest measured 52 nm) and some much smaller Ag particles, in the order of 5 nm. Due to the sonication step in the sample processing some agglomeration is expected to have been lost. Therefore, the observed sizes are expected to be a lower limit of those making up the film as deposited onto glass. Figure 3.8B displays a selected area electron diffraction (SAED) pattern for the Ag nanocrystals. The concentric rings shown indicate polycrystallinity. The individual diffraction spots seen in SAED patterns of highly crystalline nanocrystals are not observed.^{151–153}

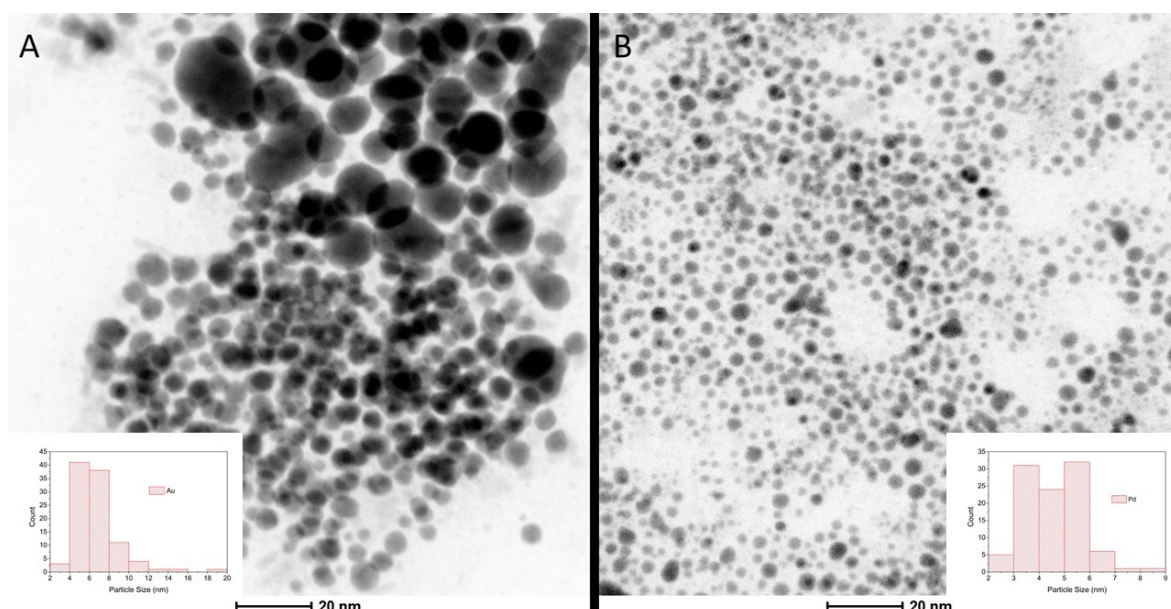


Figure 3.9 – TEM images of (A) gold and (B) palladium nanocrystals, scale bar shows 20 nm. Inset particle size histograms.

Pure Au and Pd TEM images are shown in figure 3.9. Figure 3.9A shows Au nanocrystals with an average particle size, over multiple images, of $6.89 \text{ nm} \pm 2.30$. As with Ag there are a number of large agglomerate particles, the largest measuring 18.7 nm. Figure 3.9B shows the Pd nanocrystals with average particle sizes of $4.51 \text{ nm} \pm 1.27$. These are smaller and there are less large agglomerates than the Ag and Au examples, possibly due to the original films not self assembling in the beaker. The largest measured agglomerate is in the order of 8.8 nm.

It was possible to collect some fragmented palladium nanocrystal array generated at the toluene water interface on glass. TEM images of the collected palladium is shown in figure 3.10.

Alloys of gold and palladium nanocrystals formed at the interface were collected and prepared, in the same method, for HRTEM–HAADF coupled with energy dispersive x-ray spectroscopy (EDS) analysis. High angle annular dark field (HAADF) imaging collects the very high angle scattered electrons to create the image. EDS is a method used for the identification of elemental compositions. The experiment can be completed using a very small amount of sample. Electrons exciting the material produce an X-ray emission, which is unique to each element. Meaning compositions can be identified within an alloy cluster. Figure 3.11 shows the HAADF image for a $\text{Au}_{0.50}\text{Pd}_{0.50}$ alloy. The red shaded image indicates gold nuclei and the green shaded image the palladium. From the image it can be deduced that the alloy feed

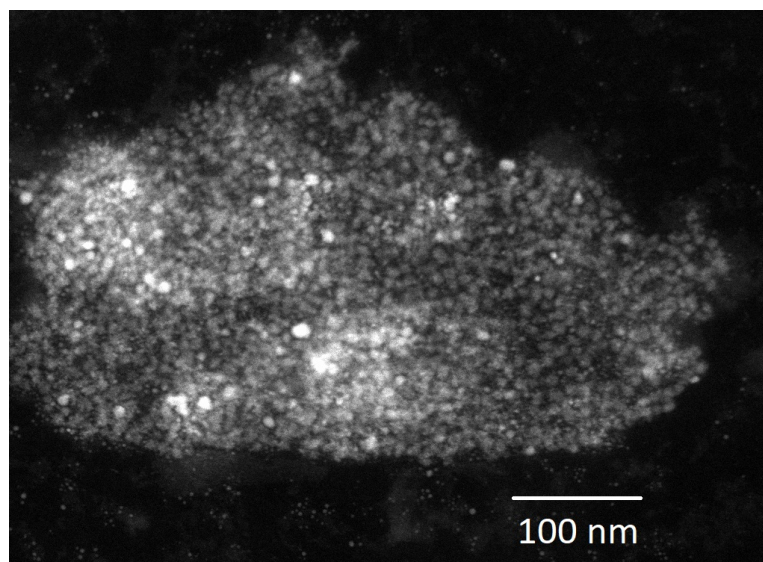


Figure 3.10 – TEM image of pure palladium nanocrystals prepared at the interface of toluene and water, 50°C 3hours. The scale bar shows 100 nm.

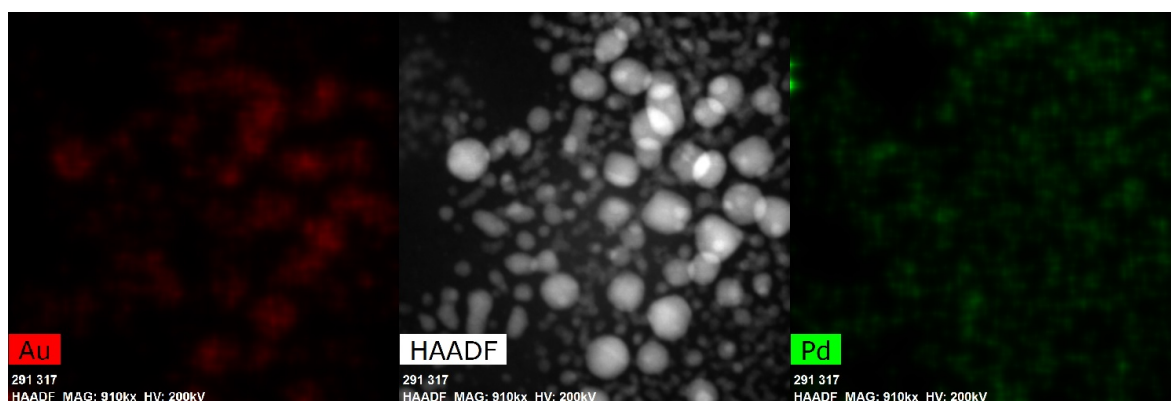


Figure 3.11 – HRTEM-HAADF images showing $\text{Au}_{0.50}\text{Pd}_{0.50}$ alloy (middle). The gold content (left, red) and palladium content (right, green) have been calculated using EDS and shown as a colour map.

ratio matched the final material produced, similar to previous reports producing gold–silver and gold–copper alloys.⁵²

Using the same method, alloys of silver and palladium were also analysed. The EDS for two clusters of $\text{Ag}_{0.50}\text{Pd}_{0.50}$ film is shown in figure 3.12. The top images show a silver rich alloy within a phase separation and the bottom images show a palladium rich alloy. The information here corresponds with the $\text{Ag}_{0.50}\text{Pd}_{0.50}$ film XRD in figure 3.5 where a range of peaks from both pure and alloyed compositions could be seen. The alloys of silver and palladium therefore do not follow the feed ratio as was found with gold silver alloys.

The 3D surface topography for a silver nanocrystal film was characterised and is shown in figure 3.13. The scanning area was 25 x 25 μm , with a step size of approximately 75 nm.

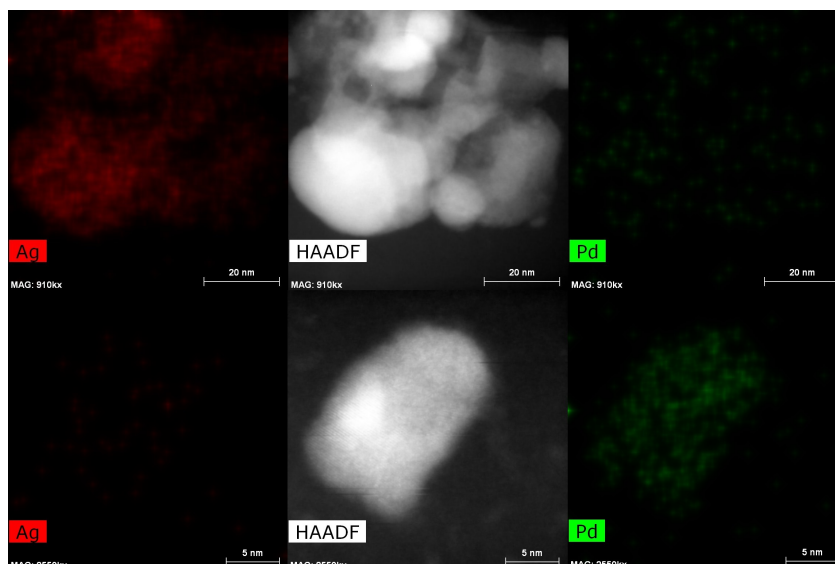


Figure 3.12 – HRTEM–HAADF images showing two areas of nanocrystals from a $\text{Ag}_{0.50}\text{Pd}_{0.50}$ alloy synthesis (middle). The silver content (left, red) and palladium content (right, green) have been calculated using EDS and shown as a colour map. The top images indicate a silver rich alloy fragment and bottom images a palladium rich alloy fragment.

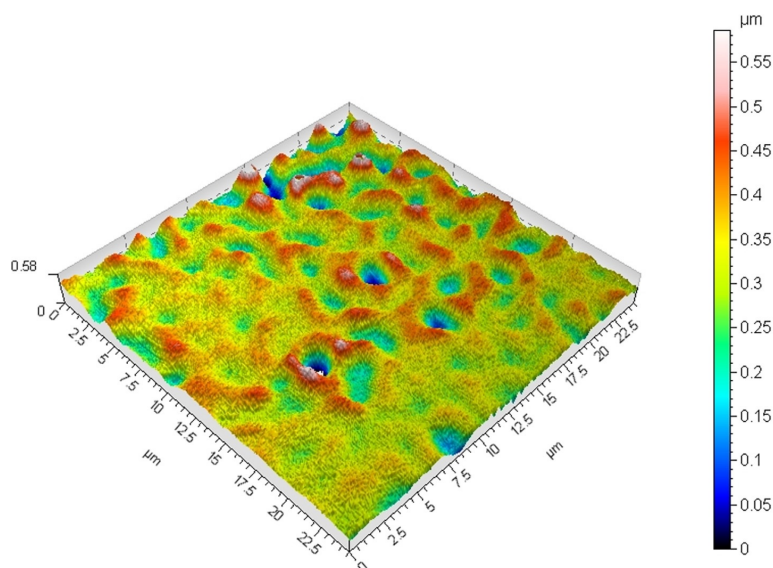


Figure 3.13 – 3D surface profile showing a silver nanocrystal film on glass substrate.

The mean surface roughness was found to be 7.36 nm, suggesting a relatively uniform film deposited on the substrate. The presence of some high peaks and valleys is evident. these could be the cracks and pinhole defects seen in some of the SEM images.

X-ray photoelectron spectroscopy (XPS) has been conducted on pure silver, silver–palladium ($\text{Ag}_{0.50}\text{Pd}_{0.50}$) and gold–palladium ($\text{Au}_{0.50}\text{Pd}_{0.50}$) nanocrystal films. Silver samples were deposited on glass substrates for analysis. The alloy samples were deposited onto thin iridium sheet for analysis. Figure 3.14A shows the XPS spectra from a silver nanocrystal film scan

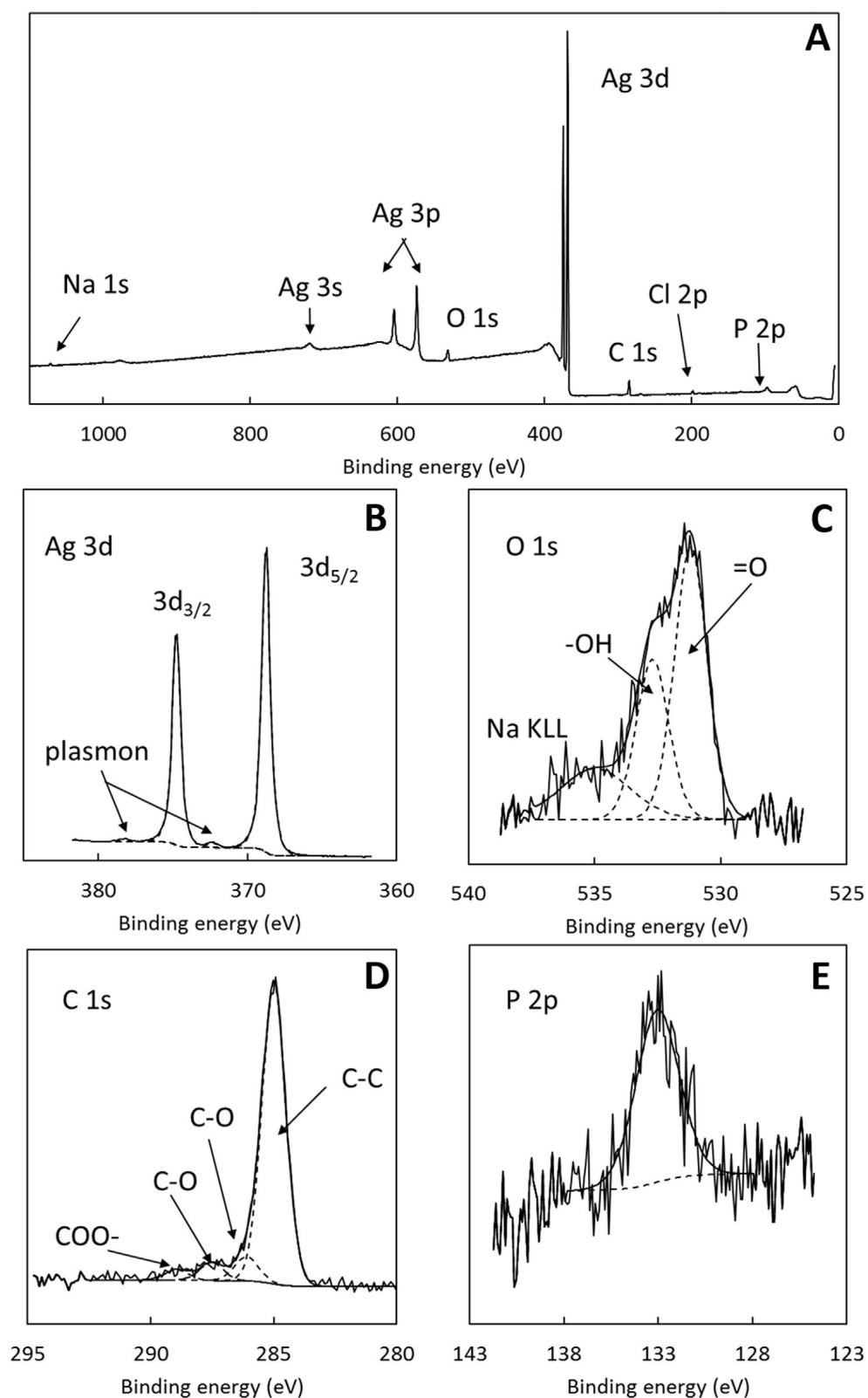


Figure 3.14 – XPS spectra obtained from the silver nanocrystal film survey scan (A). High resolution scans over Ag 3d, O 1s, C 1s, and P 2p are also shown (B-E).

survey, the summary of elemental composition can be seen in table 3.1. As was expected, for

Table 3.1 – XPS surface composition results from a silver nanocrystal film deposited on glass.

Element & photoelectron line	Composition, atom %
Ag 3d	52.3
O 1s	12.9
C 1s	27.4
Cl 2p	2.8
P 2p	2.5
S 2p	1.1
Si 2s	0.4
Na 1s	0.7

a silver film, the dominant element in the film is silver (52.3%). Binding energy of the Ag 3d_{5/2} peak was found to be 368.2 eV. Slightly higher than the accepted reference value of 368.2 eV for a bulk silver sample.¹⁵⁴ The plasmon peaks visible in figure 3.14B at around 4 eV displaced from the parent peaks indicate a metallic structure, suggesting the nanocrystals are sufficiently large enough, or the film stable enough, to maintain a metal-like electronic structure, typical of bulk silver. There is insufficient oxygen present (12.9%) for the shift to be accounted for by silver oxide presence. The small shift in binding energy, from the reference, for the Ag 3d_{5/2}–Ag 3d_{3/2} doublet is thought to be attributed to material–substrate charge transfer. Figure 3.14C shows the O 1s peak as broad and containing 3 sub peaks within it. The higher binding energy is an X-ray excited Na KLL Auger peak. The two components with binding energies of 531.2 and 532.7 eV correspond to single and double bonded oxygen respectively. This is consistent with the expected presence of a THPO ligand coordinated to the silver surface through the P=O group (seen in figure 1.11).¹⁵⁵ The C 1s peak (Figure 3.14D) shows the main component at 285.0 eV, which is attributed to carbon–carbon bonds in hydrocarbon chains. Weaker peaks are seen with higher binding energies and can be attributed to C–O (286.1 eV), C=O (287.5 eV), and COO– (288.9 eV) functional groups.¹⁵⁶ these account for around 15% of the total carbon percentage ($\approx 27\%$). As these are relatively low levels they are likely to be due to general environmental contamination, typical of samples exposed to a laboratory environment prior to analysis, these can therefore be discounted. A weak phosphorus 2p peak is shown in figure 3.14E. The binding energy of ≈ 133 eV is consistent with the 5–valent phosphorus found in the THPO ligand.¹⁵⁵ Sodium and silicon were also identified in small percentages ($<0.9\%$) which are indicative the, sodium silicate, glass substrate showing through small cracks and pinholes in the silver film. Chlorine present

at low levels may indicate some unreduced THPC from the film formation reaction. Finally, close inspection of the survey spectrum showed low levels of sulfur present (1.1%) with S 2p components at 161.6 eV and 168.7 eV in almost equal portions. The binding energies match to similar data for sulfide and sulfate forms of sulfur.^{157–159} It is known that silver surfaces are highly reactive to environmental sulfur, this presence is attributed to some low level contamination of the silver material. The sulfate component may be an indication of some oxidation of sulfur during the preparation of the films.

3.3 Influence of Annealing on the Morphology of Nanocrystalline Films

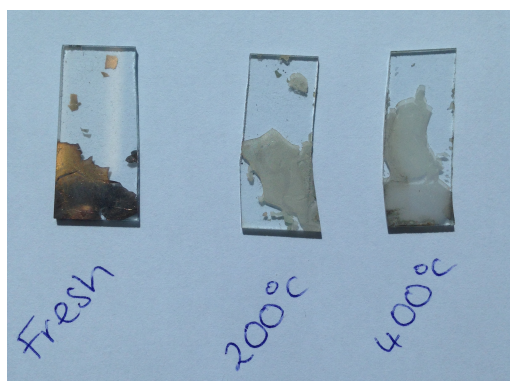


Figure 3.15 – Photograph showing the extent of material loss after annealing (right), compared to a freshly prepared substrate (left). Notice how after annealing the film loses its reflective sheen as material is lost.

To investigate the effects, if any, of annealing nanocrystal films prepared at the interface and deposited on glass, films were analysed using X-ray diffraction (XRD). Annealing of the nanocrystals on the substrate took place in a muffle furnace at temperatures between 100 and 450°C for 3–4 hours, substrates were then left to cool in the furnace until safe to be handled and stored for analysis. Initially analysis was only conducted on pure silver nanocrystal films, due to the low cost of film generation. Using the information from the initial studies gold nanocrystals were then prepared and annealed for diffraction patterns to be collected.

3.3.1 Results and Discussion

Silver nanocrystal films post annealing can be seen in figure 3.15. Of the three glass substrates shown in the photo only the fresh, non-annealed, sample is reflective and lustrous. Heating at elevated temperatures caused the material to begin thinning and lose lustre for the deposited films.

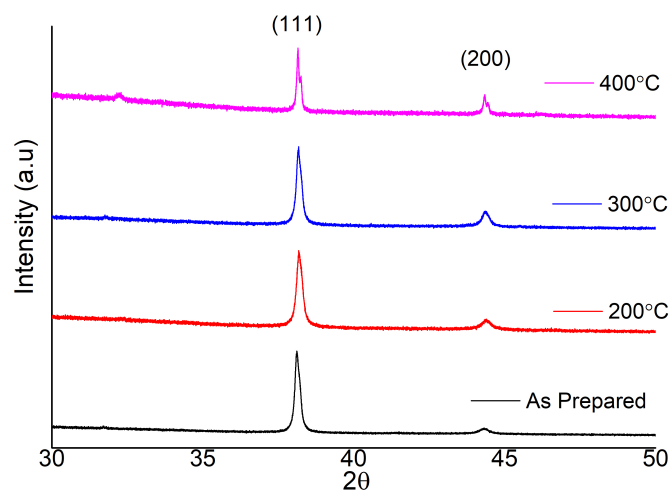


Figure 3.16 – X-ray diffraction of silver films before and after annealing. Films were held at the temperatures shown for 3 hours before being left to cool in the furnace. The data has been stacked for clarity.

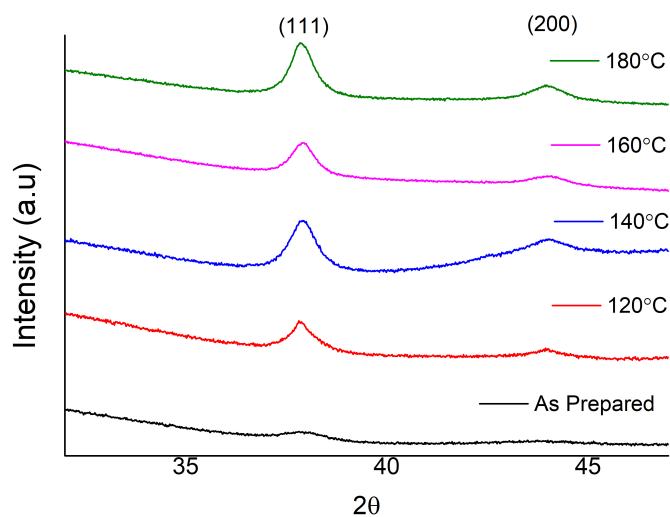


Figure 3.17 – X-ray diffraction of gold films before and after annealing. Films were held at the shown temperatures for 3 hours before being left to cool in the furnace. Data has been stacked for clarity.

XRD patterns are shown, in Figure 3.16, for as prepared silver films and films post annealing at 200, 300 and 400 °C. The XRD patterns clearly shows the (111) peak and (200) peak at $2\theta=38.11$ and $2\theta=44.30$ respectively. Annealing up to 300 °C appears to cause a sharpening of the diffraction peaks, possibly due to some surface ligand removal. Heating to even higher temperatures has caused the two peaks of interest to split as though the unit cell is changing slightly from the bulk. Visual examination of the samples post annealing did show a loss of materials. These observations demonstrate that once deposited onto the substrate the nanocrystals atoms are fixed and do not undergo further rearrangement on annealing. But, elevated temperatures do lead to an evaporation or peeling of the material from the substrate. Further investigation on the annealing of silver nanocrystal films was not undertaken, as the analysis of the XRD was enough to suffice that under the normal conditions and up to reasonable annealing temperatures these films were unchanged.

Based on the results from annealing of silver nanocrystals it was decided to keep the annealing temperatures low and a maximum temperature of 180 °C was chosen to avoid the film evaporation previously seen. Figure 3.17 shows the XRD patterns from a range of annealing temperatures used of deposited gold nanocrystals. As annealing temperatures increased, the diffraction peaks begin to become clearer, possibly due to ligand removal and some rearrangement of the nanocrystals.

3.4 Investigation of Janus Nanocrystals Generated at an Interface

It has been previously reported that nanocrystal growth at the interface of two immiscible liquids generates crystals with two distinct ligand regions (Janus nanocrystals). It is believed that each region will possess only those ligands soluble in the surrounding immiscible liquid.^{146,147} A similar technique takes deposited nanocrystals on glass and submerges them in a solution containing the ligands to be substituted in. When removed from the glass slide only the region of the nanocrystals in direct contact with the liquid have been exchanged, giving two distinct ligand regions.¹⁶⁰ Evidence of which has been demonstrated using Nuclear Overhauser enhancement spectroscopy (NOESY NMR), the two-dimensional NMR technique. In NOESY only short range dipolar couplings are resolved. Therefore, if ligands are randomly assigned as is expected in a single phase method NOESY NMR would show off diagonal interactions.

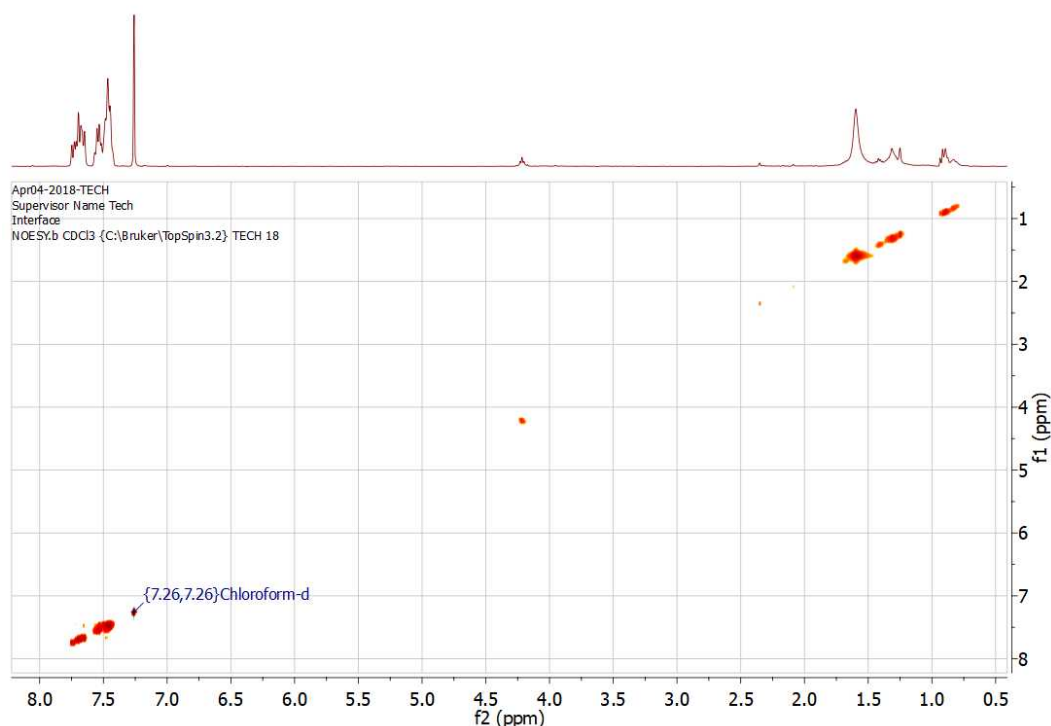


Figure 3.18 – NOESY NMR spectra showing the silver nanocrystals generated at the toluene–water interface. Samples were deposited on glass substrates and later sonicated in d-chloroform to produce a suspension for NMR analysis. The peak at 4.2 ppm is believed to be from trace H₂O/D₂O contamination.

To investigate the phenomenon, silver nanocrystals at the interface of toluene and water were prepared using the method described in chapter 2. The silver nanocrystals formed will, according to the previous works, have both, THPC and PPh₃, fragments as surface ligands. The previous work suggests that the ligands will occupy the nanocrystals surface in two well defined regions.¹⁴⁶ Nanocrystals of silver were also prepared in a single phase methanol/water reaction using hydrolysed THPC and Ag(PPh₃)₃Cl. These nanocrystals should, therefore, possess a random arrangement of the same ligands around the nanocrystal surface as there is no interface to influence the assembly.

3.4.1 Results and Discussion

NOESY NMR studies for the single and two–phase silver nanocrystal methods have been conducted. The silver nanocrystals are demonstrated to have both, THPC and PPh₃, fragments as surface ligands. Figure 3.18 shows the NOESY NMR spectra of silver nanocrystals from the toluene–water interface. The peaks around 7.45–7.80 ppm relate to the PPh₃ protons, the peaks observed about 1.31 ppm and 0.92 ppm is evidence of THPO, a fragment of THPC the strong peak at 1.60 ppm is the H₂O proton. It has been previously suggested that the absence

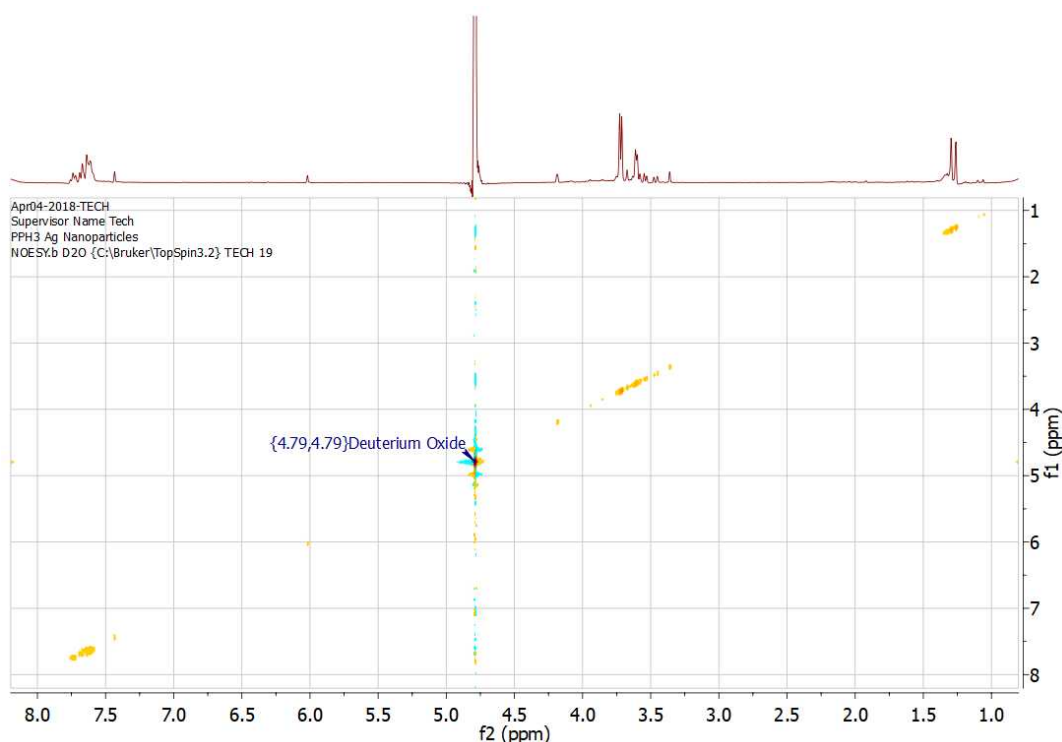


Figure 3.19 – NOESY NMR spectra showing single phase methanol/water generated silver nanocrystals. Nanocrystal suspensions were evaporated to dry and later sonicated in D₂O to create a suspension for NMR analysis.

of off diagonal peaks in the 2D NOESY NMR spectra, as seen here, is evidence of Janus nanocrystals.^{146,147,160}

NOESY NMR studies for a single phase method of preparing silver nanocrystals are shown in figure 3.19. The peaks around 7.50–7.70 ppm relate to the PPh₃ protons, the peaks observed around 3.58–3.70 ppm and 1.28 ppm are all thought to be evidence of the THPC fragments. It is evident when looking at both of the spectra that there is no evidence of off–diagonal cross peaks to be seen in either of the preparation methods. These observations are not consistent with current reported studies and may simply be down to the individual method and particular ligands used, as off–diagonal peaks have been observed in thiol terminated surface ligands.¹⁶⁰ Further future investigation will be required to draw firm conclusions either way with regard to the 2 phase Janus particle at the interface.

3.5 Conclusion

In summary, it has been possible to generate consistent smooth and continuous deposits of nanocrystals at the toluene–water interface. Through combining toluene based precursors, alloys of; AuAg, AuPd and AgPd have been generated. However, attempts to deposit a

pure palladium nanocrystal film in the same method produced an unstable precipitate that broke-up, clumped and settled to the bottom of the reaction beaker. The films possess a structure consisting of large aggregates of nanocrystals. The XRD patterns for pure gold and silver nanocrystals show the broad peaks, characteristic of nanocrystals, which match the reference data. XRD patterns for AuAg and AuPd alloys appear to show a shift in peak position, as expected, following Vegard's law. HRTEM-EDS was able to demonstrate alloy compositions of AuPd matched the initial feed ratios. Producing alloys containing silver and palladium however did not generate the same single phase alloys expected. The XRD patterns and data from HRTEM-EDS eluded to a phase separation containing both silver rich and palladium rich parts of the nanocrystal film. Annealing of nanocrystal films initially caused some rearrangement improving the diffraction reflections. At higher temperatures evaporation causes a thinning of the deposited films.

XPS was able to confirm the expected surface ligands, in conjunction with NOESY NMR investigations. It was however unable, using NOSEY, to confirm or deny if the nanocrystals produced, using the two phase method described here, were Janus particles. Further detailed studies are needed before firm conclusions can be made.

Chapter 4

Charge Transport in Metal and Metal Alloy Nanocrystal Films

4.1 Introduction

Nanocrystallites of inorganic nanocrystals sheathed in organic ligands have been demonstrated as vital ingredients in potential devices such as, electrical and electrochemical sensors, solar cell devices,^{7,8,102} plasmonic devices,^{9,161} data storage elements,⁴ field effect transistors^{10,102,143} and light-emitting diodes.^{3,11,106} Metal nanocrystals are known to possess unique electrical and optical properties due to their reduced dimensions; where the surface area – volume ratio is greater than 1, and dominance of surface plasmons.^{1,3,162–164} Therefore, electrical properties of nanocrystalline arrays differ from the bulk metal.^{3,4,165} Charge transport, in arrays, is primarily dependent on the separation distance between grains^{141,166–168} and diameter of the crystallites.^{169,170} Other factors include the degree of monodispersity in the grain size and structural disorder in films.^{84,168} These concepts were introduced in more detail in Chapter 1.

However, surface ligands can present a strong barrier for the transport of charges through an array. Ligands surrounding nanocrystals will effect the interparticle distance and radius. Ligand exchange reactions have been investigated, replacing ligands with organic and inorganic alternatives. Typical long chain hydrocarbon ligands tend not to offer ideal charge transport, and are often exchanged for shorter more suitable ligands.¹¹⁴ Stansfield *et al.* performed ligand exchanges on films of gold nanocrystals prepared at the interface of toluene and water. Thiophenols with functional groups at the para position were found to tune the conductivity between 100 and $75000\ \Omega^{-1}m^{-1}$.³⁷ Recent interest has been guided towards the smaller inorganic ligands which can promote charge transport in arrays of nanocrystals. Metal chalcogenides,^{10,104,120–122} halometallates,^{123,124} chalcogenide,^{118,125} halides and pseudo-halide ions^{8,124,126–131} (See figure 4.1). Great improvement in room temperature conductivity

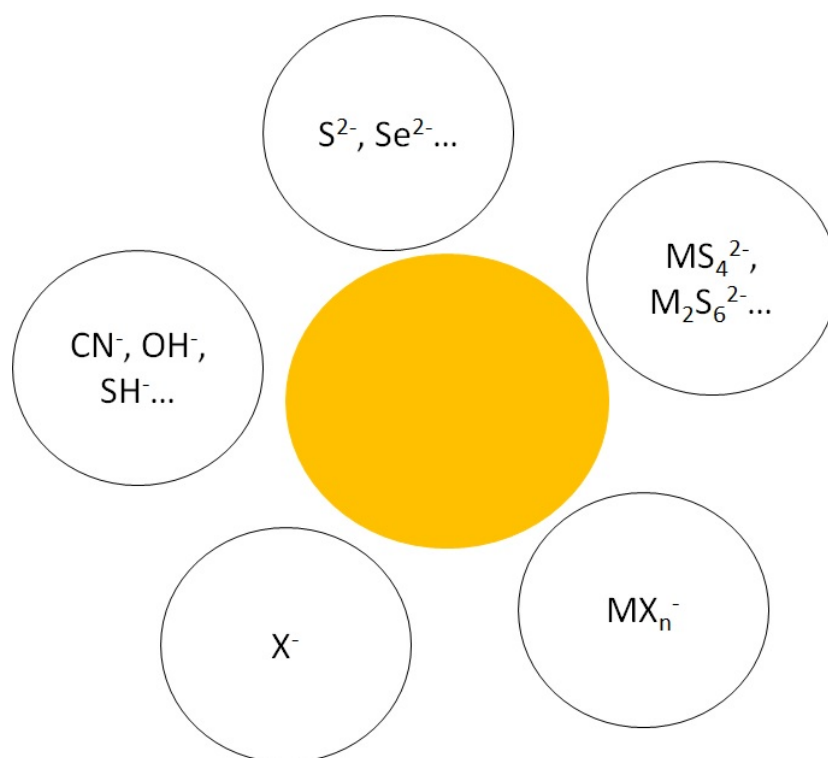


Figure 4.1 – Examples of some inorganic ligands surrounding a nanocrystal. (Top - clockwise) chalcogenide, metal chalcogenide, metal halide, halide and pseudohalide ions

was seen in gold nanocrystals after displacing dodecanethiol ligands with $\text{Sn}_2\text{S}_6^{4-}$.^{120,121} Previously, thin films of metal nanocrystals have been prepared at immiscible interfaces. Initially, films were prepared at the interface through reducing an adduct of AgNO_3 and p-methoxybenzoic acid with aqueous hydrazine, in the presence of stabilizing surfactants.^{38,171} This was later improved upon by Rao and others, reporting synthesis and properties of noble metals and metal chalcogenides at an immiscible interface.^{45,52,62,66,94}

Within this chapter it is shown that the interfacial deposits of Ag, Au and $\text{Ag}_x\text{Au}_{1-x}$ alloy nanocrystals can be obtained at the water–toluene interface. The charge transport characteristics were investigated for these new materials. In chapter 3 annealing was shown to cause a rearrangement within the crystal lattice. It was also believed possible that elevated temperatures caused a thermal ligand removal. The effects of annealing on charge transport are further investigated here, using alloyed nanocrystal arrays.

4.2 Results and Discussion

The temperature dependence on electrical resistance was studied using prepared films of Au, Ag and $\text{Ag}_x\text{Au}_{1-x}$ alloys deposited on glass substrates. Plots showing the charge transport properties of nanocrystalline Au, Ag, and their alloys, are shown in figure 4.2. Pure Ag

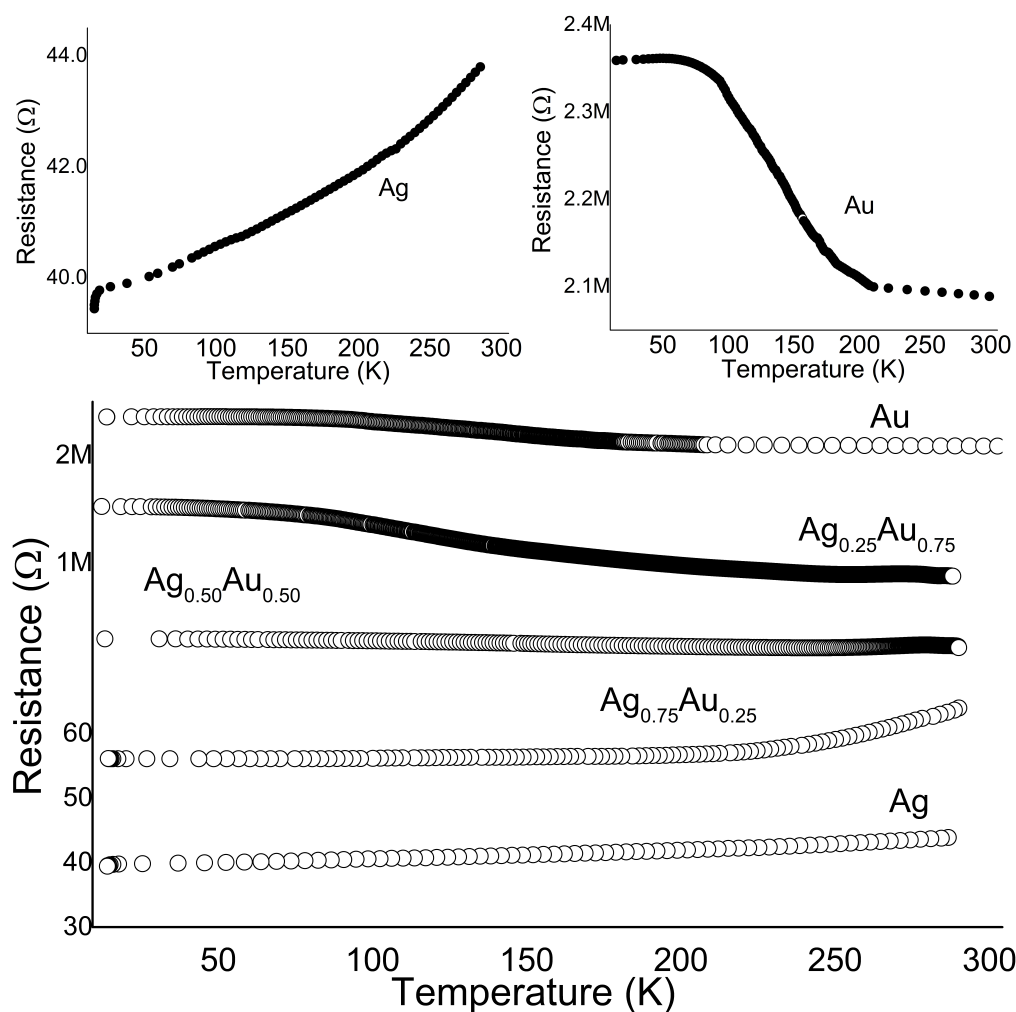


Figure 4.2 – Plots showing temperature dependence of the nanocrystal films resistance for different alloy compositions (labelled). A break has been used from 70 Ω to 100k Ω . The plot in top left shows data for Ag films, where resistance decreases $\approx 10\%$ with decreasing temperatures. The top right shows Au, with resistance increasing from 2.1 M Ω to 2.35 M Ω .

demonstrates a decreasing resistance with temperature, the same behaviour demonstrated in the bulk metal. Lower temperatures result in less vibrations of the nucleus allowing the free, conducting electrons, to pass through the material more easily. Conversely, the pure Au nanocrystalline array results in an increasing resistance with decreasing temperatures. The charge transport becomes more difficult at lower temperatures. Alluding to a conduction method differing from common metallic conduction.

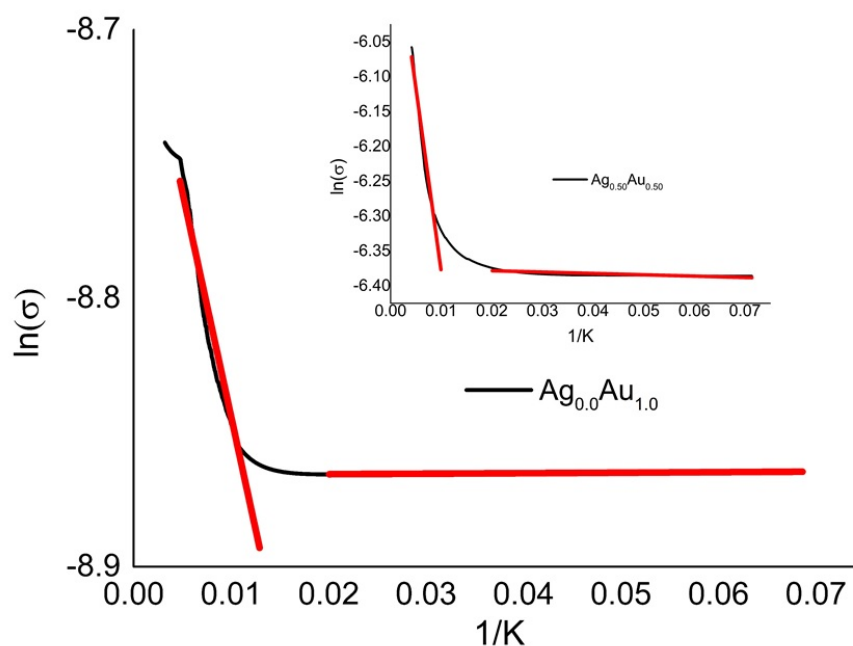


Figure 4.3 – Plot showing the change in natural log of conductivity, $\ln(\sigma)$ against the inverse temperature for a pure Au nanocrystal film. Two distinct linear regimes have been identified in red. Inset shows results from $\text{Ag}_{0.50}\text{Au}_{0.50}$ deposits.

The plotted results for the alloy arrays ($\text{Ag}_x\text{Au}_{1-x}$) move through from the metal-like properties of the Ag to those discovered for the Au, with a transition point around $x \leq 0.4$. Shown on the plot as the change from a positive to negative co-efficient of resistance. Most easily seen when comparing the two pure metal films (figure 4.2 top)

The metallic to non-metallic switch can be brought about by many factors, such as, changes in size, shape, disorder and separation distance of the particulates, highlighted more in chapter 1. Factors effecting the switch include; nanocrystal particulate size, interparticle separation, the shape size and nature of the supporting ligands to name a few. Given the trend seen here with alloy composition, the switch may be attributed to the differing interactions between the particles and ligands. Ag deposits have relatively weak binding to their surface ligands, resulting in physical contact between neighbouring nanocrystals forming conductive pathways, leading to a metallic nature. Much of the measured resistance here is believed to be contact and system resistance. However, Au films possess stronger interactions leading to better defined surface structure and interparticle repulsion. Leading to a collapse of conducting pathways, resulting in a non-metallic or semi-conducting behaviour.

Plots showing the data as natural log of conductance, $\ln(\sigma)$, against inverse temperature, $1/K$, can be used to identify the different regimes for charge transport mechanisms, discussed in chapter 1. Figure 4.3 shows pure Au and the $\text{Ag}_{0.50}\text{Au}_{0.50}$ alloy. Both deposits possess two distinct regimes, with the transition centred around 60 K. The activation energies (E_a) per grain are in the range of a few meV for the high temperature region, and there is a temperature dependence. Hence charge transport appears to be mediated by an activated hopping. At lower temperatures there appears to be no temperature dependence and E_a s fall to $< 0.1\text{ meV}$, demonstrating an electron tunnelling charge transport (see chapter 1). In the case of pure Au, there is another regime observable above 225 K. Multiple domains for activated transport have been observed previously, however the reasons for the observed behaviour remains elusive.³⁷ One possible explanation for multiple domains could be the nature of the supporting ligands, and the point at which they become almost fixed in space due to the reducing kinetic energy. Similar results are seen for the other non-metallic alloys, containing greater than $x \leq 0.4$ Au (figure 4.3 inset).

4.2.1 Charge Transport of Annealed Metal and Metal Alloy Films

Films of pure Au and $\text{Ag}_x\text{Au}_{1-x}$ alloys deposited on glass were annealed at temperatures between 120°C and 180°C before their charge transport characteristics were measured. Annealing is known to allow some rearrangement of the grains. It has been shown in chapter 3 that annealing at temperatures higher than 180°C resulted in severe flaking of the films and evaporation from the glass substrate. Pure silver was not investigated here as it was already found to be metallic in nature. Figure 4.4 shows the charge transport properties of pure Au films after annealing at temperatures 180°C and below. Higher temperatures were not used as they had already been shown to cause an evaporation and severe flaking of the nanocrystal material from the substrate surface. Generally higher annealing temperatures lead to increased resistance. It is believed to be due to thermal removal of the supporting ligands around nanocrystals, breaking down the possible conduction pathways. However, annealing at higher temperatures (up to 180°C) yielded films with drastically lower resistance. Thought to be through a rearrangement, or fusing of the nanoparticulates creating new pathways for the charge to pass through. It should be noted that the maximum annealing temperature used is drastically lower than the metals melting point (1064°C , for bulk gold).

To investigate the unexpected drop in resistance for 180°C gold, resulting in a more conducting material, plots of natural log of conductance, $\ln(\sigma)$, against inverse temperature, $1/K$,

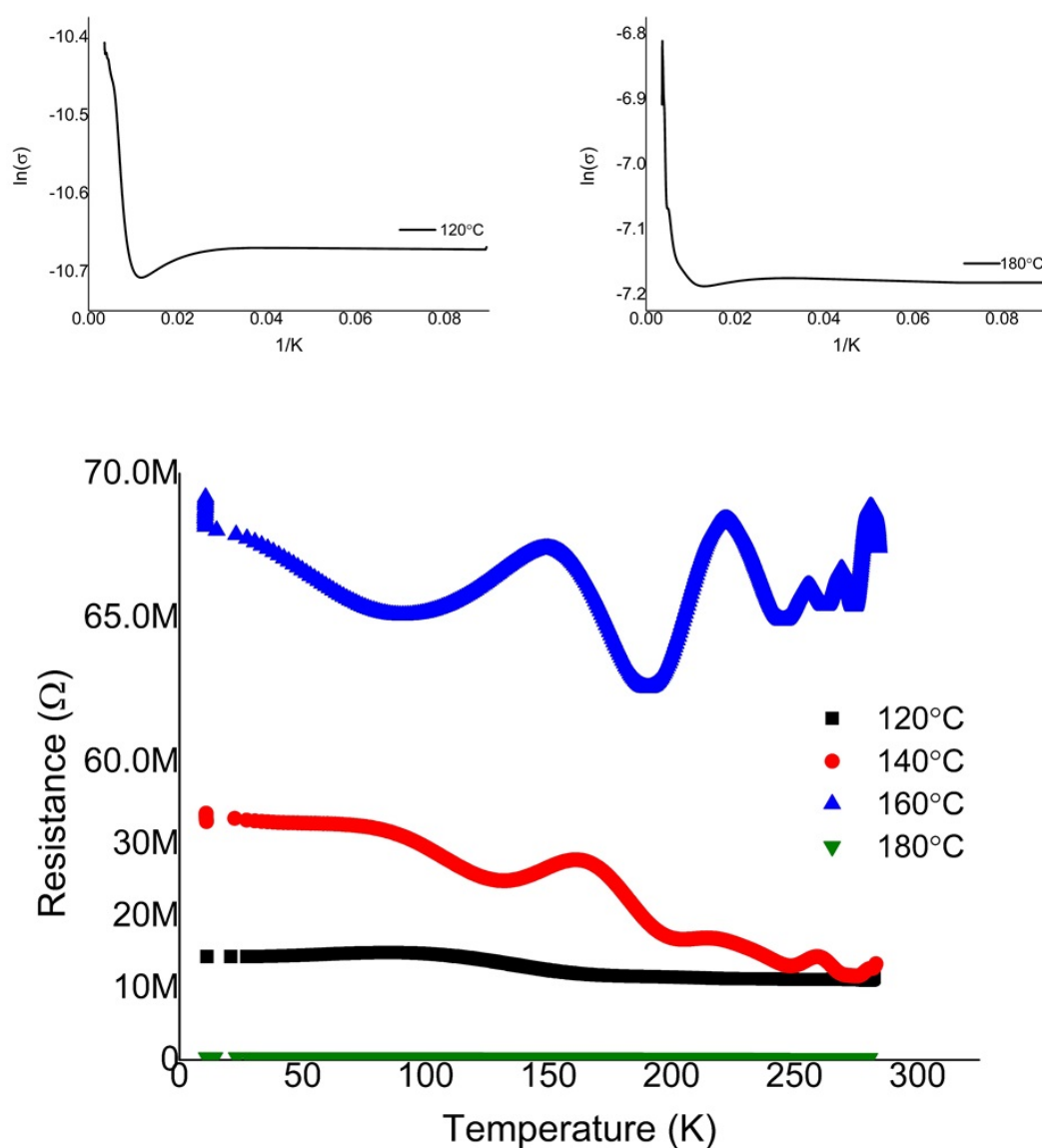


Figure 4.4 – Plots showing temperature dependence of resistance for pure Au deposits annealed at selected temperatures. A break in the Y axis has been used between 40M Ω and 60M Ω . The plots on top show change in natural log of conductivity, $\ln(\sigma)$ against the inverse temperature for a pure gold nanocrystal films annealed at 120°C (Left) and 180°C(Right).

were produced for 120°C and 180°C samples (figure 4.4 top). Both plots show 2 defined mechanisms for charge transport, and their switching point in around the same temperature as found previously, for non-annealed samples. It would appear that the sudden and dramatic drop in resistance, when annealed at 180°C, is not a sign of the array becoming metallic in nature. It is, however, an interesting property, more complex than originally thought, which does require further work and investigation.

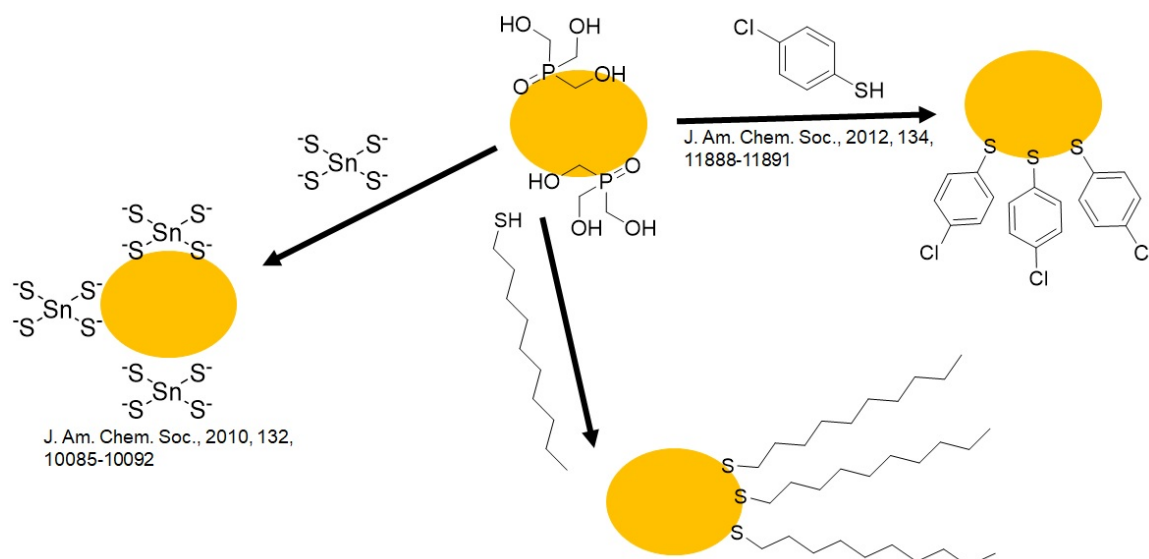


Figure 4.5 – Diagram showing the ligand exchanges used. Top centre shows the supporting ligands expected after the generation of the nanocrystal arrays. Yellow shapes represent the metal nanoparticle with the attached ligands.

4.2.2 Ligand Exchange for Charge Transport Tuning

Ligand exchange has been attempted for pure Ag and pure Au nanocrystal films. For films of Ag, ligand exchange was performed using dilute solutions of 1,10-decanedithiol, 1-dodecanethiol and 3-chlorobenzenethiol prior to any inorganic ligand testing. It is expected that the exchange will work well as the metal–sulfur binding is stronger than the existing ligand bindings. 1,10-decanedithiol has two possible binding points through the terminal thiol functional groups, whereas both 1-dodecanethiol and 3-chlorobenzenethiol have single binding points through their thiol group (figure 4.5).

Freshly prepared deposits on glass substrates were submerged in the solutions and left to exchange for 24–48 hours in a fridge. On removal films were gently washed to remove and non-adhered ligands. Figure 4.6 shows the charge transport properties of ligand exchanged Ag films. The exchanged ligands are shown to have no effect on the resistance properties of the Ag. Adding further evidence to the belief that when Ag deposits form at the interface there is contact between the nanocrystals, removing the requirement of ligands for charges to pass through. There is a drop of a few ohms of resistance when compared to the Ag prepared and tested in figure 4.2, believed to be from replacing the contact wires within the instrument changing the systems contact resistance whilst not affecting the film properties.

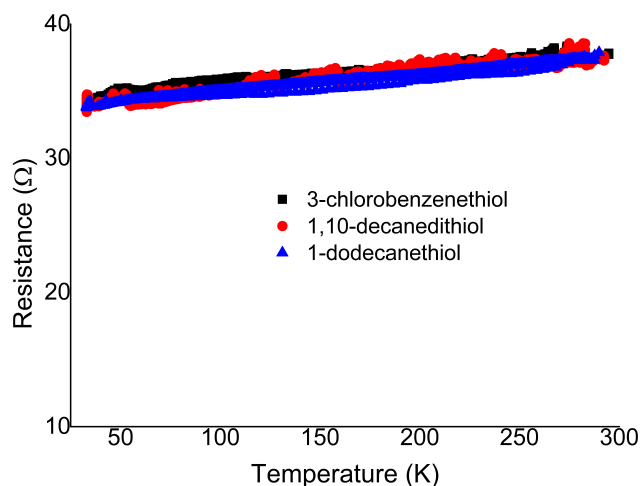


Figure 4.6 – Plot of resistance against temperature for various Ag films after ligand exchange. The resistance drops with temperature as is expected for a metal conductor.

Au films were deposited on glass substrates and the ligands replaced in an inorganic ligand exchange. Saturated solutions of $\text{Na}_2\text{S}_x\text{H}_2\text{O}$ in water and methanol were prepared to generate S^{2-} and SO_x ligands respectively. Previous studies had shown these to ligand exchange when used with CdS and Au nanocrystals.¹¹⁸ Na_4SnS_4 has been identified as a possible small inorganic ligand for use in nanocrystals. To investigate, the Na_4SnS_4 ligand was synthesised (see chapter 2 for synthesis) and used as an aqueous solution in ligand exchanges with Au.¹⁰⁴

Figure 4.7 shows charge transport properties of Au films after the ligand exchange. It is interesting to see that the S^{2-} and Na_2SnS_4 both had the effect of lowering electrical resistance whilst a ligand exchange to SO_x went on to dramatically increase the film resistance. The overall trend for all three ligands is for a resistance increase as temperature decreases, the same as reported previously. The behaviour is akin to semi-conductors and is typical of films consisting of metal nanocrystals interspersed by organic long chained ligands.^{37,75} Two of the inorganic ligands shown here have the ability to tune resistance by a significant factor of, up to, 1 MΩ. However, the resulting materials are still non-metallic in their conducting properties.

4.3 Conclusion

In this chapter it has been shown that the thin films of metal nanocrystals with phosphinyl surface ligands generated previously could be utilised for charge transport. Ligand exchange

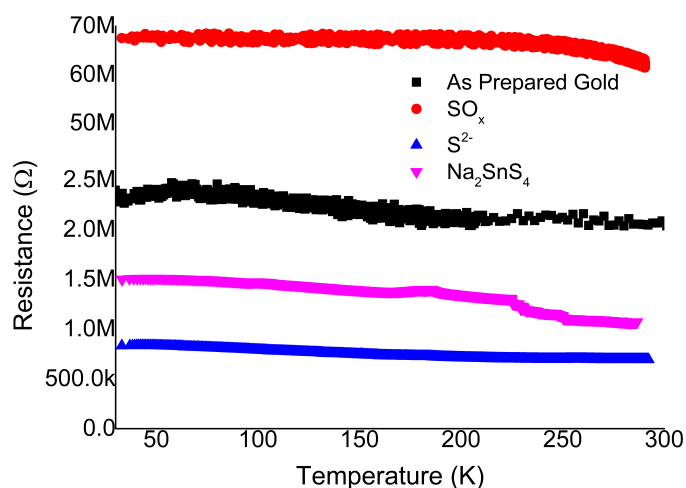


Figure 4.7 – Plot of resistance against temperature for as prepared Au films and Au films with exchanged ligands. A break has been used between 3M Ω and 50M Ω.

could be used to swap in more desirable ligands through a simple post deposition soaking method.

Ag films were found to have a resistance in the order of a few Ωs and conduct as though they were a bulk material. Much of the measured resistance is contact and system resistance caused by the wires and contacts used. It is possible to remove the effects of contact resistance through the use of a 4 probe measuring method, bringing the overall resistance down dramatically. However, we did not have access to these types of measurement during the experiments. Ligand exchanges performed on Ag deposits did nothing to alter the conducting properties, giving rise to the theory that the nanocrystal particulates are likely to be in such an arrangement within the deposits that they are touching, or so close as to provide a very easy low resistance route for conduction.

Au film deposits possessed conductivities akin to semi-conductors, as is common in nano-sized Au, with resistance measured in the range of MΩ. There were two defined regions for the conducting mechanism with a change over at around 60 K. At higher temperatures charge transport is dominated by some form of activated hopping, below 60 K charge transport is independent of temperature and more likely tunnelling transport dominates.

The preparation of alloyed deposits of Au and Ag films produced a tunable resistance range over 2.4 MΩs. There was a non-metallic to metallic transition when compositions contained

more than $\approx 40\%$ Ag. The non-metallic films, less than $\approx 40\%$ Ag, appeared to have the same two mechanisms for charge transport and the same transition between temperature dependence and non-temperature dependence as found with the pure Au films.

When annealing alloyed $\text{Ag}_x\text{Au}_{1-x}$ films at temperatures below 180°C an increase in film resistance was observed, believed to be caused by the thermal decomposition of surface ligands. However, at more elevated temperatures surprisingly the resistance dropped, possibly through some thermal rearrangement of nanoparticulates on the substrate surface. The phenomenon does require retesting and further more in-depth investigation.

The charge transport was shown to be highly selective to a number of factors including alloy content, supporting ligand, and annealing. The charge transport relationship appears complex and more studies are required to fully unravel and understand. The synthetic scheme used here is suitably apt for creating further materials for these types of studies, as the method is simple and creates deposits with reproducible character.

Chapter 5

Nanocrystal Metals and Metal Alloys as Nanocatalysts

5.1 Introduction

One goal of the chemical industry is to reduce the production costs and keep the environmental impact low, whilst still obtaining high-quality products. Catalytic membranes are a viable solution, as they have the ability to improve yield whilst decreasing the costs and ease of separation. Membranes can be easily recycled multiple times, saving both time and money.¹⁷² Membrane supported catalysts have been developed using both organic and inorganic materials, depending on the reaction conditions needed. Supports can play an active or passive part in the catalysis process. They can help to enable catalysis in a medium which the catalyst does not dissolve. They can also play a synergistic role promoting activity of the catalyst.^{25,172,173} Inorganic catalyst materials, such as metals and ceramics, are able to perform at much higher temperatures than organic polymer catalysts.¹⁷² Cellulose, one of the most abundant biopolymers on the planet, has been used previously to produce cheap and environmentally sustainable supports for metal nanocatalysts.^{25,173}

Zhang *et al.* produced Pd nanocrystals embedded into magnetic supports. These supported nanocatalysts were shown to catalyse the reduction of 4-nitrophenol and nitrobenzene in the presence of NaBH₄, demonstrating improved activity over corresponding reference samples.¹⁷⁴ The magnetic properties of the supports allowed for quick and easy separation from the solution. These separated nanocatalysts were recycled up to 4 times without obvious loss of activity. Other nanocrystalline metals including; Pt, Ru, Rh and Au have also been utilised in magnetically recoverable nanocatalysts for reactions.^{26,28,29}

The hydrogenation of alkenes is an important reaction in petrochemical and fine chemical synthesis.¹⁷⁵ Palladium tends to be a desirable catalyst for these reactions due to its mild

reaction conditions, high activity and selectivity.^{176–178} However, the cost of palladium is high and methods to reduce the costs associated are needed.

Lin *et al.* developed phosphor-doped graphitic carbon nitride via a facile calcination technique to be used as the support for a heterogeneous palladium catalyst. The optimised catalyst was used for the hydrogenation of styrene, where it was shown to exhibit an excellent catalytic activity of $856.89 \text{ mmol}_{\text{Styrene}}/\text{min}/\text{g}_{\text{Pd}}$ along with a high TOF value of $18,974 \text{ h}^{-1}$.¹⁷⁶

Yamada *et al.* was able to reproducibly prepare silicon nanowire array and palladium nanoparticle hybrids for use as hydrogenation catalysts.¹⁷⁸ The system was tested for the hydrogenation of a variety of alkenes, including tetra-substituted olefins. These were readily converted to alkanes in high yield by fresh and recycled catalyst. It was found that the catalysts could be used more than one hundred times without the loss of activity. In contrast to carbon supported palladium catalysts which decrease during its reuse, affording much lower catalytic activity.¹⁷⁸

In the following chapter the nanocrystals produced using the methods described in chapter 2 are investigated for their catalytic properties. The as generated films were collected on Whatman™ PTFE membrane circle, by suction filtration, dried in air and used as heterogeneous catalysts for the reduction reactions of 4-nitrophenol and nitrobenzene and for the hydrogenation reaction of cyclohexene. Catalysts were deposited on supports to increase the ease of separation and allow for multiple recycling reactions without loss of material. By using alloys containing Pd it is hoped that the reactions are still able to occur. Reducing the amount of Pd required in each reaction has the potential create large cost savings.

5.2 Nanocatalysed Reduction Reactions

Nitroaromatic compounds are starting materials for the production of large quantities of aromatic amines. The 4-nitrophenol reduction by sodium borohydride in the presence of Ag catalysts is now accepted as an alternative effective and eco-friendly route to produce 4-aminophenol.^{181,182} In recent years, the reaction has become a model for evaluating the performance of a reduction catalyst, due to its simplicity.¹⁷⁹ In neutral or acidic aqueous solution 4-nitrophenol exhibits a light straw colour and shows a strong absorption peak at 317 nm (Figure 5.2). With the addition of sodium borohydride 4-nitrophenolate ions are formed resulting in a red-shift of the absorption band to 400 nm, accompanied by a

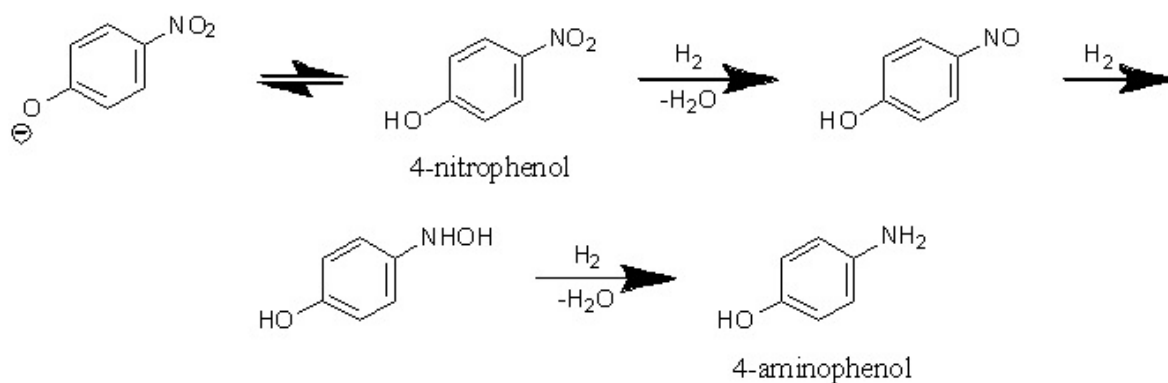


Figure 5.1 – Proposed mechanism for the reduction of 4-nitrophenol to 4-aminophenol on the surface of metallic nanocrystals.^{179,180}

colour change to yellow–green.¹⁸¹ In the presence of a catalyst the sodium borohydride is able to reduce 4-nitrophenolate to 4-aminophenol. The latter possesses a peak at 295 nm. As a function of time the decrease of the 4-nitrophenolate peak and the increase of the 4-aminophenol peak can be tracked easily by UV/Vis spectroscopy. The suggested reaction route for the 4-nitrophenol reduction is shown in figure 5.1. The hydroxyl–group of 4-nitrophenol may exist as protonated or deprotonated dependent on the pH–value. In the first step 4-nitrophenol is reduced to nitrosophenol, which reacts quickly to 4-hydroxylaminophenol. The product 4-aminophenol is formed after another (rate determining) reduction step. In detail the reduction is performed via an electron transfer from borohydride to the catalyst. The transfer results in a hydrogen atom, which can then reduce the 4-nitrophenol. Both reactants, 4-nitrophenol and sodium borohydride need to be absorbed onto the catalyst surface for the reaction to proceed.^{179,180}

The reduction of nitrobenzene (figure 5.3) is one of the most important conversions in synthetic organic chemistry since the anilines obtained are commercially important starting materials and intermediates for many valuable compounds such as pharmaceuticals, agrochemicals, and dyes.^{183,184} The reaction is relatively mild and can be catalysed by many metals. For this reason it is often employed as a reference reduction reaction for testing activities of potential catalysts.^{185–189} Typically, such a reaction does not occur in the absence of a catalyst due to the enormous potential difference between the hydrogen donor (sodium borohydride) and the acceptor (nitrobenzene) which leads to a kinetic barrier.^{184,190} The widely accepted mechanism for the reaction, proposed by F. Haber in 1898, is shown in figure 5.4. Whereby

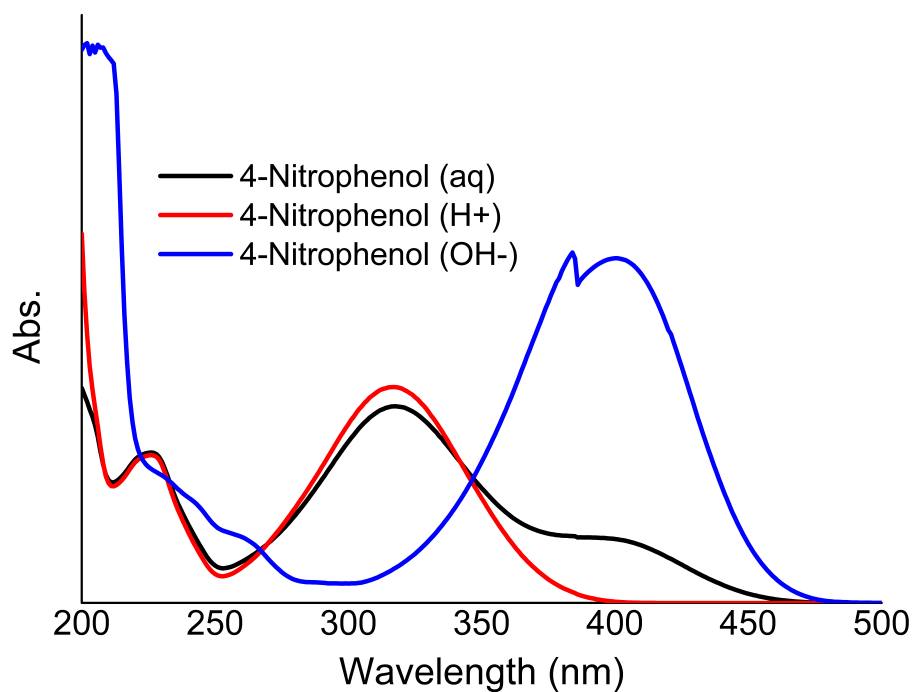


Figure 5.2 – 4-Nitrophenol in aqueous, basic and acid conditions showing how the UV/Vis profile changes as the -OH group interacts in the conditions.

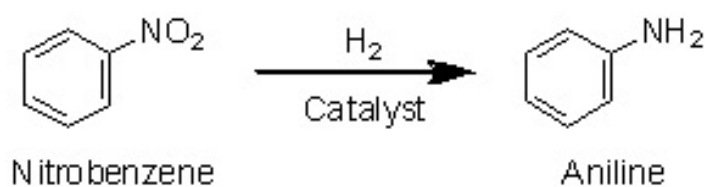


Figure 5.3 – Simple schematic reaction equation for the catalysed reduction of nitrobenzene to aniline.

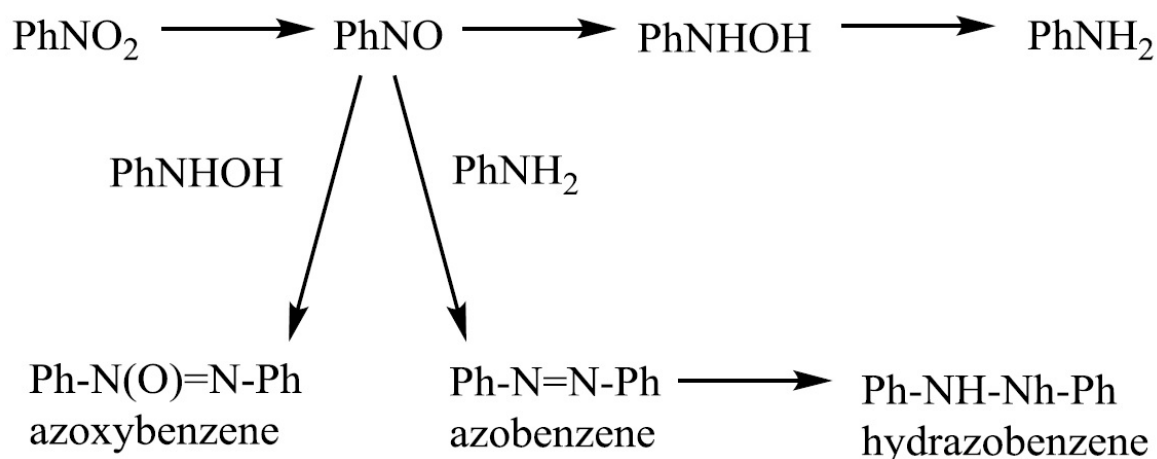


Figure 5.4 – The Haber mechanism for nitrobenzene reduction to aniline, originally proposed in 1898.^{183,191}

nitrobenzene reacts to aniline passing through the two intermediates, nitrosobenzene and phenylhydroxylamine. Furthermore, by-products such as azoxybenzene, azobenzene and hydrazobenzene could be formed.^{183,191}

Of the two reactions chosen for reduction modeling the 4-nitrophenol is the easier to reduce due to the hydroxide group acting as an activating group, directed to the ortho- and para- ring positions. The nitro group is an electron withdrawing group which reinforces the activation on the para- position. Nitrobenzene lacks a similar activated ring making the reduction more challenging.

To assess the catalytic activity of noble metal and metal alloy nanocrystal deposits at the water–oil interface the aqueous reductions of 4-nitrophenol and nitrobenzene in the presence of sodium borohydride are investigated and monitored through UV/Vis spectroscopy.

5.2.1 Results and Discussion

4-Nitrophenol

Ag, Ag_{0.5}Au_{0.5}, Au_{0.5}Pd_{0.5} and Ag_{0.5}Pd_{0.5} nanocatalysts were tested using the model 4-nitrophenol reduction, described above, using the method described in chapter 2. 4-nitrophenol and sodium borohydride were combined in a quartz UV cuvette before the nanocatalyst was added down the side, so as not to obscure the light beam. Figure 5.5 shows absorption spectra results for a, fresh unused, Ag film deposited on a Whatman™ PTFE membrane. We see that over the course of 30 minutes, the λ_{max} at 400 nm corresponding to 4-nitrophenolate decreases in intensity by 35% while the peak at 295 nm due to 4-aminophenol increases slightly. The

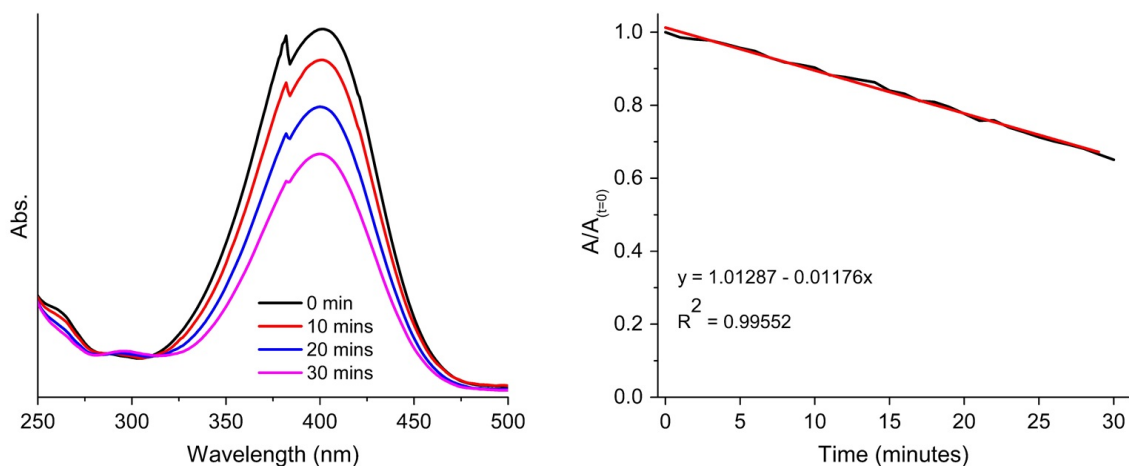


Figure 5.5 – (LEFT) UV/Vis absorption spectra for a solution of 4-nitrophenol with sodium borohydride in the presence of a Ag film deposited on Whatman™ PTFE membrane. Abs. are arbitrary units of absorption and time indicates minutes since addition of sodium borohydride. (RIGHT) $A/A_{t=0}$ against time. Where A is absorption at time and $A_{t=0}$ is initial absorption, before addition of sodium borohydride.

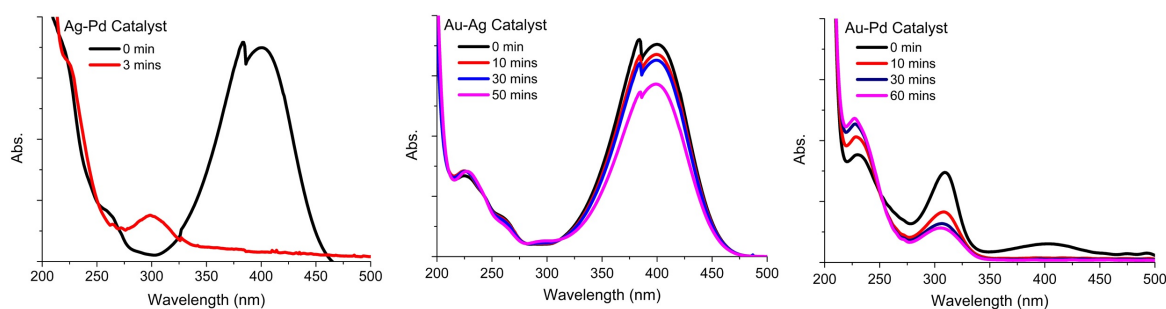


Figure 5.6 – UV/Vis absorption spectra for a solution of 4-nitrophenol with sodium borohydride in the presence of $\text{Ag}_{0.5}\text{Pd}_{0.5}$ (Left), $\text{Au}_{0.5}\text{Ag}_{0.5}$ (Middle) and $\text{Ag}_{0.5}\text{Pd}_{0.5}$ (Right) alloy films deposited on Whatman™ PTFE membrane. Abs. are arbitrary units of absorption and time indicates minutes since addition of sodium borohydride.

inset plot of $A/A_{t=0}$ against time shows the ratio between the UV/Vis absorbance at each time point and the initial absorbance at $t=0$. The steeper the gradient of the graph the faster the loss of 4-nitrophenolate. The Ag nanocatalyst shows a relatively slow rate of reduction for the 4-nitrophenol reaction. When in the presence of water sodium borohydride decomposes to hydrogen gas and sodium metaborate. Therefore, all reactions were monitored for only 60 minutes, as the sodium borohydride begins to lose much of its activity over longer periods.

Data from $\text{Ag}_{0.5}\text{Au}_{0.5}$, $\text{Au}_{0.5}\text{Pd}_{0.5}$ and $\text{Ag}_{0.5}\text{Pd}_{0.5}$ nanocatalysts for the reduction of 4-nitrophenol can be seen in figure 5.6. All 3 alloys are seen to cause a measurable loss of the 4-nitrophenol molecule compared to a control. Demonstrating that it is possible to catalyse the reduction of

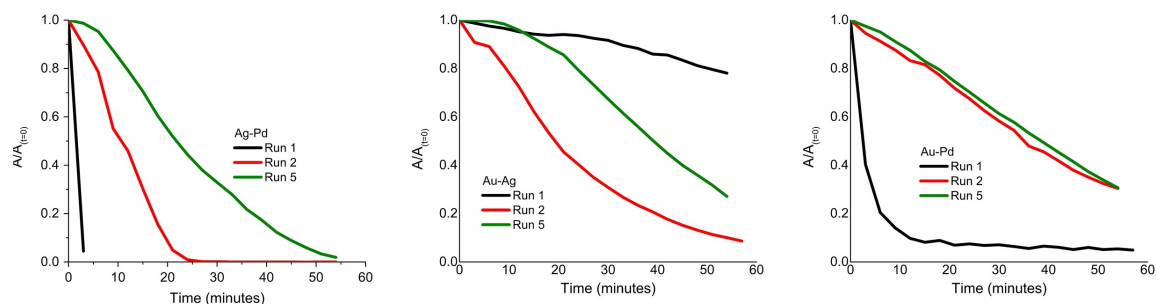


Figure 5.7 – Plots of $A/A_{t=0}$ against time for $\text{Ag}_{0.5}\text{Pd}_{0.5}$ (Left), $\text{Au}_{0.5}\text{Ag}_{0.5}$ (Middle) and $\text{Ag}_{0.5}\text{Pd}_{0.5}$ (Right) nanocatalysts performance for multiple reactions recycling the original supported catalyst. Data has been shown for the initial, second and fifth cycle. Where A is absorbance at time and $A_{t=0}$ is initial absorbance, before addition of sodium borohydride. Between each use the nanocatalyst was washed gently with water to remove any loosely adhered reactants.

4-nitrophenol at varying rates depending on the catalyst composition. Catalysts containing palladium do lead to faster reduction rates. For example, $\text{Ag}_{0.5}\text{Pd}_{0.5}$ nanocatalyst reports a $\approx 90\%$ loss of 4-nitrophenol within 3 minutes. However, Ag and $\text{Ag}_{0.5}\text{Au}_{0.5}$ supported catalysts are still suitable lower cost alternatives. Given that there is some uncertainty in the method of preparing the supported nanocatalysts. In that, the loading of material on to the support is unknown. Some supports may therefore contain more nanocatalyst material than others. The reliability of rate change comparison for the first run of the nanocatalysts could be called into question. However each support was prepared in the same way and cut to the same size in the hope of reducing the issue.

The plot showing a $\text{Au}_{0.5}\text{Pd}_{0.5}$ catalysed reduction shows a different UV/Vis profile. It appears that when in contact with the particular catalyst 4-nitrophenol behaves as if it were in acidic conditions (see figure 5.2) pushing the λ_{max} to ≈ 317 nm. A λ_{max} of ≈ 317 nm was only observed for the $\text{Au}_{0.5}\text{Pd}_{0.5}$ investigation when using a virgin catalyst. When recycling the nanocatalyst the acidic form is no longer detected, reverting back to the neutral form of 4-nitrophenol. It is possible that there is some initial binding, or interaction between the catalyst surface and reactant before the addition of the sodium borohydride.

The nanocatalysts are supported on Whatman™ PTFE membrane circles to promote easy separation from the reaction liquor and recycling. Membranes were gently washed with distilled water, to remove any loosely adhered reactants and products, and recycled multiple times.

$A/A_{t=0}$ plots for the nanocatalyst recycling is shown in figure 5.7. Nanocatalysts were recycled up to five times to investigate any changes in their performance. Generally, the rate drops, as expected, when compared to the initial virgin catalysts. Likely caused by some loss of material on washing and also some blocking of active sites by products not fully desorbing. However, the activity caused by the composition is preserved on recycling. The catalyst with the highest rate still has the higher rates on recycling. The same trend was seen during repeats using and recycling a fresh supported catalyst.

Nitrobenzene

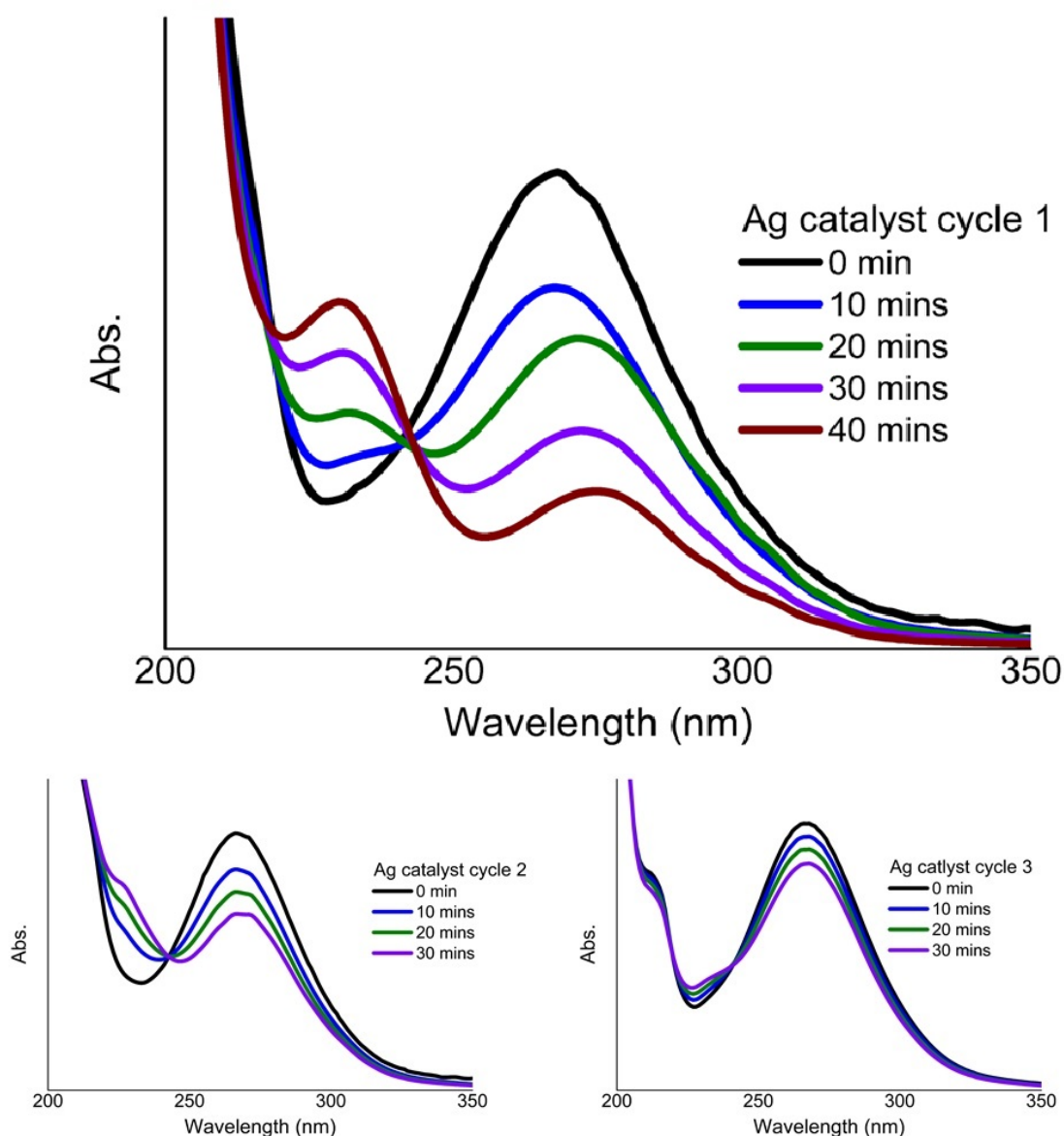


Figure 5.8 – UV/Vis absorption spectra for a solution of nitrobenzene with sodium borohydride in the presence of a Ag film deposited on Whatman™ PTFE membrane (Top). The catalyst was removed washed and recycled twice after the initial cycle. UV/Vis absorption spectra for recycling shows some retained reduction activity (Bottom). Abs. are arbitrary units of absorption and time indicates minutes since addition of sodium borohydride.

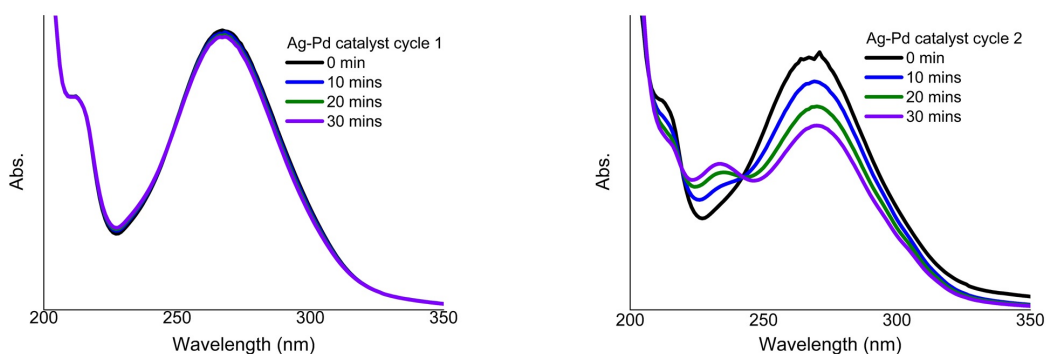


Figure 5.9 – UV/Vis absorption spectra for a solution of nitrobenzene with sodium borohydride in the presence of a virgin $\text{Ag}_{0.5}\text{Pd}_{0.5}$ film deposited on Whatman™ PTFE membrane (Left). The catalyst was removed washed and recycled after the initial cycle (Right). Abs. are arbitrary units of absorption and time indicates minutes since addition of sodium borohydride.

Ag and $\text{Ag}_{0.5}\text{Pd}_{0.5}$ supported nanocatalysts were also investigated as possible catalysts for the reduction of nitrobenzene to aniline, described above. Nitrobenzene and sodium borohydride were combined in a quartz UV cuvette before the nanocatalyst was added down the side, so as not to obscure the light beam (see chapter 2). Figure 5.8 shows the UV/Vis spectra for cycle 1, 2 and 3 for Ag nanocatalysed reductions of nitrobenzene in the presence of sodium borohydride. Performance of the catalyst is reduced with each repeat cycle. On the third use of the Ag nanocatalyst 30 minutes reaction time leads to nitrobenzene intensity reducing by almost 22%, compared to 60% for a virgin nanocatalyst. There are very few reported examples of pure Ag nanocatalysed reduction of nitrobenzene under benign room-temperature conditions. Previous examples incorporate Ag nanocrystals as part of a complex or organic framework.^{184,192}

UV/Vis absorption spectra for the supported $\text{Ag}_{0.5}\text{Pd}_{0.5}$ alloy nanocatalyst is shown in Figure 5.9. Cycle 1 shows no reduction in the absorption intensity, meaning there is very little or no reduction of the nitrobenzene. The inactivity was unexpected, as the Ag nanocatalyst did perform reasonably for nitrobenzene reduction and the same alloy composition was also successful in the reduction of 4-nitrophenol. However, after removal and gentle washing the nanocatalyst is shown to have become active and successfully reduces the nitrobenzene to aniline. Over the 30 minutes reaction the intensity of absorption for nitrobenzene reduced by 18%. Less than expected, when compared to a Pd free Ag nanocatalyst. It was anticipated that the Pd would increase the reduction rate as Pd is preferred by conventional wisdom for these types of reactions. The difference could be linked with the initial cycle not causing any

reduction to occur. If the nanocatalyst had become inactive due to dirt, or a missed step in the cleaning when depositing, the washing step between cycles may not have removed all contamination. Leaving only a small amount of the surface open for reducing. Further cycles were not investigated as the reduction rate was expected to worsen with each new cycle, as previous results showed.

5.3 Nanocatalysed Hydrogenation of Cyclohexene

It is possible to perform catalysed reductions of alkenes to alkanes in methods not involving H_2 gas.¹⁹³ However for the current study reactions were performed in a sealed pressure vessel under a high H_2 atmosphere to reduce other possible side and secondary reactions which may occur using other H_2 sources. The method chosen provided a more easily repeatable system, where the pressure and temperature could be controlled.

5.3.1 Results and Discussion

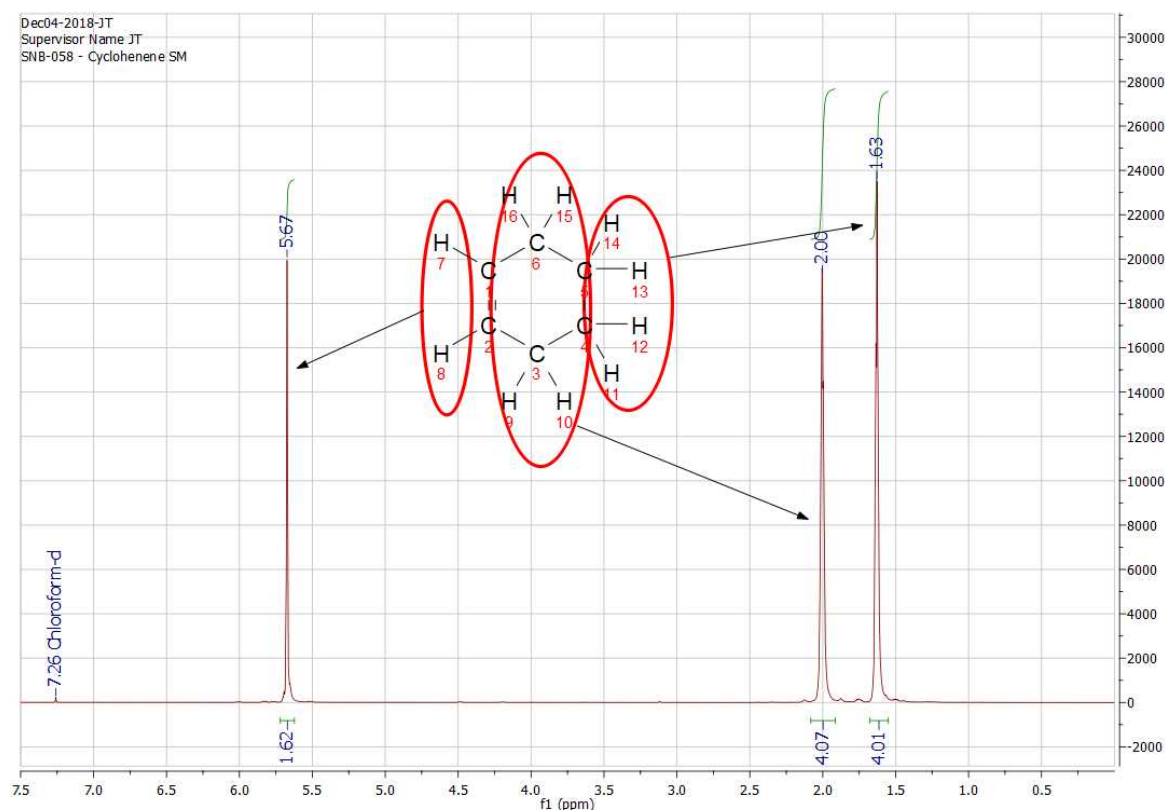


Figure 5.10 – Proton NMR of cyclohexene in $CDCl_3$. Peaks have been assigned and identified on the inset molecule.

Cyclohexene was chosen as the subject for hydrogenation and chloroform as a solvent for the ease of monitoring. NMR peaks for the starting material and expected product, cyclohexane, would not interfere and would be easily interpreted from a crude NMR carried out in deuterated chloroform. Figure 5.10 shows the NMR spectrum of cyclohexene. The three

peaks can be easily assigned. The peak at 1.63 ppm relates to four hydrogens labelled 11, 12, 13 and 14. The peak at 2.00 ppm relates to the four hydrogens labelled 9, 10, 15 and 16. Finally the peak at 5.69 ppm is the two hydrogens over the double bond, labelled 7 and 8. Cyclohexane is a symmetric molecule and will possess only one peak which is expected at 1.43 ppm.^{194,195}

Prior to using the nanocatalyst materials and to ascertain that any hydrogenation identified was being performed due to the addition of the catalysts a blank reaction was initially performed. Figure S1 shows the NMR spectra after 5 hours heating and stirring under a hydrogen rich atmosphere. The spectra matches that of pure cyclohexene, as expected. Therefore, the reaction conditions alone do not cause hydrogenation to take place.

The reaction was then performed three further times with the addition of a nanocatalyst, $\text{Ag}_{0.5}\text{Au}_{0.5}$, $\text{Au}_{0.5}\text{Pd}_{0.5}$ or $\text{Ag}_{0.5}\text{Pd}_{0.5}$ on Whatman™ PTFE membrane circle supports. The crude experiment was designed to see if there was any generation of cyclohexane from the reduction of cyclohexene when catalysed by these novel nanocatalysts. The NMR spectra of the crude reaction liquor from each experiment can be seen in figures S2, 5.11 and S3. Figures 5.11 and S3 show a new peak at 1.43 ppm, attributed to the generation of cyclohexane from cyclohexene. There is however no evidence of the generation of cyclohexane in the reaction employing a $\text{Ag}_{0.5}\text{Au}_{0.5}$ nanocatalyst (figure S2). The evidence would suggest that for the hydrogenation to proceed palladium must be present in the catalyst. However our initial investigation does not answer how much or how little Pd must be present.

5.4 Conclusions

In the chapter, nanocrystal films and their alloys prepared and characterised in chapter 3 have been deposited on to Whatman™ PTFE membrane circles for testing as nanocatalysts in the reduction reactions, of 4-nitrophenol, nitrobenzene, and the hydrogenation reaction of cyclohexene.

4-nitrophenol and nitrobenzene were both successfully reduced through the use of thin film nanocatalysts in the presence of sodium borohydride. Those catalysts containing Pd demonstrated faster reduction rates overall compared to those without Pd. The rates of reduction are important as the sodium borohydride decomposes readily in the aqueous solution and halts the reaction. Recycling of the nanocatalysts for multiple reactions did show a drop

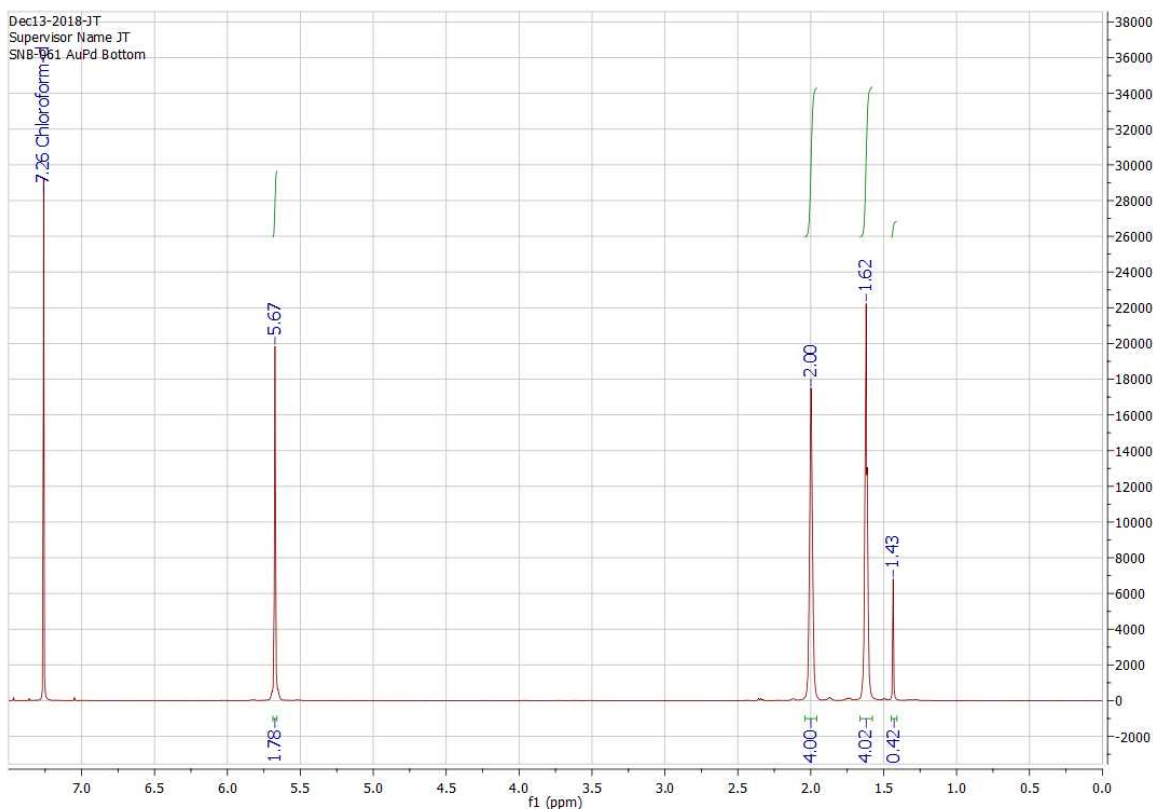


Figure 5.11 – Proton NMR of crude reaction liqueur in CDCl_3 after heating for 5 hours under H_2 atmosphere in the presence of a $\text{Au}_{0.5}\text{Pd}_{0.5}$ nanocatalyst supported on Whatman™ PTFE membrane circle. A small new peak at 1.43 ppm can be seen, relating to cyclohexane.

in performance from the initial use, as is expected, due possibly to some material being lost on washing and possible catalyst poisoning. The density of catalyst on supports may vary slightly between each prepared support, but, the alloy composition will not. However, repeating the reduction and recycling of fresh catalysts provided similar results. Catalyst recycling will allow greater quantities of the amine products to be generated increasing the yield per gram for each nanocatalyst material.

The three alloy nanocatalysts, $\text{Ag}_{0.5}\text{Au}_{0.5}$, $\text{Au}_{0.5}\text{Pd}_{0.5}$ or $\text{Ag}_{0.5}\text{Pd}_{0.5}$, were tested for their activity as possible hydrogenation catalysts for cyclohexene. Using NMR of the crude reaction mixture it was noted that only the catalysts containing Pd showed evidence of generating cyclohexane during the reaction. All of the alloys used for the investigation were generated as 1:1 ratios. As an initial testing of the nanocatalysts, it was believe that these ratios would give an good indication with simple testing and be able to lead in to further research. Future work is now required to investigate varying the alloy ratios to determin

the lowest ratio of Pd required for a viable reaction. Through decreasing the Pd content the overall costs will be reduced for producing the desired products.

Chapter 6

Using Silver Nanocrystal Films as Antibacterial Coatings

6.1 Introduction

It is well known that silver nanocrystals (AgNCs) have antimicrobial and antifungal uses, due to their favourable chemical and physical characteristics.^{196–198} There are varied methods for the synthesis of AgNCs, including scalable solution based methods, making AgNCs cost effective.^{199–208} Due to the ease of generation, alloying and functionalisation of the AgNCs they are of particular interest in medical and food industries. Bacteria have the ability to adhere to and form biofilms on many different surfaces, making them potentially dangerous contaminants.²⁰⁹ Within medicine, bacterial biofilms can lead to conditions from short term illnesses, serious long term illnesses and even death. Excessive build-up of bacteria in the food industry can lead to spoilage and an increase in food wastage, leading to increased cost to manufacturers and in turn customers. Surface modification (through the use of laser processing) and surface coatings are both being used to prevent the formation of biofilms on surfaces.^{209,210} Despite these positive factors of using AgNCs, there are still negatives to using AgNCs for human applications. Silver ions, of which nanocrystals within the body would become a source, are toxic to mammalian species in high levels. It has been well documented, and evidence shows toxicity to multiple organs. However, additional evidence is required for a clearer understanding of the mechanisms involved.^{211,212} By using AgNC films for antibacterial applications it is hoped to be a balance between sufficient silver to prevent biofilm formation whilst keeping the overall dose, and therefore toxicity, low.

AgNC films generated in the method previously described, were coated onto glass microscope slides. The prepared AgNC films were used by collaborators in Chester to investigate the ability of AgNCs to counter biofilm formation by the Gram-negative bacteria, *Escherichia coli* (ATCC 25922). Prior to testing the AgNC films were autoclaved at 121 °C for 15 min,

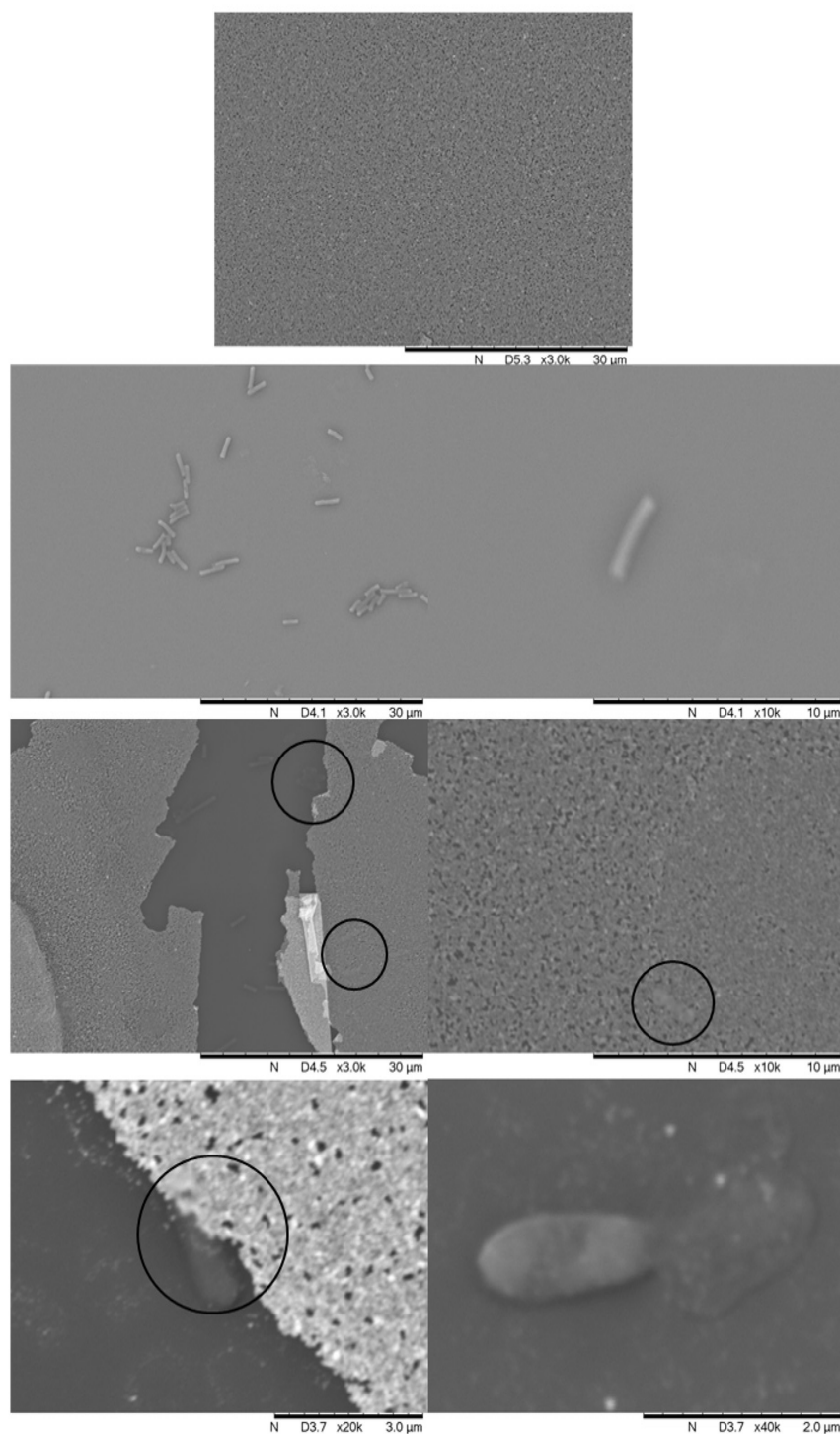


Figure 6.1 – Scanning electron microscopy of the AgNC films. (A) Control sample of Ag unexposed to bacteria. (B and C) *E. coli* adhered to a reference glass microscope slide, incubated for 24 hours. (D-G) *E. coli* adhered to AgNC films after 24 h of incubation, Denatured *E. coli* cells have been circled.

then placed in antiseptic petri dishes. pregrown cultures were added and incubated at 37 °C for 6, 12 and 24 hour periods. After each time point, the samples were then removed and rinsed twice with sterile phosphate-buffered saline to remove any planktonic bacteria before analysis.

6.2 Results and Discussion

SEM micrographs of *E. coli* adhered to surfaces with and without the AgNC coating are displayed in figure 6.1. Figure 6.1A shows a control silver film with no bacteria present. Showing, as you would expect, no growth of bacterial colonies. Demonstrating an absence of contamination in processing of the samples. Figure 6.1B and C display a control sample of the bare glass slide in the bacteria broth. The *E. coli* cells, unexposed to silver, are smooth and show the typical characteristics of rod cell shape and size ($\approx 3 \text{ }\mu\text{m}$). The adhered cells exposed to the AgNC films, however, were damaged severely. The damage can be seen in Figure 6.1D–G, with misshapen, pitted, fragmented and translucent cells, suggesting leakage of the cell content. This is in agreement with previous studies looking into the effects of AgNCs on *E. coli*.^{211,212} The effects of AgNC films on the growth of *E. coli* over 24 h was investigated by epifluorescence microscopy. Samples were stained using Syto-9 and propidium iodide (PI). Syto-9 is a small green fluorescing molecule that can penetrate the cell walls with ease, therefore staining all cells regardless of their viability. Conversely, the red fluorescing PI molecule cannot penetrate the cell membrane, so only compromised cells will become stained²¹³ (figure 6.2). As can be seen in figure 6.2, the bacteria on glass substrates remain intact (green) whilst bacteria exposed to the AgNC films become predominantly denatured with compromised cell walls (red). Demonstrating the strong antibacterial activity of the silver nanocrystal films across the time period. The observations from SEM confirm that the cells are being denatured and there is cell membrane compromising when in contact with AgNCs.

6.3 Conclusion

The antibacterial effect of AgNC films on Gram-negative *E. coli* bacteria has been investigated as a method of halting biofilm formation. The simple, low temperature, one-pot, low-cost, liquid based method of preparing AgNC films has been used to generate thin repeatable and uniform films of nanocrystals on glass microscope slide substrates. The prepared AgNC films have been shown to be an effective deterrent in the biofilm formation of *E. coli* when

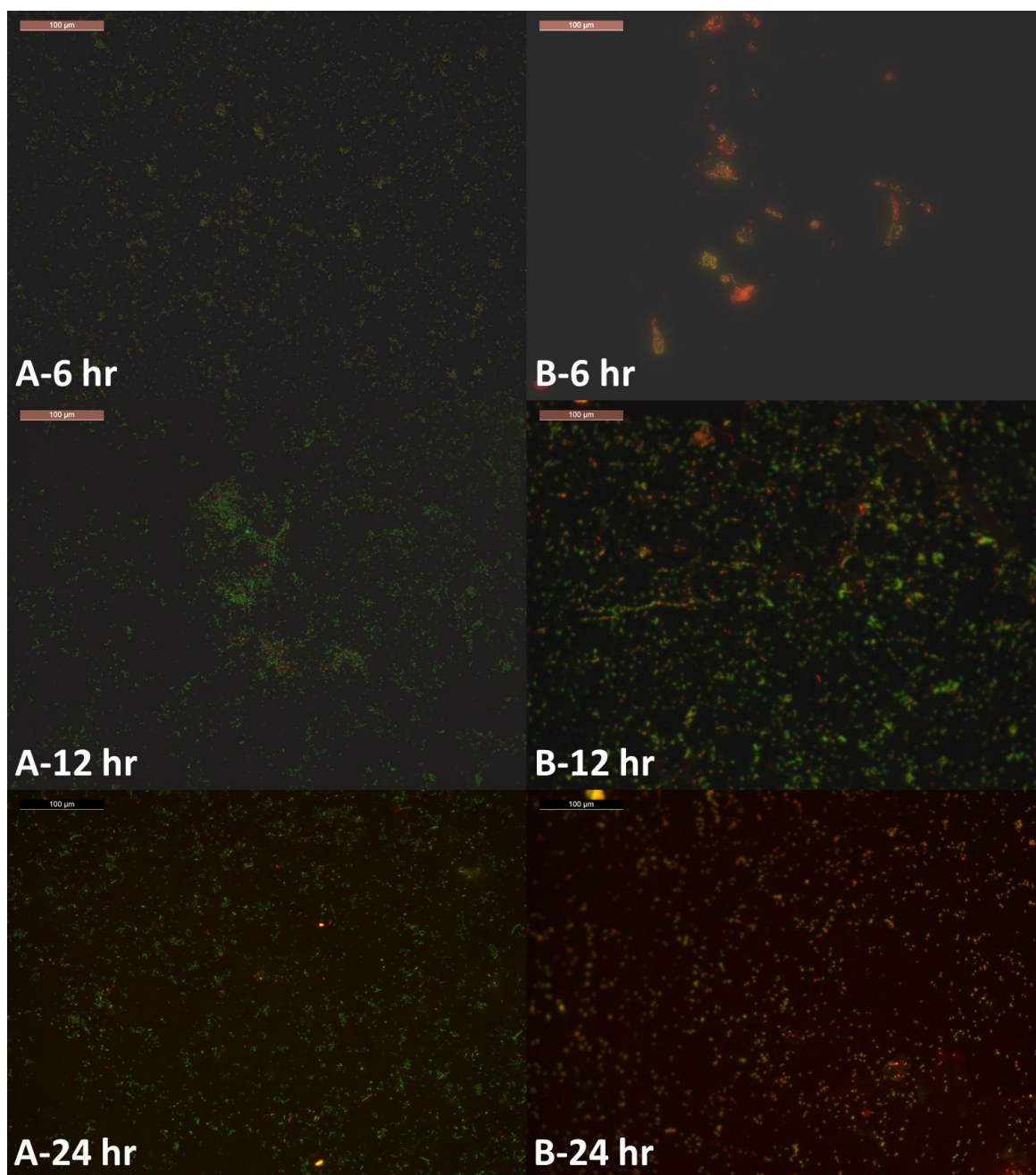


Figure 6.2 – Fluorescence micrographs of (A) *E. coli* adhered to a reference glass microscope slide and (B) an AgNC film after 6, 12 and 24 h incubation. The scale bar shown in the top left of each image is 100 μm . The green fluorescent staining indicates live cells and the red dead cells. Some of the images (such as B-12 h) appear green, but on closer inspection the interior of the bacteria cell is red, indicating death, and the green is the outer cell membrane casing.

compared to blank microscope slide controls. The SEM images indicate there is a high degree of cell membrane disruption causing a loss of cell integrity. It should however be mentioned that the film to substrate adhesion is very limited and over extended exposure or application of friction the films are known to break down and come away from the substrate. These antibacterial AgNC films would be an interesting and cost effective coating for use in medical and food applications, if the surface coatings could be stabilised and a greater bond be perfected.

Chapter 7

Summary and Future Work

In Summary, I have been able to practice the techniques required for preparing and characterising metal and metal alloy nanocrystal films prepared at the water–toluene interface. The films have been deposited onto glass, polystyrene and Whatman™ PTFE membrane circle substrates. Which have been used for characterisation, charge transport studies, catalysis testing and Ag antibacterial studies

Charge transport measurements of nanocrystals, on glass substrates, showed that Ag films must form in such a way that their particles are close enough to conduct as the bulk material. When performing organic ligand exchanges on silver films they showed no change in the reported temperature resistance plots, supporting the theory.

Au nanocrystal films, on glass showed a non–metallic charge transport behaviour, akin to a semi–conductor, with two defined conducting mechanisms. When performing inorganic ligand exchanges with Au films it was possible to alter the charge transport properties. Although further investigation is needed to identify if patterns can be predicted through the size and nature of incoming ligands.

Alloys of metallic nanocrystals were prepared in the same manner. $\text{Ag}_x\text{Au}_{1-x}$ alloys show the ability to produce a tunable range of charge transport properties, over $2.4\text{M}\Omega\text{s}$. Similar to the Au nanocrystals the alloys showed two different charge transport mechanisms working across the testing temperature range.

When annealing alloyed $\text{Ag}_x\text{Au}_{1-x}$ films at temperatures below 180°C observations showed and increase in film resistance, believed to be caused by the thermal decomposition of surface ligands reducing conducting pathways. However, at more elevated temperatures surprisingly the resistance dropped, possibly through some thermal rearrangement of nanoparticulates

on the substrate surface. The phenomenon does require retesting and further more in-depth investigation.

Silver, $\text{Ag}_{0.5}\text{Au}_{0.5}$, $\text{Au}_{0.5}\text{Pd}_{0.5}$ and $\text{Ag}_{0.5}\text{Pd}_{0.5}$ nanocrystals have shown catalytic activity in tests as hydrogenation and reduction catalysts. In aqueous medium the supported nanocatalysts were able to catalyse the reduction reactions of 4-nitrophenol and nitrobenzene in the presence of sodium borohydride. In hydrogen rich environments, only the supported nanocatalysts containing Pd were able to catalyse the hydrogenation of cyclohexene to cyclohexane. The percentage of Pd required for hydrogenation to occur is yet to be investigated, as the investigation was to discover if nanocrystal films produced in the method described here could work as catalysts.

Prepared Ag nanocrystal films have been shown to be an effective deterrent in the biofilm formation of *E. coli* when compared to blank microscope slide controls. During investigations it was noted that the adhesion of films to the glass substrate was not great and samples could be easily damaged and flake off the surface. Further work is required in developing and investigating surface modification or alternative supporting substrates to better hold the Ag films and prevent Ag nanocrystals leaching into the environment.

Bibliography

- [1] C. N. R. Rao, P. J. Thomas and G. U. Kulkarni, *Nanocrystals: Synthesis, Properties and Applications*, Springer Berlin Heidelberg, Berlin, Heidelberg, 2007, vol. 95, pp. 1–186.
- [2] S. G. Booth and R. A. W. Dryfe, *J. Phys. Chem. C*, 2015, **119**, 23295–23309.
- [3] D. V. Talapin, J.-s. Lee, M. V. Kovalenko and E. V. Shevchenko, *Chem. Rev.*, 2010, **110**, 389–458.
- [4] A. Zabet-Khosousi and A.-A. Dhirani, *Chem. Rev.*, 2008, **108**, 4072–4124.
- [5] M. Nasilowski, B. Mahler, E. Lhuillier, S. Ithurria and B. Dubertret, *Chem. Rev.*, 2016, acs.chemrev.6b00164.
- [6] K. L. Kelly, E. Coronado, L. L. Zhao and G. C. Schatz, *J. Phys. Chem. B*, 2003, **107**, 668–677.
- [7] D. B. Mitzi, M. Yuan, W. Liu, A. J. Kellock, S. J. Chey, V. Deline and A. G. Schrott, *Adv. Mater.*, 2008, **20**, 3657–3662.
- [8] J. Tang, K. W. Kemp, S. Hoogland, K. S. Jeong, H. Liu, L. Levina, M. Furukawa, X. Wang, R. Debnath, D. Cha, K. W. Chou, A. Fischer, A. Amassian, J. B. Asbury and E. H. Sargent, *Nat. Mater.*, 2011, **10**, 765–771.
- [9] J. Wei, N. Schaeffer and M. P. Pileni, *J. Phys. Chem. B*, 2014, **118**, 14070–14075.
- [10] J. Jang, W. Liu, J. S. Son and D. V. Talapin, *Nano Lett.*, 2014, **14**, 653–662.
- [11] Z. Chen, B. Nadal, B. Mahler, H. Aubin and B. Dubertret, *Adv. Funct. Mater.*, 2014, **24**, 295–302.
- [12] G. Schmid and B. Corain, *Eur. J. Inorg. Chem.*, 2003, **2003**, 3081–3098.

- [13] *Nanoscience*, ed. P. J. Thomas and N. Revaprasadu, Royal Society of Chemistry, Cambridge, 5th edn., 2018, vol. 5.
- [14] D. J. Barber and I. C. Freestone, *Archaeometry*, 1990, **32**, 33–45.
- [15] S. Schacht, Q. Huo, I. G. Voigt-Martin, G. D. Stucky and F. Schulz, *Science.*, 1996, **273**, 768–771.
- [16] M. Faraday, *Philos. Trans. R. Soc. London*, 1857, **147**, 145–181.
- [17] C. N. R. Rao, G. U. Kulkarni, P. J. Thomas and P. P. Edwards, *Chem. - A Eur. J.*, 2002, **8**, 28–35.
- [18] P. Buffat and J.-P. Borel, *Phys. Rev. A*, 1976, **13**, 2287–2298.
- [19] T. Castro, R. Reifengerger, E. Choi and R. P. Andres, *Phys. Rev. B*, 1990, **42**, 8548–8556.
- [20] C. Burda, X. Chen, R. Narayanan and M. A. El-Sayed, *Chem. Rev.*, 2005, **105**, 1025–1102.
- [21] P. Atkins and J. DePaula, *Atkins' Physical Chemistry*, Oxford University Press, 9th edn., 2009.
- [22] P. P. Edwards, R. L. Johnston and C. N. R. Rao, in *Met. Clust. Chem.*, Wiley-VCH Verlag GmbH, Weinheim, Germany, 2002, vol. 3, pp. 1454–1481.
- [23] C. N. R. Rao, G. U. Kulkarni, P. J. Thomas and P. P. Edwards, *Chem. Soc. Rev.*, 2000, **29**, 27–35.
- [24] S. Navalón and H. García, *Nanomaterials*, 2016, **6**, 123.
- [25] E. Lam, S. Hrapovic, E. Majid, J. H. Chong and J. H. Luong, *Nanoscale*, 2012, **4**, 997–1002.

- [26] V. Polshettiwar, R. Luque, A. Fihri, H. Zhu, M. Bouhrara and J.-M. Basset, *Chem. Rev.*, 2011, **111**, 3036–3075.
- [27] M. C. M. Daniel and D. Astruc, *Chem. Rev.*, 2004, **104**, 293–346.
- [28] B. Karimi, M. Tavakolian, F. Mansouri and H. Vali, *ACS Sustain. Chem. Eng.*, 2019, **7**, 3811–3823.
- [29] L. M. Rossi, F. P. Silva, L. L. R. Vono, P. K. Kiyohara, E. L. Duarte, R. Itri, R. Landers and G. Machado, *Green Chem.*, 2007, **9**, 379.
- [30] P. K. Jain, X. Huang, I. H. El-Sayed and M. A. El-Sayed, *Plasmonics*, 2007, **2**, 107–118.
- [31] N. S. Abadeer and C. J. Murphy, *J. Phys. Chem. C*, 2016, **120**, 4691–4716.
- [32] S. K. Ghosh and T. Pal, *Chem. Rev.*, 2007, **107**, 4797–4862.
- [33] S. Link and M. A. El-Sayed, *Int. Rev. Phys. Chem.*, 2000, **19**, 409–453.
- [34] A. J. Frank, N. Cathcart, K. E. Maly and V. Kitaev, *J. Chem. Educ.*, 2010, **87**, 1098–1101.
- [35] S. Berchmans, P. J. Thomas and C. N. R. Rao, *J. Phys. Chem. B*, 2002, **106**, 4647–4651.
- [36] B. L. Cushing, V. L. Kolesnichenko and C. J. O'Connor, *Chem. Rev.*, 2004, **104**, 3893–3946.
- [37] G. L. Stansfield and P. J. Thomas, *J. Am. Chem. Soc.*, 2012, **134**, 11888–11891.
- [38] D. Yogeve and S. Efrima, *J. Phys. Chem.*, 1988, **92**, 5754–5760.
- [39] P. J. Thomas, E. Mbufu and P. O'Brien, *Chem. Commun.*, 2013, **49**, 118–127.
- [40] C. N. R. Rao, G. U. Kulkarni, P. J. Thomas, V. V. Agrawal and P. Saravanan, *J. Phys. Chem. B*, 2003, **107**, 7391–7395.
- [41] L. Zheng and J. Li, *J. Phys. Chem. B*, 2005, **109**, 1108–1112.

- [42] P. J. Thomas, G. U. Kulkarni and C. N. R. Rao, *J. Phys. Chem. B*, 2000, **104**, 8138–8144.
- [43] C. N. R. Rao, G. U. Kulkarni, P. J. Thomas, V. V. Agrawal, U. K. Gautam and M. Ghosh, *Curr. Sci.*, 2003, **85**, 1041–1045.
- [44] U. K. Gautam, M. Ghosh and C. N. R. Rao, *Langmuir*, 2004, **20**, 10775–10778.
- [45] E. Albrasi, A. J. Kelly, S. Johal, P. O’Brien, S. N. Baxter and P. Thomas, *J. Colloid Interface Sci.*, 2017, **496**, 474–478.
- [46] G. L. Stansfield, H. M. Johnston, S. N. Baxter and P. Thomas, *RSC Adv.*, 2018, **8**, 6225–6230.
- [47] I. Benjamin, *Chem. Rev.*, 2006, **106**, 1212–1233.
- [48] Z. Samec, *Chem. Rev.*, 1988, **88**, 617–632.
- [49] I. Benjamin, *J. Phys. Chem. B*, 2008, **112**, 15801–15806.
- [50] D. Wang, H. Duan and H. Möhwald, *Soft Matter*, 2005, **1**, 412.
- [51] H. Duan, D. Wang, D. G. Kurth and H. Möhwald, *Angew. Chemie Int. Ed.*, 2004, **43**, 5639–5642.
- [52] V. V. Agrawal, P. Mahalakshmi, G. U. Kulkarni and C. N. R. Rao, *Langmuir*, 2006, **22**, 1846–1851.
- [53] J. L. Hueso, V. Sebastián, Á. Mayoral, L. Usón, M. Arruebo and J. Santamaría, *RSC Adv.*, 2013, **3**, 10427.
- [54] A. Hoffman, *J. Am. Chem. Soc.*, 1921, **43**, 1684–1688.
- [55] A. Hoffman, *J. Am. Chem. Soc.*, 1930, **52**, 2995–2998.
- [56] W. J. Vullo, *J. Org. Chem.*, 1968, **V**, 9–11.

- [57] W. A. Reeves and J. D. Guthrie, *Ind. Eng. Chem.*, 1956, **48**, 64–67.
- [58] D. G. Duff, A. Baiker and P. P. Edwards, *Langmuir*, 1993, **9**, 2301–2309.
- [59] D. G. Duff, A. Baiker and P. P. Edwards, *J. Chem. Soc. Chem. Commun.*, 1993, **272**, 96.
- [60] W. W. Bryan, A. C. Jamison, P. Chinwangso, S. Rittikulsittichai, T.-C. Lee and T. R. Lee, *RSC Adv.*, 2016, **6**, 68150–68159.
- [61] P. J. Thomas, G. U. Kulkarni and C. N. R. Rao, *J. Mater. Chem.*, 2004, **14**, 625–628.
- [62] M. K. Sanyal, V. V. Agrawal, M. K. Bera, K. P. Kalyanikutty, J. Daillant, C. Blot, S. Kubowicz, O. Konovalov and C. N. R. Rao, *J. Phys. Chem. C*, 2008, **112**, 1739–1743.
- [63] D. Li, Z. Chen, Z. Wan, T. Yang, H. Wang and X. Mei, *RSC Adv.*, 2016, **6**, 34090–34095.
- [64] G. Hofmann, G. Tofighi, G. Rinke, S. Baier, A. Ewinger, A. Urban, A. Wenka, S. Heideker, A. Jahn, R. Dittmeyer and J.-D. Grunwaldt, *J. Phys. Conf. Ser.*, 2016, **712**, 012072.
- [65] L. Usón, V. Sebastian, A. Mayoral, J. L. Hueso, A. Eguizabal, M. Arruebo and J. Santamaria, *Nanoscale*, 2015, **7**, 10152–10161.
- [66] G. L. Stansfield, P. V. Vanitha, H. M. Johnston, D. Fan, H. AlQahtani, L. Hague, M. Grell and P. J. Thomas, *Philos. Trans. A. Math. Phys. Eng. Sci.*, 2010, **368**, 4313–30.
- [67] D. G. Duff, A. Baiker, I. Gameson and P. P. Edwards, *Langmuir*, 1993, **9**, 2310–2317.
- [68] V. V. Agrawal, G. U. Kulkarni and C. N. R. Rao, *J. Phys. Chem. B*, 2005, **109**, 7300–7305.
- [69] C. N. R. Rao and K. P. Kalyanikutty, *Acc. Chem. Res.*, 2008, **41**, 489–499.

- [70] R. Krishnaswamy, S. Majumdar, R. Ganapathy, V. V. Agrawal, A. K. Sood and C. N. R. Rao, *Langmuir*, 2007, **23**, 3084–3087.
- [71] P. J. Thomas, G. U. Kulkarni and C. Rao, *Chem. Phys. Lett.*, 2000, **321**, 163–168.
- [72] W. Wang, T. Lee and M. A. Reed, in *Introd. Mol. Electron.*, Springer Berlin Heidelberg, 2005, vol. 680, pp. 275–300.
- [73] C. P. Collier, T. Vossmeier and J. R. Heath, *Annu. Rev. Phys. Chem.*, 1998, **49**, 371–404.
- [74] C. A. Neugebauer and M. B. Webb, *J. Appl. Phys.*, 1962, **33**, 74.
- [75] N. J. Hardy, M. D. Hanwell and T. H. Richardson, *J. Mater. Sci. Mater. Electron.*, 2007, **18**, 943–949.
- [76] S. Kano, T. Tada and Y. Majima, *Chem. Soc. Rev.*, 2015, **44**, 970–987.
- [77] H. Zhang, Y. Yasutake, Y. Shichibu, T. Teranishi and Y. Majima, *Phys. Rev. B*, 2005, **72**, 205441.
- [78] S. Karmakar, S. Kumar, P. Marzo, E. Primiceri, R. Di Corato, R. Rinaldi, P. G. Cozzi, A. P. Bramanti and G. Maruccio, *Nanoscale*, 2012, **4**, 2311.
- [79] P. Zhang and T. K. Sham, *Appl. Phys. Lett.*, 2002, **81**, 736.
- [80] S. Pradhan, J. Sun, F. Deng and S. Chen, *Adv. Mater.*, 2006, **18**, 3279–3283.
- [81] J. Kane, J. Ong and R. F. Saraf, *J. Mater. Chem.*, 2011, **21**, 16846.
- [82] C. Duan, Y. Wang, J. Sun, C. Guan, S. Grunder, M. Mayor, L. Peng and J. Liao, *Nanoscale*, 2013, **5**, 10258–10266.
- [83] P. Yang, I. Arfaoui, T. Cren, N. Goubet and M. P. Pileni, *J. Phys. Condens. Matter*, 2013, **25**, 335302.
- [84] R. Parthasarathy, X.-M. Lin and H. M. Jaeger, *Phys. Rev. Lett.*, 2001, **87**, 4.

- [85] D. Yu, C. Wang, B. L. Wehrenberg and P. Guyot-Sionnest, *Phys. Rev. Lett.*, 2004, **92**, 216802–1.
- [86] S. Kano, Y. Azuma, M. Kanehara, T. Teranishi and Y. Majima, *Appl. Phys. Express*, 2010, **3**, 105003.
- [87] H. Koo, S. Kano, D. Tanaka, M. Sakamoto, T. Teranishi, G. Cho and Y. Majima, *Appl. Phys. Lett.*, 2012, **101**, 083115.
- [88] B. Skinner, T. Chen and B. I. Shklovskii, *Phys. Rev. B*, 2012, **85**, 1–13.
- [89] H. Grabert and M. H. Devoret, *Single Charge Tunneling*, Springer US, Boston, MA, 1992, vol. 294.
- [90] T. Chen, B. Skinner, W. Xie, B. I. Shklovskii and U. R. Kortshagen, *J. Phys. Chem. C*, 2014, **118**, 19580–19588.
- [91] J. Liao, S. Blok, S. J. van der Molen, S. Diefenbach, A. W. Holleitner, C. Schönenberger, A. Vladyka and M. Calame, *Chem. Soc. Rev.*, 2015, **44**, 999–1014.
- [92] N. Mott, *Philos. Mag.*, 1972, **11**, 1–18.
- [93] A. L. Efros and B. I. Shklovskii, *J. Phys. C Solid State Phys.*, 1975, **8**, L49–L51.
- [94] P. J. Thomas, G. L. Stansfield, N. Komba, D. J. H. Cant, K. Ramasamy, E. Albrasi, H. Al-Chaghouri, K. L. Syres, P. O’Brien, W. R. Flavell, E. Mubofu, F. Bondino and E. Magnano, *RSC Adv.*, 2015, **5**, 62291–62299.
- [95] K. Whitham, J. Yang, B. H. Savitzky, L. F. Kourkoutis, F. Wise and T. Hanrath, *Nat. Mater.*, 2016, **15**, 557–563.
- [96] S. K. Ram, S. Kumar, R. Vanderhaghen and P. Roca i Cabarrocas, *J. Non. Cryst. Solids*, 2002, **299-302**, 411–415.
- [97] P. Guyot-Sionnest, *J. Phys. Chem. Lett.*, 2012, **3**, 1169–1175.

- [98] N. Mott, *J. Non. Cryst. Solids*, 1968, **1**, 1–17.
- [99] D. Joung and S. I. Khondaker, *Phys. Rev. B*, 2012, **86**, 235423.
- [100] H. Liu, A. Pourret and P. Guyot-Sionnest, *ACS Nano*, 2010, **4**, 5211–5216.
- [101] M. A. Boles, D. Ling, T. Hyeon and D. V. Talapin, *Nat. Mater.*, 2016, **15**, 141–153.
- [102] C. R. Kagan, E. Lifshitz, E. H. Sargent and D. V. Talapin, *Science.*, 2016, **353**, aac5523–aac5523.
- [103] R. Wang, Y. Shang, P. Kanjanaboos, W. Zhou, Z. Ning and E. H. Sargent, *Energy Environ. Sci.*, 2016, **9**, 1130–1143.
- [104] L. Protesescu, M. Nachttegaal, O. Voznyy, O. Borovinskaya, A. J. Rossini, L. Emsley, C. Copéret, D. Günther, E. H. Sargent and M. V. Kovalenko, *J. Am. Chem. Soc.*, 2015, **137**, 1862–1874.
- [105] N. C. Anderson, M. P. Hendricks, J. J. Choi and J. S. Owen, *J. Am. Chem. Soc.*, 2013, **135**, 18536–18548.
- [106] M. V. Kovalenko, L. Manna, A. Cabot, Z. Hens, D. V. Talapin, C. R. Kagan, V. I. Klimov, A. L. Rogach, P. Reiss, D. J. Milliron, P. Guyot-Sionnest, G. Konstantatos, W. J. Parak, T. Hyeon, B. A. Korgel, C. B. Murray and W. Heiss, *ACS Nano*, 2015, **9**, 1012–1057.
- [107] C. R. Kagan and C. B. Murray, *Nat. Nanotechnol.*, 2015, **10**, 1013–1026.
- [108] P. Reiss, M. Carrière, C. Lincheneau, L. Vaure and S. Tamang, *Chem. Rev.*, 2016, acs.chemrev.6b00116.
- [109] A. Nag, H. Zhang, E. Janke and D. V. Talapin, *Zeitschrift für Phys. Chemie*, 2015, **229**, 85–107.
- [110] J.-H. Choi, H. Wang, S. J. Oh, T. Paik, P. Sung, J. Sung, X. Ye, T. Zhao, B. T. Diroll, C. B. Murray and C. R. Kagan, *Science.*, 2016, **352**, 205–208.

- [111] J. M. Luther, M. Law, Q. Song, C. L. Perkins, M. C. Beard and A. J. Nozik, *ACS Nano*, 2008, **2**, 271–280.
- [112] L. Wang, P.-A. Albouy and M. P. Pileni, *Chem. Mater.*, 2015, **27**, 4431–4440.
- [113] F. Schulz, G. T. Dahl, S. Besztejan, M. A. Schroer, F. Lehmkuhler, G. Grübel, T. Voss-meyer and H. Lange, *Langmuir*, 2016, [acs.langmuir.6b01704](https://doi.org/10.1021/acs.langmuir.6b01704).
- [114] R. Debnath, J. Tang, D. A. Barkhouse, X. Wang, A. G. Pattantyus-Abraham, L. Brzo-zowski, L. Levina and E. H. Sargent, *J. Am. Chem. Soc.*, 2010, **132**, 5952–5953.
- [115] H. Nakanishi, K. J. M. Bishop, B. Kowalczyk, A. Nitzan, E. A. Weiss, K. V. Tretiakov, M. M. Apodaca, R. Klajn, J. F. Stoddart and B. A. Grzybowski, *Nature*, 2009, **460**, 371–375.
- [116] S. C. Warren, D. A. Walker and B. A. Grzybowski, *Langmuir*, 2012, **28**, 9093–9102.
- [117] G. Li, H. Abroshan, C. Liu, S. Zhuo, Z. Li, Y. Xie, H. J. Kim, N. L. Rosi and R. Jin, *ACS Nano*, 2016, **10**, 7998–8005.
- [118] A. Nag, M. V. Kovalenko, J.-s. Lee, W. Liu, B. Spokoyny and D. V. Talapin, *J. Am. Chem. Soc.*, 2011, **133**, 10612–10620.
- [119] D. S. Dolzhenkov, H. Zhang, J. Jang, J. S. Son, M. G. Panthani, T. Shibata, S. Chattopadhyay and D. V. Talapin, *Science*, 2015, **347**, 425–428.
- [120] M. V. Kovalenko, M. I. Bodnarchuk, J. Zaumseil, J.-S. Lee and D. V. Talapin, *J. Am. Chem. Soc.*, 2010, **132**, 10085–10092.
- [121] M. V. Kovalenko, M. Scheele and D. V. Talapin, *Science*, 2009, **324**, 1417–1420.
- [122] R. W. Crisp, J. N. Schrauben, M. C. Beard, J. M. Luther and J. C. Johnson, *Nano Lett.*, 2013, **13**, 4862–4869.
- [123] D. N. Dirin, S. Dreyfuss, M. I. Bodnarchuk, G. Nedelcu, P. Papagiorgis, G. Itskos and M. V. Kovalenko, *J. Am. Chem. Soc.*, 2014, **136**, 6550–6553.

- [124] H. Zhang, J. Jang, W. Liu and D. V. Talapin, *ACS Nano*, 2014, **8**, 7359–7369.
- [125] H. Zhang, B. Hu, L. Sun, R. Hovden, F. W. Wise, D. A. Muller and R. D. Robinson, *Nano Lett.*, 2011, **11**, 5356–5361.
- [126] H. Zhang, J. Yang, J.-R. Chen, J. R. Engstrom, T. Hanrath and F. W. Wise, *J. Phys. Chem. Lett.*, 2016, **7**, 642–646.
- [127] P. R. Brown, D. Kim, R. R. Lunt, N. Zhao, M. G. Bawendi, J. C. Grossman and V. Bulović, *ACS Nano*, 2014, **8**, 5863–5872.
- [128] S. J. Oh, Z. Wang, N. E. Berry, J.-H. Choi, T. Zhao, E. A. Gaulding, T. Paik, Y. Lai, C. B. Murray and C. R. Kagan, *Nano Lett.*, 2014, **14**, 6210–6216.
- [129] W.-K. Koh, S. R. Saudari, A. T. Fafarman, C. R. Kagan and C. B. Murray, *Nano Lett.*, 2011, **11**, 4764–4767.
- [130] A. T. Fafarman, W.-k. Koh, B. T. Diroll, D. K. Kim, D.-K. Ko, S. J. Oh, X. Ye, V. Doan-Nguyen, M. R. Crump, D. C. Reifsnyder, C. B. Murray and C. R. Kagan, *J. Am. Chem. Soc.*, 2011, **133**, 15753–15761.
- [131] S. J. Oh, N. E. Berry, J.-H. Choi, E. A. Gaulding, T. Paik, S.-H. Hong, C. B. Murray and C. R. Kagan, *ACS Nano*, 2013, **7**, 2413–2421.
- [132] D. B. Mitzi, *Adv. Mater.*, 2009, **21**, 3141–3158.
- [133] D. K. Kim, Y. Lai, B. T. Diroll, C. B. Murray and C. R. Kagan, *Nat. Commun.*, 2012, **3**, 1216.
- [134] J.-H. Choi, A. T. Fafarman, S. J. Oh, D.-K. Ko, D. K. Kim, B. T. Diroll, S. Muramoto, J. G. Gillen, C. B. Murray and C. R. Kagan, *Nano Lett.*, 2012, **12**, 2631–2638.
- [135] S. J. Oh, N. E. Berry, J.-H. Choi, E. A. Gaulding, H. Lin, T. Paik, B. T. Diroll, S. Muramoto, C. B. Murray and C. R. Kagan, *Nano Lett.*, 2014, **14**, 1559–1566.

- [136] D. V. Sanghani, P. J. Smith, D. W. Allen and B. F. Taylor, *Inorganica Chim. Acta*, 1982, **59**, 203–206.
- [137] M. Diab, B. Moshofsky, I. Jen-La Plante and T. Mokari, *J. Mater. Chem.*, 2011, **21**, 11626.
- [138] W. Schiwy, S. Pohl and B. Krebs, *Zeitschrift fr Anorg. und Allg. Chemie*, 1973, **402**, 77–86.
- [139] E. E. Jelley, *J. Chem. Soc.*, 1933, 1580.
- [140] M. Brust, M. Walker, D. Bethell, D. J. Schiffrin and R. Whyman, *J. Chem. Soc., Chem. Commun.*, 1994, 801–802.
- [141] J. B. Pełka, M. Brust, P. Gierłowski, W. Paszkowicz and N. Schell, *Appl. Phys. Lett.*, 2006, **89**, 063110.
- [142] B. A. Korgel, S. Fullam, S. Connolly and D. Fitzmaurice, *J. Phys. Chem. B*, 1998, **102**, 8379–8388.
- [143] D. V. Talapin and C. B. Murray, *Science.*, 2005, **310**, 86–9.
- [144] T. S. Mentzel, V. J. Porter, S. Geyer, K. MacLean, M. G. Bawendi and M. A. Kastner, *Phys. Rev. B*, 2008, **77**, 075316.
- [145] N. Cioffi, L. Colaianne, E. Ieva, R. Pilolli, N. Ditaranto, M. D. Angione, S. Cotrone, K. Buchholt, A. L. Spetz, L. Sabbatini and L. Torsi, *Electrochim. Acta*, 2011, **56**, 3713–3720.
- [146] K. Luo, C. Hu, Y. Luo, D. Li, Y. Xiang, Y. Mu, H. Wang and Z. Luo, *RSC Adv.*, 2017, **7**, 51605–51611.
- [147] D. Li, C. Hu, Y. Luo, G. Zhu, Q. Li, Z. Luo and K. Luo, *Appl. Surf. Sci.*, 2019, **475**, 615–620.
- [148] I.-K. Suh, H. Ohta and Y. Waseda, *J. Mater. Sci.*, 1988, **23**, 757–760.

- [149] L. Salamakha, E. Bauer, S. Mudryi, A. Gonçalves, M. Almeida and H. Noël, *J. Alloys Compd.*, 2009, **479**, 184–188.
- [150] A. R. Denton and N. W. Ashcroft, *Phys. Rev. A*, 1991, **43**, 3161–3164.
- [151] B. A. Cymes, M. P. S. Krekeler, K. N. Nicholson and J. D. Grigsby, *Environ. Earth Sci.*, 2017, **76**, 640.
- [152] K. Jyoti, M. Baunthiyal and A. Singh, *J. Radiat. Res. Appl. Sci.*, 2016, **9**, 217–227.
- [153] P. Asanithi, S. Chaiyakun and P. Limsuwan, *J. Nanomater.*, 2012, **2012**, 1–8.
- [154] M. P. Seah, I. S. Gilmore and G. Beamson, *Surf. Interface Anal.*, 1998, **26**, 642–649.
- [155] V. Bemmer, M. Bowker, J. H. Carter, P. R. Davies, L. E. Edwards, K. D. M. Harris, C. E. Hughes, F. Robinson, D. J. Morgan and M. G. Thomas, *RSC Adv.*, 2020, **10**, 8444–8452.
- [156] P. Gobbo, Z. Mossman, A. Nazemi, A. Niaux, M. C. Biesinger, E. R. Gillies and M. S. Workentin, *J. Mater. Chem. B*, 2014, **2**, 1764–1769.
- [157] M. Fantauzzi, B. Elsener, D. Atzei, A. Rigoldi and A. Rossi, *RSC Adv.*, 2015, **5**, 75953–75963.
- [158] N. L. Craig, A. B. Harker and T. Novakov, *Atmos. Environ.*, 1974, **8**, 15–21.
- [159] M. Fantauzzi, A. Rigoldi, B. Elsener, D. Atzei and A. Rossi, *J. Electron Spectros. Relat. Phenomena*, 2014, **193**, 6–15.
- [160] S. Pradhan, L. E. Brown, J. P. Konopelski and S. Chen, *J. Nanoparticle Res.*, 2009, **11**, 1895–1903.
- [161] Y. Akimov, W. Koh and K. Ostrikov, *Opt. Express*, 2009, **17**, 10195.
- [162] G. Xu, M. Tazawa, P. Jin and S. Nakao, *Appl. Phys. A Mater. Sci. Process.*, 2005, **80**, 1535–1540.

- [163] Y. T. Yen, T. Y. Lu, Y. C. Lee, C. C. Yu, Y. C. Tsai, Y. C. Tseng and H. L. Chen, *ACS Appl. Mater. Interfaces*, 2014, **6**, 4292–4300.
- [164] P. P. Edwards, M. T. J. Lodge, F. Hensel and R. Redmer, *Philos. Trans. A. Math. Phys. Eng. Sci.*, 2010, **368**, 941–65.
- [165] M. A. Boles, M. Engel and D. V. Talapin, *Chem. Rev.*, 2016, **116**, 11220–11289.
- [166] M. Brust, D. J. Schiffrin, D. Bethell and C. J. Kiely, *Adv. Mater.*, 1995, **7**, 795–797.
- [167] F. P. Zamborini, L. E. Smart, M. C. Leopold and R. W. Murray, *Anal. Chim. Acta*, 2003, **496**, 3–16.
- [168] R. C. Doty, H. Yu, C. K. Shih and B. A. Korgel, *J. Phys. Chem. B*, 2001, **105**, 8291–8296.
- [169] M. J. Hostetler, J. E. Wingate, C.-J. Zhong, J. E. Harris, R. W. Vachet, M. R. Clark, J. D. Londono, S. J. Green, J. J. Stokes, G. D. Wignall, G. L. Glish, M. D. Porter, N. D. Evans and R. W. Murray, *Langmuir*, 1998, **14**, 17–30.
- [170] M. Brust, D. Bethell, C. J. Kiely and D. J. Schiffrin, *Langmuir*, 1998, **14**, 5425–5429.
- [171] I. Farbman and S. Efrima, *J. Phys. Chem.*, 1992, **96**, 8469–8473.
- [172] H. Abdallah, *Bull. Chem. React. Eng. Catal.*, 2017, **12**, 136.
- [173] L. M. Rossi, F. P. Silva, L. L. R. Vono, P. K. Kiyohara, E. L. Duarte, R. Itri, R. Landers and G. Machado, *Green Chem.*, 2007, **9**, 379.
- [174] J. Zhang, T. Yao, H. Zhang, X. Zhang and J. Wu, *Nanoscale*, 2016, **8**, 18693–18702.
- [175] M. J. Climent, A. Corma and S. Iborra, *Chem. Rev.*, 2011, **111**, 1072–1133.
- [176] B. Lin, Y. Zhang, Y. Zhu, Y. Zou, Y. Hu, X. Du, H. Xie, K. Wang and Y. Zhou, *Catal. Commun.*, 2020, **144**, 106094.

- [177] G. Garg, S. Foltran, I. Favier, D. Pla, Y. Medina-González and M. Gómez, *Catal. Today*, 2020, **346**, 69–75.
- [178] Y. M. A. Yamada, H. Baek, T. Sato, A. Nakao and Y. Uozumi, *Commun. Chem.*, 2020, **3**, 81.
- [179] S. Gu, S. Wunder, Y. Lu, M. Ballauff, R. Fenger, K. Rademann, B. Jaquet and A. Zacccone, *J. Phys. Chem. C*, 2014, **118**, 18618–18625.
- [180] B. Naik, S. Hazra, V. S. Prasad and N. N. Ghosh, *Catal. Commun.*, 2011, **12**, 1104–1108.
- [181] P. Zhang, C. Shao, Z. Zhang, M. Zhang, J. Mu, Z. Guo and Y. Liu, *Nanoscale*, 2011, **3**, 3357–3363.
- [182] S. Saha, A. Pal, S. Kundu, S. Basu and T. Pal, *Langmuir*, 2010, **26**, 2885–2893.
- [183] E. A. Gelder, S. D. Jackson and C. M. Lok, *Chem. Commun.*, 2005, 522–524.
- [184] R. F. Quadrado, G. Gohlke, R. S. Oliboni, A. Smaniotto and A. R. Fajardo, *J. Ind. Eng. Chem.*, 2019, **79**, 326–337.
- [185] A. Metcalfe and M. W. Rowden, *J. Catal.*, 1971, **22**, 30–34.
- [186] N. John Jebarathinam, M. Eswaramoorthy and V. Krishnasamy, *Stud. Surf. Sci. Catal.*, 1998, **113**, 1039–1043.
- [187] X. Yu, M. Wang and H. Li, *Appl. Catal. A Gen.*, 2000, **202**, 17–22.
- [188] S. de Miguel, J. Vilella, E. Jablonski, O. Scelza, C. Salinas-Martinez de Lecea and A. Linares-Solano, *Appl. Catal. A Gen.*, 2002, **232**, 237–246.
- [189] R. Qu, M. Macino, S. Iqbal, X. Gao, Q. He, G. J. Hutchings and M. Sankar, *Nanomaterials*, 2018, **8**, year.

- [190] J. F. de Souza, G. T. da Silva and A. R. Fajardo, *Carbohydr. Polym.*, 2017, **161**, 187–196.
- [191] B. Leipzig, *Zeitschrift für Elektrotechnik und Elektrochemie*, 1898, **4**, 506–514.
- [192] G. Romanazzi, A. M. Fiore, M. Mali, A. Rizzuti, C. Leonelli, A. Nacci, P. Mastrorilli and M. M. Dell’Anna, *Mol. Catal.*, 2018, **446**, 31–38.
- [193] K. A. Korvinson, H. K. Akula, C. T. Malinchak, D. Sebastian, W. Wei, T. A. Khandaker, M. R. Andrzejewska, B. Zajc and M. K. Lakshman, *Adv. Synth. Catal.*, 2020, **362**, 166–176.
- [194] G. R. Fulmer, A. J. M. Miller, N. H. Sherden, H. E. Gottlieb, A. Nudelman, B. M. Stoltz, J. E. Bercaw and K. I. Goldberg, *Organometallics*, 2010, **29**, 2176–2179.
- [195] H. E. Gottlieb, V. Kotlyar and A. Nudelman, *J. Org. Chem.*, 1997, **62**, 7512–7515.
- [196] H. Liu, G. Chen, H. Jiang, Y. Li and R. Luque, *ChemSusChem*, 2012, **5**, 1892–1896.
- [197] S. Ifuku, Y. Tsukiyama, T. Yukawa, M. Egusa, H. Kaminaka, H. Izawa, M. Morimoto and H. Saimoto, *Carbohydr. Polym.*, 2015, **117**, 813–817.
- [198] J. S. Kim, E. Kuk, K. N. Yu, J.-H. Kim, S. J. Park, H. J. Lee, S. H. Kim, Y. K. Park, Y. H. Park, C.-Y. Hwang, Y.-K. Kim, Y.-S. Lee, D. H. Jeong and M.-H. Cho, *Nanomedicine Nanotechnology, Biol. Med.*, 2007, **3**, 95–101.
- [199] S. Gao, D. Yuan, J. Lü and R. Cao, *J. Colloid Interface Sci.*, 2010, **341**, 320–325.
- [200] H. H. Park, H. H. Park, X. Zhang, Y. J. Choi, H. Kim and R. H. Hill, *J. Ceram. Soc. Japan*, 2010, **118**, 1002–1005.
- [201] H. Wang, Y. Lou and D. O. Northwood, *J. Mater. Process. Technol.*, 2008, **204**, 327–330.
- [202] S.-d. Oh, S. Lee, S.-h. Choi, I.-S. Lee, Y.-m. Lee, J.-h. Chun and H.-j. Park, *Colloids Surfaces A Physicochem. Eng. Asp.*, 2006, **275**, 228–233.

- [203] D. H. Chen and Y. W. Huang, *J. Colloid Interface Sci.*, 2002, **255**, 299–302.
- [204] H. A. Chaghouri, M. A. Malik, P. John Thomas and P. O’Brien, *J. Nanosci. Nanotechnol.*, 2016, **16**, 5420–5425.
- [205] H. Peng, Y. Liu, W. Peng, J. Zhang and R. Ruan, *BioResources*, 2016, **11**, 385–399.
- [206] Y. Li, Q. Qiang, X. Zheng and Z. Wang, *Electrochem. commun.*, 2015, **58**, 41–45.
- [207] A. Celebioglu, Z. Aytac, O. C. Umu, A. Dana, T. Tekinay and T. Uyar, *Carbohydr. Polym.*, 2014, **99**, 808–816.
- [208] A. I. Lukman, B. Gong, C. E. Marjo, U. Roessner and A. T. Harris, *J. Colloid Interface Sci.*, 2011, **353**, 433–444.
- [209] A. Gillett, D. Waugh, J. Lawrence, M. Swainson and R. Dixon, *J. Laser Appl.*, 2016, **28**, 022503.
- [210] Q. Zhao and Y. Liu, *J. Food Eng.*, 2006, **72**, 266–272.
- [211] J. L. Graves, M. Tajkarimi, Q. Cunningham, A. Campbell, H. Nonga, S. H. Harrison and J. E. Barrick, *Front. Genet.*, 2015, **6**, 1–13.
- [212] M. Rai, A. Yadav and A. Gade, *Biotechnol. Adv.*, 2009, **27**, 76–83.
- [213] Y. Jin, T. Zhang, Y. H. Samaranayake, H. H. P. Fang, H. K. Yip and L. P. Samaranayake, *Mycopathologia*, 2005, **159**, 353–360.

Supplementary Material

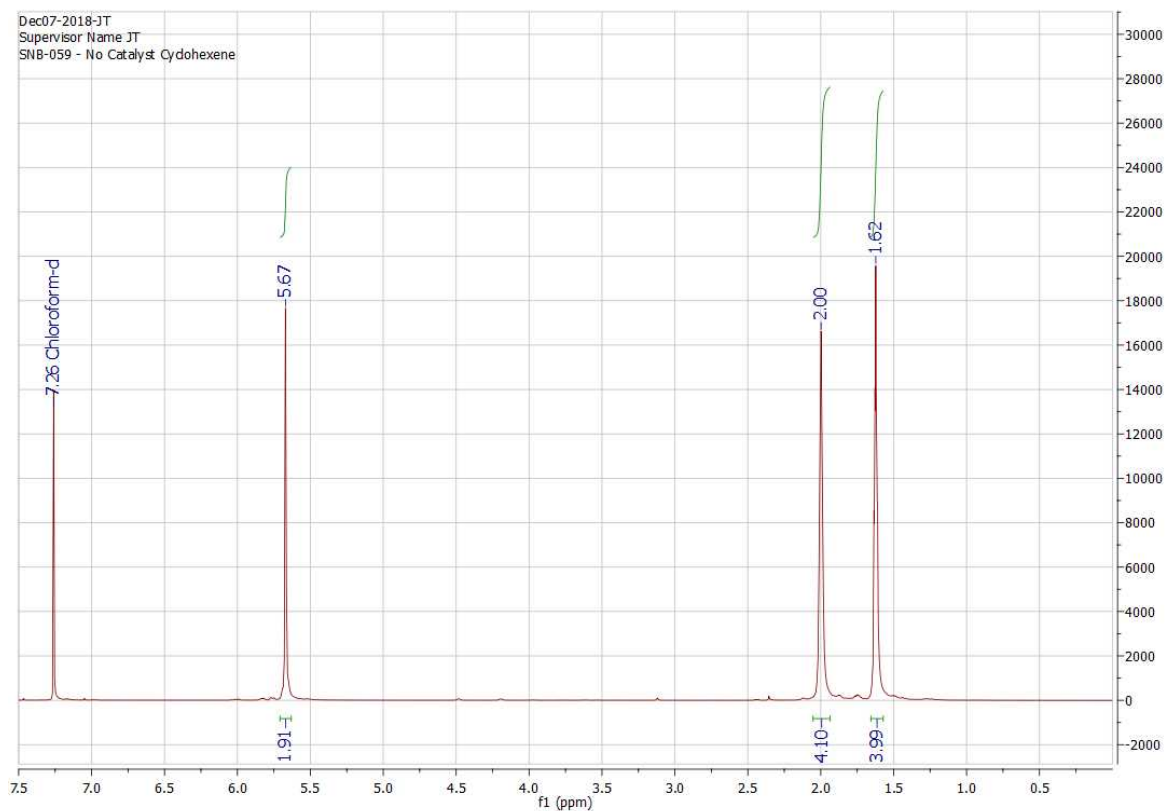


Figure S1 – Proton NMR of crude reaction liqueur in CDCl_3 after heating for 5 hours under H_2 atmosphere in the absence of a catalyst.

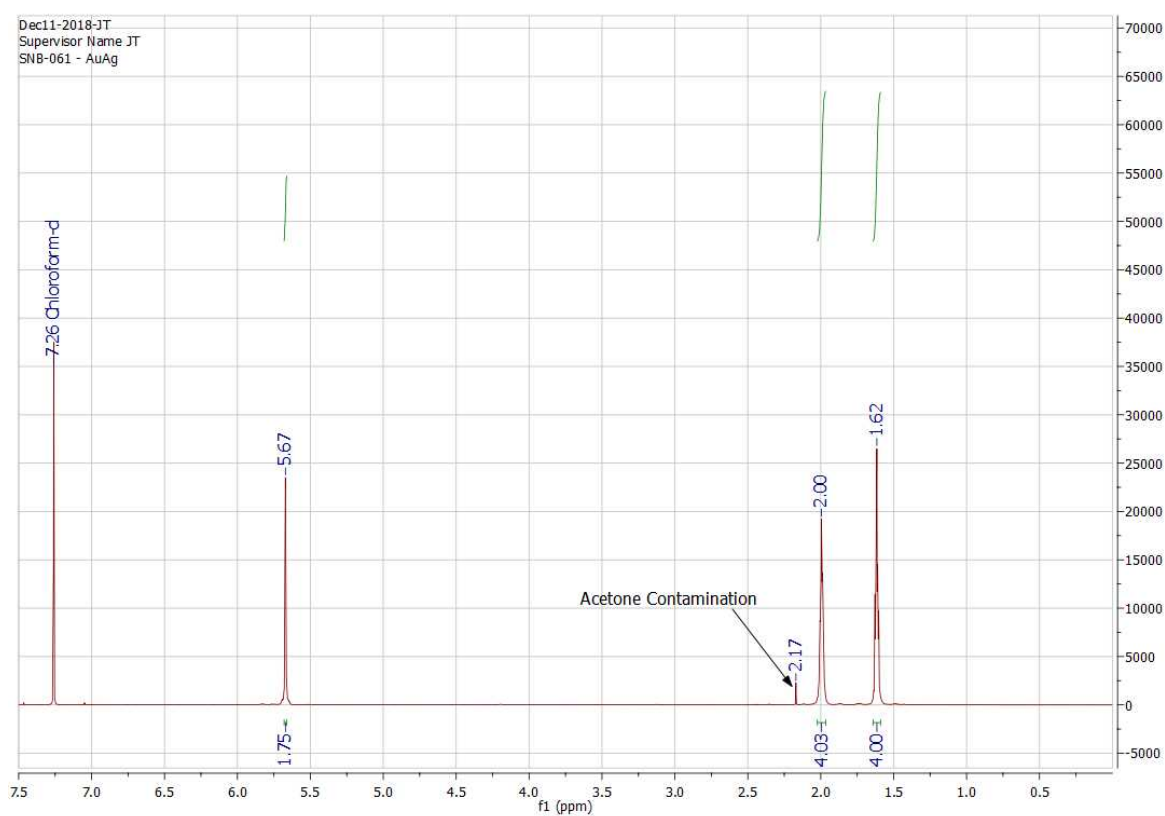


Figure S2 – Proton NMR of crude reaction liqueur in CDCl_3 after heating for 5 hours under H_2 atmosphere in the presence of a $\text{Ag}_{0.5}\text{Au}_{0.5}$ nanocatalyst supported on Whatman™ PTFE membrane circle.

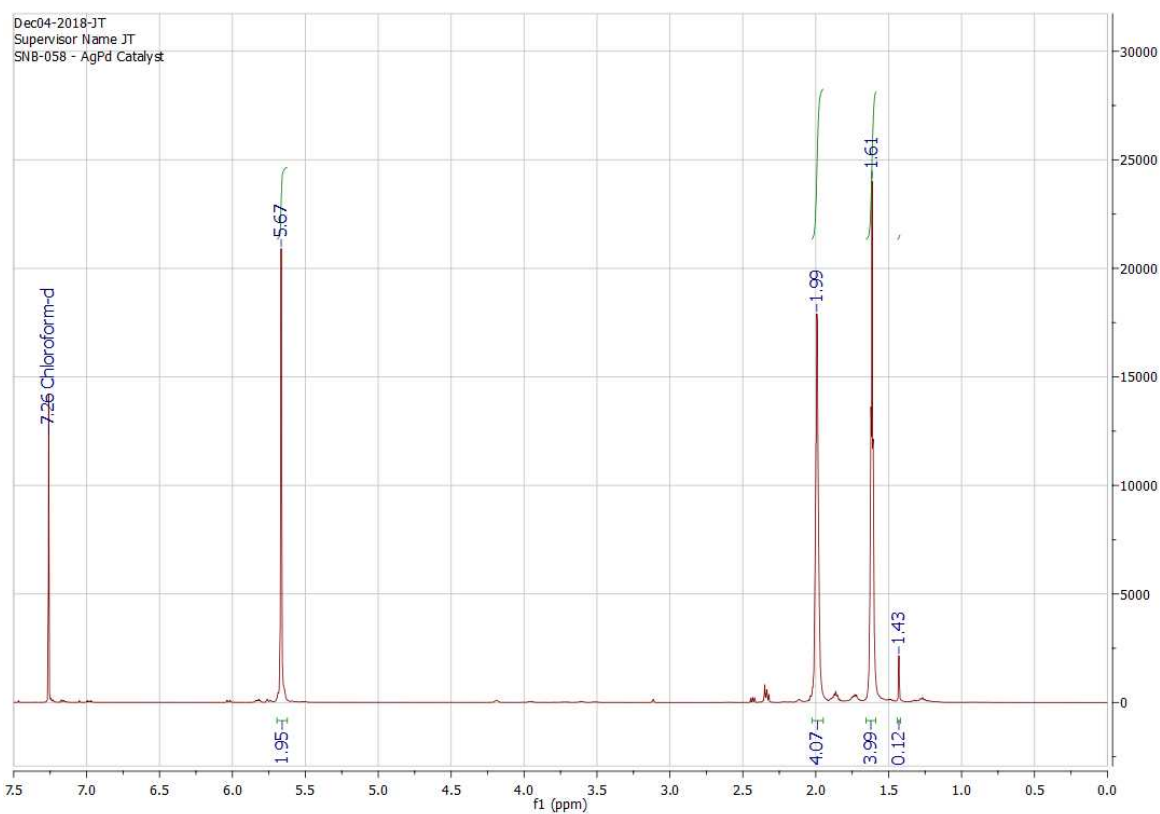


Figure S3 – Proton NMR of crude reaction liqueur in CDCl_3 after heating for 5 hours under H_2 atmosphere in the presence of a $\text{Ag}_{0.5}\text{Pd}_{0.5}$ nanocatalyst supported on Whatman™ PTFE membrane circle. A new peak at 1.43 ppm can be seen, relating to cyclohexane.